



universität
wien

MASTERARBEIT

Titel der Masterarbeit

“Electrical Characterisation and Aging Studies
of Silicon Strip Sensors”

Verfasser

Axel König, BSc

angestrebter akademischer Grad

Master of Science (MSc)

Wien, 2014

Studienkennzahl lt. Studienblatt:

A 066 876

Studienrichtung lt. Studienblatt:

Masterstudium Physik

Betreuer:

Univ. Doz. DI Dr. Manfred Krammer

Contents

1	Experimental Particle Physics at CERN	2
1.1	The Large Hadron Collider	2
1.2	The Compact Muon Solenoid	3
1.2.1	The Silicon Strip Tracker	4
1.2.2	The Phase II Upgrade of the Silicon Strip Tracker	5
2	The Physics of Semiconductors	6
2.1	Energy Band Model	6
2.2	Charge Carrier Density of Intrinsic Semiconductors	7
2.3	Doping of Semiconductors	8
2.4	The p-n Junction or Diode	9
2.4.1	Current-Voltage Characteristics	11
2.4.2	Capacitance-Voltage Characteristics	12
3	Silicon Strip Sensors for Particle Physics Experiments	14
3.1	Working Principle	14
3.2	Sensor Design	16
3.2.1	The Silicon Base or Bulk Material	16
3.2.2	Strip and Backside Implantation	17
3.2.3	Signal Coupling	17
3.2.4	Ring Structures	18
3.2.5	Passivation	18
3.2.6	Pad Structures	19
4	Silicon Strip Sensors Manufactured by Infineon Technologies Austria AG	20
4.1	Wafer Layout	20
5	Sensor Characterisation at HEPHY	23
5.1	Quality Test Setup	23
5.2	Process Quality Control Setup	25
6	Previous Measurement Results	26
6.1	First Batch	26
6.2	Second Batch	27
6.3	Analysis of the Area of defective Strips	28

7	Investigations of the Area of Defective Strips	29
7.1	Field-Effect Transistor Measurements	29
7.1.1	Theoretical Introduction	29
7.1.2	Test Samples and Measurement Setup	32
7.1.3	Measurement Results	35
7.1.4	Conclusion	42
7.2	External Charge Application Using an Ioniser Pistol	43
7.2.1	Measurement Setup and Tests Samples	43
7.2.2	Measurement Results	44
7.3	Formation of the Defective Area at Infineon and HEPHY	47
7.3.1	Sawing Tests	47
7.3.2	Sensor Handling Tests	51
7.3.3	Conclusion	53
7.4	Removal of the Area of Defective Strips	54
7.4.1	Tests Samples and Procedure	54
7.4.2	Measurement Results	55
7.4.3	Conclusion	58
7.5	Examination of the Resistivity of the Passivation Layer	59
7.5.1	Test Samples	60
7.5.2	Measurement Procedure	62
7.5.3	Measurement Setup	66
7.5.4	Measurement Results	68
7.5.5	Conclusion	73
8	Environmental Stress Tests Using a Climate Chamber	74
8.1	Climate Chamber Test Setup	75
8.2	Test Samples	77
8.3	Test Cycle with Varying Relative Humidities	77
8.4	Test Cycle with Varying Temperatures	80
8.5	Conclusion	84
9	Neutron Irradiation Studies	85
9.1	Theoretical Introduction	85
9.1.1	The Non Ionising Energy Loss (NIEL) Scaling Hypothesis	86
9.1.2	Change of the Global Leakage Current Under Irradiation	86
9.1.3	Change of the Full depletion Voltage Under Irradiation	88
9.2	The TRIGA Mark II Reactor at the ATI	89
9.3	Tests Samples Used for Neutron Irradiation Studies	90
9.3.1	Types of Test Samples	90
9.3.2	Preparation of Test Samples	91
9.4	Irradiation Procedure and Electrical Evaluation	93
9.4.1	Irradiation Procedure	93
9.4.2	Electrical Measurements	94

9.5	Measurement Results	95
9.5.1	Current-Voltage Characteristics After Irradiation	95
9.5.2	Capacitance-Voltage Characteristics After Irradiation	97
9.5.3	Results Correlated to the Irradiation Time and Fluence Calibration . . .	99
9.6	Conclusion	101
10	Summary and Outlook	103
	Acknowledgments	105
	Bibliography	106

1 Experimental Particle Physics at CERN

The European Organisation for Nuclear Research (CERN) is one of the largest facilities for fundamental research in the field of particle and nuclear physics. It is located close to Geneva, Switzerland, and has in total 21 participating member states from all over Europe. Beside its theoretical physics department, CERN is especially known for its accelerator complex containing the world's largest collider ring, the Large Hadron Collider.

1.1 The Large Hadron Collider

The Large Hadron Collider (LHC) is the world largest synchrotron storage ring with a circumference of about 27 km allowing protons to collide with a center of mass energy of 14 TeV [1]. It is built to test and verify the Standard Model of Particle Physics (SM) and to search for physics beyond of it. The particles in the two counter rotating beams can be brought into collision at four different points, so called interaction points, whereas to every interaction point an experiment corresponds. Two of the four experiments namely CMS and ATLAS are redundant multi-purpose particle detectors searching for still undiscovered particles and new physics. The other two experiments, LHCb and ALICE, have specific tasks like precise measurements of CP-violation or investigations of quark gluon plasmas.

Beside proton beams also lead nuclei beams with a center of mass energy of 1150 TeV [1] can be brought into collision. About 1,200 super conducting dipole magnets with a magnetic field strength up to 8.33 T ensure that the accelerated particles continue to move on a circular path and over 390 quadrupole magnets keep the particle beams focused [1]. The only 5.6 cm wide beam pipe is evacuated to a pressure of only 0.01 μ Pa to minimize the loss of particles and to reduce the spreading of the beam due to scattering. Well defined and spatial small particle bunches with high particle densities along with a high bunch crossing rate enables a luminosity of up to $10^{34} \text{ cm}^{-2} \text{ s}^{-1}$ [1] if the LHC is operating with protons. The luminosity can be calculated according to equation 1.1 with f as the revolution frequency, n the number of bunches in the ring, $N_{1,2}$ the number of particles in crossing bunches and A as the area of overlapping bunches.

$$L = f \cdot n \cdot N_1 \cdot N_2 \cdot A^{-1} \quad (1.1)$$

A further increase in luminosity will be necessary for a detailed analysis of new particles found at the experiments at LHC. A higher luminosity corresponds to more interactions so the chance for rare events to happen is higher. Therefore, an upgrade of the LHC, the High Luminosity LHC (HL-LHC), is planned. It will probably provide an increase in luminosity by one order of magnitude in comparison to the existing LHC up to 2025.

1.2 The Compact Muon Solenoid

The Compact Muon Solenoid (CMS) is one of the two large multi-purpose particle detectors located at one of the four interaction points of the LHC. Its barrel shape with several cylindrical detector layers and endcaps at both ends provides the best technical feasible geometry for detecting particles of different kinds. The phrase “compact” inside the detectors name suggests that it is comparatively small. Actually it is one of the biggest particle detectors ever built, 14.6 m in width and height and 21.6 m in length [2, 3]. Its weight of about 12,500 t makes CMS the worlds heaviest accelerator detector [4]. One of the detectors major tasks is to proof the existence of the by theorists predicted Higgs-Boson and to search for new physics like supersymmetry.

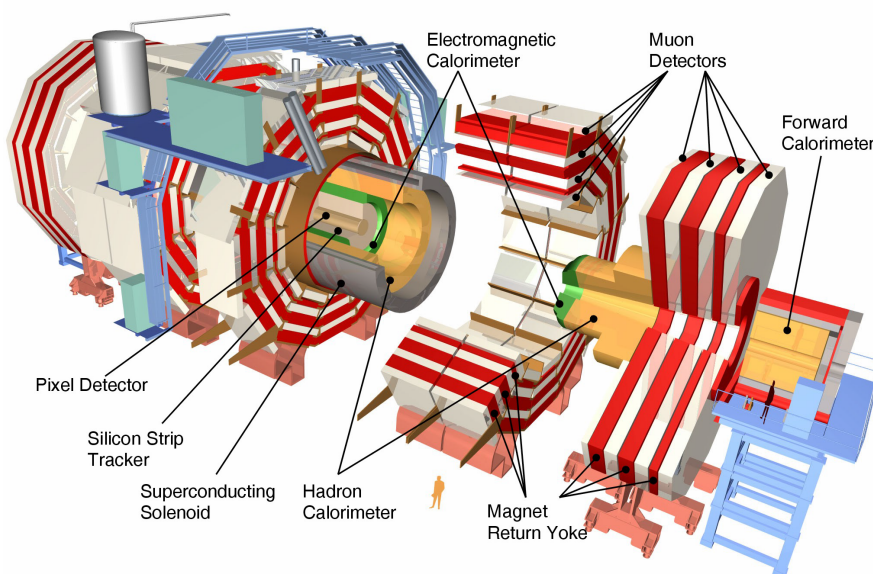


Figure 1.1: Schematic 3D view of the Compact Muon Solenoid [5].

The CMS detector itself is a composition of different detector systems (see figure 1.1) which allow determining the major characteristics like charge, momentum and energy of particles passing through the different detector layers. The principal constituents of CMS are the following:

- **Superconducting Solenoid:** The superconducting solenoid has high importance for particle identification although it is actually not a detector. It provides a magnetic field strength of 4 T [2] used to bend the tracks of charged particles via the Lorentz force. Most of the weight of CMS (i.e. 80 %) arises from the iron return yoke which returns the magnetic flux of the solenoid [2].
- **Inner Tracking System:** This system consists of two silicon based detector types

having different functions. The vertex detector is the innermost detector of CMS and used for the reconstruction of the interaction point. The silicon strip tracker is used to reconstruct the actual tracks of particles arising from the interaction of colliding protons. Along with the curvature of the measured tracks and knowledge of the magnetic field it is then possible to gain the momentum of incident particles.

- **Calorimetry:** CMS consists of two different calorimeter types, the electromagnetic calorimeter (ECAL) and the hadronic calorimeter (HCAL) [3]. Both calorimeters have the task to determine the kinetic energy of a particle by completely stopping them inside the different layers of the calorimeter. The ECAL measures the energy of particles which interact primarily via the electromagnetic force (i.e. electrons, photons etc.) and the HCAL particles which interact primarily via the strong nuclear force (i.e. pions, neutrons etc.).
- **Muon System:** It is important to have a sophisticated muon identification system since muons have a high significance in one of the most probable decay channels of the Higgs-Boson. Muons are not likely to be stopped by the calorimetry system. Therefore, the muon detector is the outermost detector component of CMS. It consists of several gaseous detectors lying in between the iron layers of the return yoke measuring the momentum and charge of the incoming muons.

In July 2012 the CMS and ATLAS experiments observed a new particle with a mass of about $125 \text{ GeV}/c^2$. By now it is assured that the observed particle is the Higgs-Boson which finally completes the Standard Model of Particle Physics. The experimental validation of this fundamental gauge boson is of such a high importance that Peter W. Higgs and François Englert, two of the theoretical physicists that established the so called Brout-Englert-Higgs Mechanism, were honored with the Nobel Prize in Physics in 2013.

1.2.1 The Silicon Strip Tracker

The silicon strip tracker is indispensable for particle identification which makes it one of the most important detectors of CMS. Generally it can be compared to a high resolution digital camera for ionising particles. It is the second innermost detector located right behind the vertex detector and thus exposed to one of the highest radiation doses inside CMS. The therewith related change of the silicon bulk properties makes it necessary to cool the whole tracker to -20°C . The cylindrical shape of the tracker with its 10 overlapping layers (see figure 1.2) along with two endcaps hinders particles from being undetected and enables a micrometer precise track resolution. The tracker consists of 15,148 detector modules having in total 9.8 million readout channels [2]. The modules in turn comprise one or two silicon strip sensors, a support structure and readout chips.

The actual sensitive parts of modules are the silicon strip sensors whereby different variants are installed inside the tracker. Sensors with shorter strips lengths for example are located at the inner layers whereas sensors with larger strips lengths are located at the outermost

layers. Furthermore, different shapes are used, for example trapezoidal one for the endcaps. The granularity of strips and thus the resolution improves from the outer layer to the inner ones. However, a higher granularity inside the outer layers will not necessarily provide a better accuracy but definitively increases the number of read-out channels.

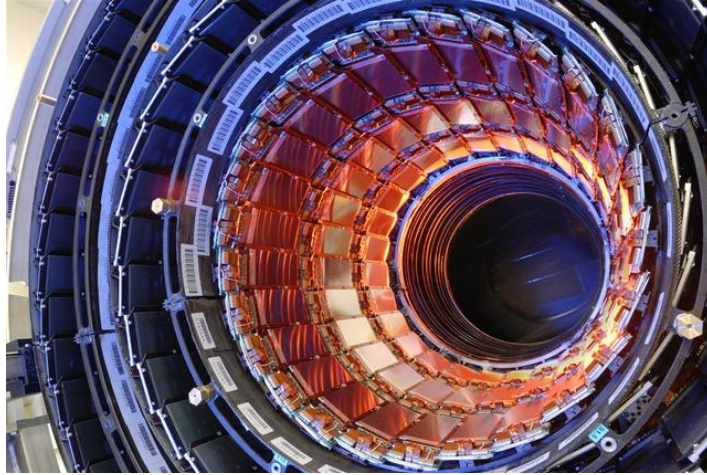


Figure 1.2: The cylindrical layers of the silicon strip tracker [5].

1.2.2 The Phase II Upgrade of the Silicon Strip Tracker

The performance of sensors decreases with the radiation damage caused by incident particles. The degradation in performance will already be significant until the LHC is upgraded around 2025. Hence, a complete exchange of the tracker will be mandatory. This exchange is known as the phase II upgrade and will be conducted right before the HL-LHC gets operative.

The new tracker will have to deal with the significantly higher luminosity of the HL-LHC. Higher luminosity corresponds to more interactions, a higher track density and also a larger radiation damage for the tracker. The new silicon strip tracker will have to deal with those new boundary conditions. In order to resolve the growing track density the tracker will also grow in granularity by means of more implemented silicon strip sensors. Furthermore, the design of the sensors will be different, i.e. shorter strips. The base material of the sensors will also be different which makes the change of the sensor characteristics under irradiation more manageable. One of the biggest changes compared to the old tracker will be the design of the sensor modules. One module will host two stacked silicon strips sensors with a combine readout electronics. Furthermore every sensor module will have a trigger capability. This means that every module provides besides its tracking information also information for physical interesting events. Triggering of events is crucial since it is not possible to store the data of all events detected by CMS.

2 The Physics of Semiconductors

2.1 Energy Band Model

Quantum mechanics shows that the energy of electrons surrounding the nucleus is quantized, so only discrete energy levels can be occupied [6]. The energy levels for a hydrogen atom for example can be calculated according to equation 2.1 with $E_R = 13.6 \text{ eV}$ as the Rydberg-Energy and n as a positive integer [6].

$$E_n = -\frac{E_R}{n^2} \quad (2.1)$$

However, atoms bound in a crystal lattice are forming new energy levels due to atomic interactions. The differences in energy of the newly formed levels are much smaller as compared to those of a single atom. Thus one can say that they are forming a continuous band of energy. The most significant energy bands are called valence band and conduction band. The valence band is in units of energy the highest band which is completely filled with electrons at 0 degree Kelvin. Electrons inside the conduction band are not localised to a specific atom and can propagate over the whole crystal lattice. Whether the conduction band is filled or not depends on the type of the material and the temperature. Furthermore, the Fermi level E_F is of great importance for the band model. It is defined as the energy level where half of the states are populated.

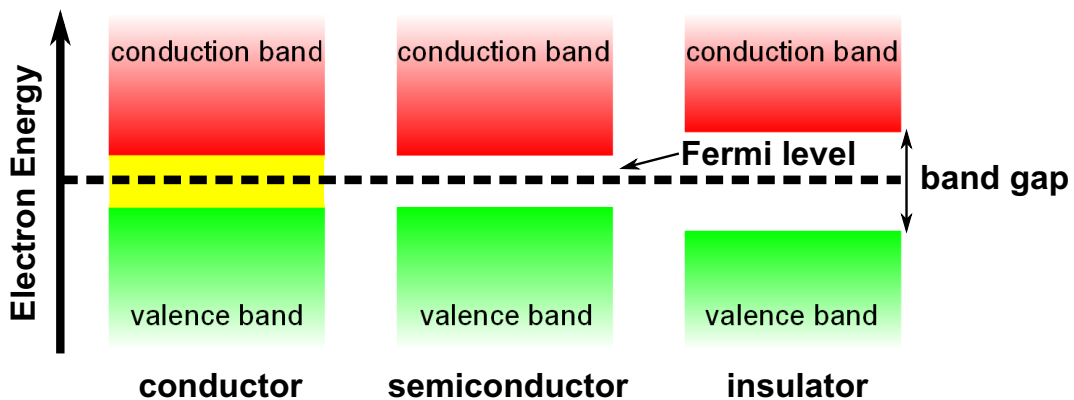


Figure 2.1: Schematic view of the band model for conductors (left), semiconductors (middle) and insulators (right).

Depending on their energy band structure solid-state materials can be divided into three groups namely conductors, insulators and semiconductors (see figure 2.1). For a conductor the valence and the conduction bands are overlapping. Hence, electrons from the valence band contribute to the current flow. Unlike for conductors the valence and conduction bands for insulators are separated through a large band gap. This band gap is a forbidden region of energy which is like the energy bands formed by atomic interactions. This large band gap makes it very unlikely for insulators that electrons can be thermally excited into the conduction band.

The band structure of semiconductors is similar to that of insulators with the exception that the band gap is much smaller. This makes it more likely for electrons to reach the conduction band by thermal excitation. The band gap E_g of silicon for example can be calculated using equation 2.2 by the knowledge of the temperature T [6].

$$E_g(T) = 1.17 - \frac{4.73 \cdot 10^{-4} \times T^2}{T + 636} \quad (2.2)$$

At room temperature (i.e. 300 K) the band gap of silicon is approximately 1.12 eV.

2.2 Charge Carrier Density of Intrinsic Semiconductors

If an electron is excited into the conduction band it leaves a vacancy in the valence band called hole. Equally to electrons also holes contribute to the current flow in a semiconductor. The number of electrons n_e and the number of holes n_p have to be identical for intrinsic¹ semiconductors. Those numbers are again identical to the so called intrinsic carrier density n_i . In general the carrier density can be calculated by integrating the product of the density of allowed energy states per unit volume $N(E)$ and the corresponding occupation probability² $P(E)$ over a defined range of energy [6]:

$$n = \int_{E_1}^{E_2} N(E) \cdot P(E) dE. \quad (2.3)$$

Further calculation yields the intrinsic carrier density n_i in terms of the effective density of states in the conduction and valence band, N_C and N_V [6]:

$$n_i = \sqrt{N_C N_V} \cdot \exp\left(\frac{-E_g}{2kT}\right). \quad (2.4)$$

¹ An intrinsic semiconductor contains by definition only a small amount of impurities compared to the number of thermally generated electrons and holes [6].

² The occupation probability for a specific energy level $P(E) = (1 + \exp(E - E_F)/kT)^{-1}$ can be derived from the Fermi-Dirac-Statistics.

with T as the temperature and k as the Boltzmann constant. The effective state density in the conduction and valance band can be calculated with the use of equation 2.5 [6].

$$N_C = 2 \cdot \left(\frac{2\pi m_e^{\text{eff}} kT}{h^2} \right)^{\frac{3}{2}} \text{ and } N_V = 2 \cdot \left(\frac{2\pi m_p^{\text{eff}} kT}{h^2} \right)^{\frac{3}{2}} \quad (2.5)$$

Here N_V and N_C are containing the effective electron mass m_e^{eff} and the effective hole mass m_p^{eff} respectively. Those effective masses are the apparent masses of particles inside a crystal lattice which can be larger or smaller than the masses of free particles [6]. It is important to mention that for intrinsic semiconductors the fermi level E_F^i lies approximately in the middle of the band gap at room temperature, i.e. $E_F^i \approx \frac{E_C + E_V}{2}$ with E_C and E_V as the energy of the conduction respectively valence band [6]. This is no longer valid for doped semiconductors.

2.3 Doping of Semiconductors

Doping denotes a process of introducing impurities (dopants) into a semiconductor (see figure 2.2) in order to change its band structure which consequently changes the electrical characteristics too. Doped or impure semiconductors are called extrinsic [6].

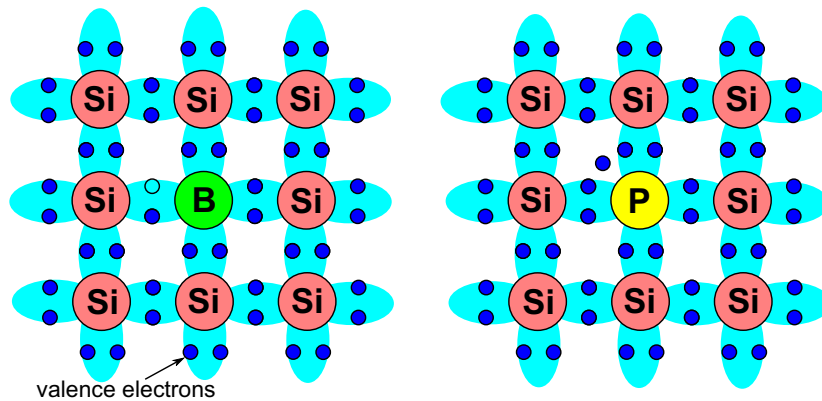


Figure 2.2: Left: Silicon doped with boron leading to p-type silicon due to the missing valence electron, right: Silicon doped with phosphorus leading to n-type silicon due to an additional valence electron.

Two different ways of doping, called n- and p-type, are possible. To get a n-type semiconductor one has to add atoms with one valence electron more than the basic semiconductor material has. Taking silicon as an example, elements of the group V like phosphorus or arsenic (called donators) would be added. Elements of the group III like boron or indium (called acceptors) which have one valence electron less than silicon would lead to a p-type doping.

The change of the electrical properties of doped semiconductors is dramatic even with a low doping concentration. For $T > 0$ K the thermal energy is usually high enough to raise all the

loose bound valence electrons of donor impurities into the conduction band. This results in a creation of a new energy level inside the band gap close to the lower edge of the conduction band. The open energy state of acceptors caused by the “missing” valence electron can be occupied by valence electrons of the surrounding semiconductor material. Because of that acceptors are generating a new energy state above the energy level of the valence band.

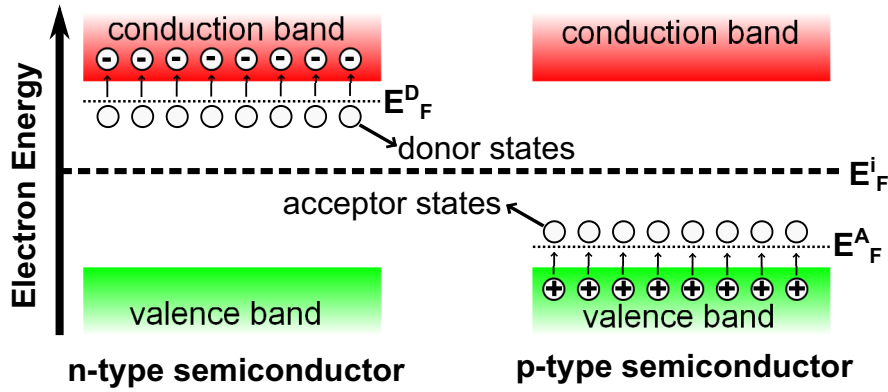


Figure 2.3: Band structure of a n-type (left) and p-type (right) semiconductor.

The introduction of new energy states inside the band gap also leads to a shift of the Fermi level. For n-type semiconductors the energy level is shifted towards the conduction band and can be calculated according to equation 2.6 [6]

$$E_F^D = E_C - kT \ln \left(\frac{N_C}{N_D} \right) \quad (2.6)$$

with N_D as the donor concentration. For p-type semiconductors the Fermi level is shifted to the valence band and can be calculated according to equation 2.7 [6]

$$E_F^A = E_V - kT \ln \left(\frac{N_A}{N_V} \right) \quad (2.7)$$

with N_A as the acceptor concentration. Equations 2.6 and 2.7 are valid under the assumption that all electrons and holes are thermally excited into their according band. The donor concentration N_D is in this case equal to the electron density n and the acceptor concentration N_A is equal to the hole density p [6].

2.4 The p-n Junction or Diode

Merging n- and p-type semiconductors leads to the so-called p-n junction (see figure 2.4). It is one of the fundamental devices of electronic engineering and also known as diode. If two differently doped semiconductors are brought together electrons begin to diffuse from

the n-type to the p-type material recombining there with holes. Vice versa this happens for holes in the p-type material due the large carrier concentration gradient for differently doped semiconductors [6]. However, both acceptor and donor ions are bound in the crystal lattice and are unable to move. The result is the formation of a so-called space charge region (or depletion region) at the actual junction, a region completely empty of free charge carriers. The spread of this region depends among others on the acceptor and donator concentrations and continues as long as the electric field formed by the bound dopant ions is high enough to stop the diffusion process.

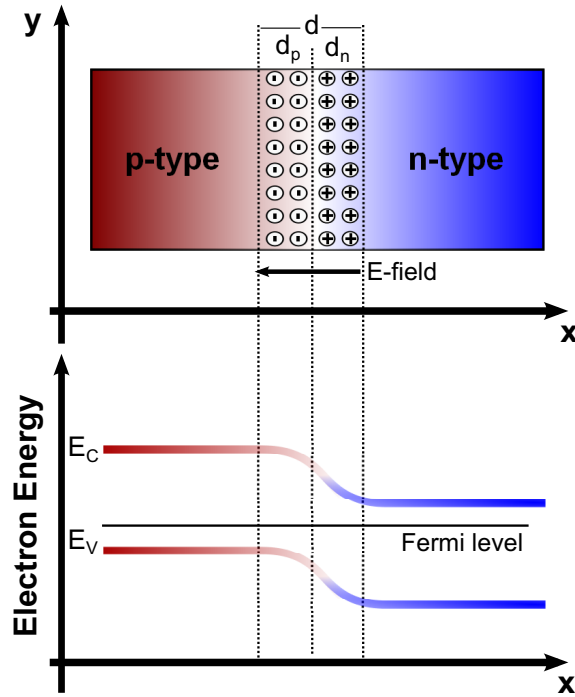


Figure 2.4: Top: P-n junction showing the depletion region, bottom: Band structure.

The resulting potential difference of the positively charged n- and negatively charged p-side is called built-in voltage V_{bi} . At thermal equilibrium this voltage can be calculated using equation 2.8 with e as the elementary charge [6].

$$V_{bi} = \frac{kT}{e} \ln \left(\frac{N_A N_D}{n_i^2} \right) \quad (2.8)$$

The width of the depletion region d is the sum of the widths of the depleted areas inside the n- and p-type material, d_n and d_p , and can be calculated according to equation 2.9 [6] where ϵ_0 corresponds to the vacuum permittivity and ϵ_r to the relative permittivity of silicon.

$$d = d_n + d_p = \left(\frac{1}{N_A} + \frac{1}{N_D} \right) \cdot \sqrt{\frac{2\epsilon_0\epsilon_r V_{bi}}{e} \cdot \left(\frac{1}{N_A} + \frac{1}{N_D} \right)^{-1}} = \sqrt{\frac{2\epsilon_0\epsilon_r V_{bi}}{e} \cdot \frac{N_A + N_D}{N_A N_D}} \quad (2.9)$$

If the acceptor and donator concentrations are identical, the depletion region will grow equally in both areas. Generally the depletion region will grow deeper into the less doped material if one concentration is higher than the other.

2.4.1 Current-Voltage Characteristics

The current-voltage characteristics of a p-n junction strongly depends on the polarity of the external applied voltage source. Two different types of voltage configurations exist which correspond to either the forward biased or reverse biased mode.

The p-n junction is called forward biased if the positive pole is connected to the p-type semiconductor and the negative pole to the n-type. This biasing configuration along with positive applied voltages reduces the potential barrier of the depletion region. It allows electrons to reach the p-type region and holes to reach the n-type region easier. As a result the width of the depletion layer shrinks by an increase of the external applied voltage until the whole depletion layer vanishes (in particular if $V_{\text{ext}} = |V_{\text{bi}}^{\text{Si}}| \approx 0.7 \text{ V}$). A further increase of the external voltage beyond this value leads to an electrical current flowing through the p-n junction.

A change of the polarity of the applied external voltage source results in reverse biasing. In this case electrons and holes tend to move towards the external electrodes. The potential barrier and the depletion layer width increase. However, charge carriers can still be thermally excited inside the depleted volume. This excitation of charge carriers results in a so called leakage or dark current $I_0(T)$ which is temperature dependent. The leakage current is a volume generated current and in general very small. If the reverse bias voltage exceeds a specific value, the p-n junction will break down and an exponentially increasing current will flow. This breakthrough process is reversible as long as the current is small enough. The current-voltage characteristic in reverse bias mode are displayed in figure 2.5.

The above described current-voltage behaviours of the p-n junction are mathematically summarised by the Shockley equation:

$$I(T) = I_0(T) \cdot \left(\exp\left(\frac{qV}{kT}\right) - 1 \right) \quad (2.10)$$

which has validity for reverse and forward biasing³. In case of forward biasing (i.e. $V > 0$), the current exponentially increases with the voltage. Furthermore, the exponential growth itself is temperature dependent. If the p-n junction is operated in reverse bias mode (i.e. $V < 0$), the current will eventually saturate at $I_0(T)$ if the voltage is tuned to values far below 0 V (see equation 2.11).

$$\lim_{V \rightarrow -\infty} I_0(T) \cdot \left(\exp\left(\frac{qV}{kT}\right) - 1 \right) = I_0(T) \quad (2.11)$$

³ In equation 2.10 it is assumed that the positive pole of the external voltage source is connected to the p-side and the negative pole to the n-side of the p-n junction.

For both biasing methods the width of the depletion region can still be calculated using equation 2.9 when substituting $V_{bi} \rightarrow V_{bi} - V$ and that forward biasing corresponds to positive voltages V .

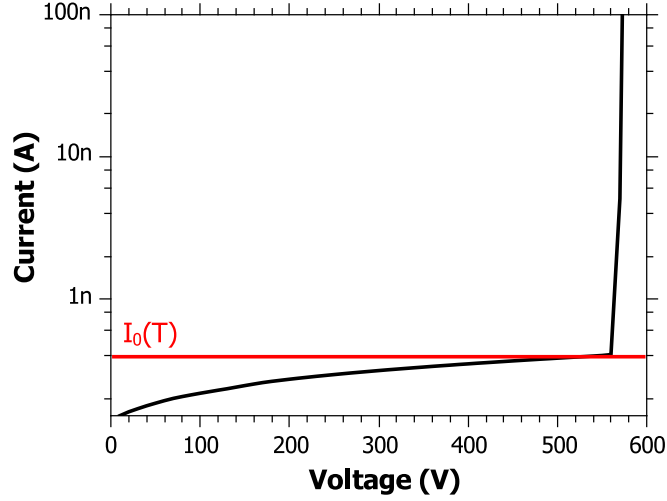


Figure 2.5: Current-voltage characteristics of a p-n junction operated in reverse bias mode.

2.4.2 Capacitance-Voltage Characteristics

The capacitance-voltage characteristics of a p-n junction can easily be understood when thinking of a parallel plate capacitor. The capacitor plates correspond to the non-depleted area of the doped semiconductor material and the capacitor dielectric is corresponding to the depletion region. For a parallel plate capacitor the capacitance can be calculated according to equation 2.12 where A is equal to the area of the capacitor plates and d to the thickness of the dielectric between them.

$$C = \epsilon_0 \epsilon_r \frac{A}{d} \quad (2.12)$$

If one replaces the distance d with the expression of the width of the depletion region with applied external voltage in equation 2.12, the equation 2.13 can be derived.

$$C = A \cdot \sqrt{\frac{e \epsilon_0 \epsilon_r N_A N_D}{2(N_A + N_D) \cdot (V_{bi} - V)}} \quad (2.13)$$

In semiconductor industries the resistivity $\rho = [e \cdot (n\mu_n + p\mu_p)]^{-1}$, where μ_n respectively μ_p are the mobilities of electrons respectively holes, is a more commonly used expression rather than the dopant concentrations N_A respectively N_D . Using the resistivity and assuming that one

concentration is much higher than the other (e.g. $N_D \gg N_A$), one can obtain the capacitance of a p-n junction according to equation 2.14.

$$C = A \cdot \sqrt{\frac{\epsilon_0 \epsilon_r}{2\rho\mu \cdot (V_{bi} - V)}} \quad (2.14)$$

Equation 2.14 is valid at room temperature (i.e. $N_A \approx p$ and $N_D \approx n$).

If the p-n junction is operated in reverse bias mode, an increase in voltage leads to an increase of the width of the depletion layer. The capacitance consequently gets less until the depleted volume covers the whole semiconductor device. A further increase in voltage will then not lead to a further decrease in capacitance anymore. The voltage at full depletion is called full depletion voltage V_{depl} and can be fitted from $1/C^2$ vs. V plots (see figure 2.6).

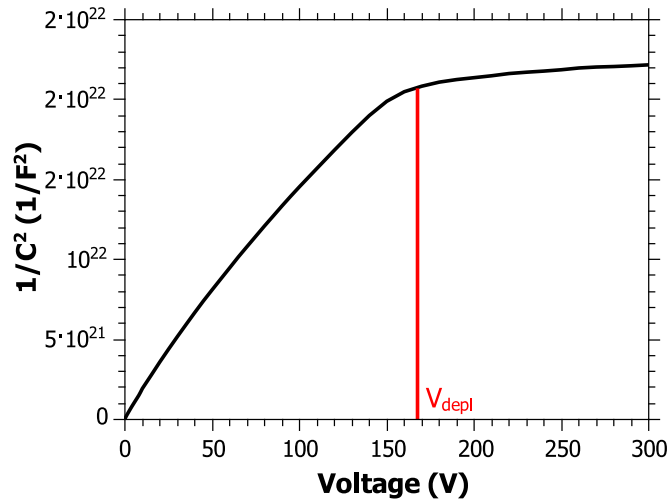


Figure 2.6: Capacitance-voltage characteristics of a p-n junction operated in reverse bias mode.

A formula for the full depletion voltage (see equation 2.15) can be derived if equations 2.12 and 2.14 are equated and if it is again assumed that one dopant concentration (now called N) is significantly higher than the other.

$$V_{\text{depl}} \approx \frac{eNd_{\text{max}}^2}{2\epsilon_0\epsilon_r} \quad (2.15)$$

d_{max} corresponds to the maximum width of the depletion region (i.e. if the device is completely depleted).

3 Silicon Strip Sensors for Particle Physics Experiments

Silicon strip sensors are frequently used and well established in many particle physics experiments like CMS for the detection of ionising radiation. The design provides a one dimensional spacial information at which location an incident particle hits the sensor. Silicon strip sensors are designed and built in many different ways due to specific requirements of individual particle physics experiments. The following sections will restrict to sensors currently used in CMS having one of the most basic designs.

3.1 Working Principle

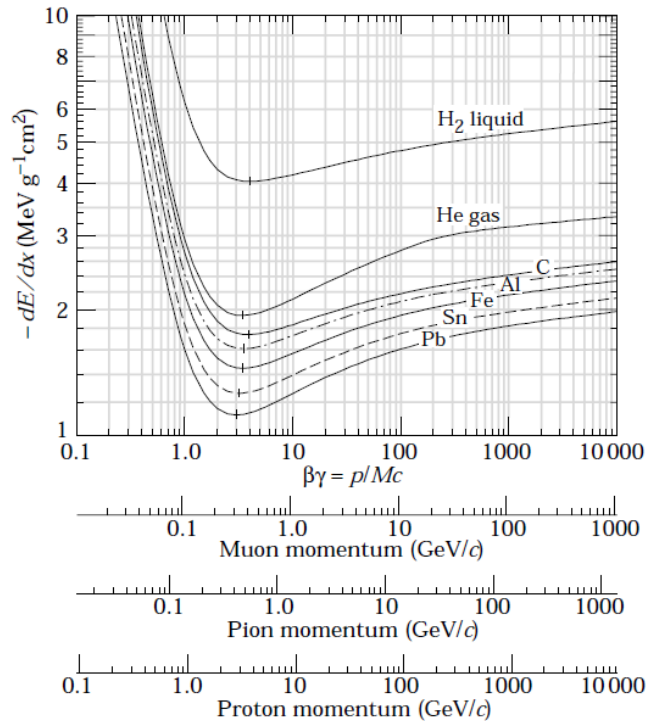


Figure 3.1: Energy loss for different particles passing through different materials [7].

As a first approximation silicon strip sensors can be compared to diodes operated in reverse bias mode. The depleted volume is the detector which is sensitive to charged particles. If

such particles are passing through matter, they mainly interact via the coulomb interaction and lose at least a fraction of their initial energy¹ (see figure 3.1).

In silicon this energy deposition causes the production of electron hole pairs inside the depleted volume. They subsequently propagate towards the electrodes which results in a measurable electrical signal due to the applied external electrical field.

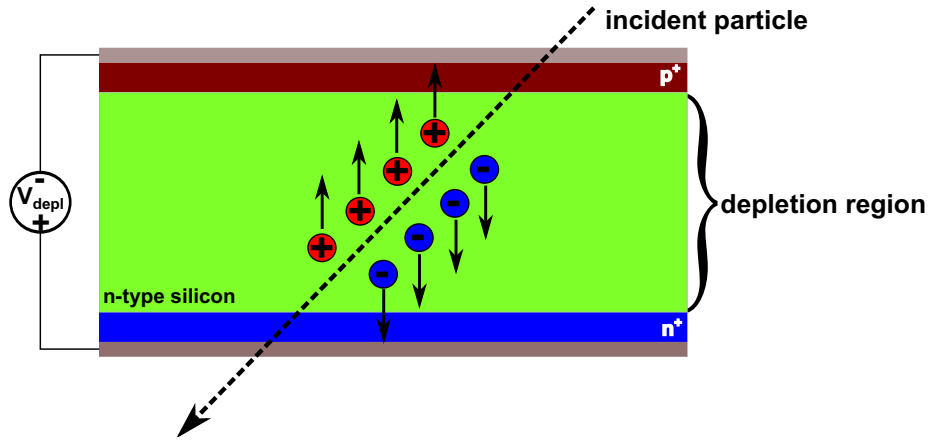


Figure 3.2: Creation of electron hole pairs inside the depleted volume caused by a traversing charged particle.

The amount of generated charge carriers can be calculated under the constraint of considering only minimum ionizing particles (MIP's). MIP's are classified as particles whose mean energy loss for a specific material is minimal. This consideration is valid because almost all particles produced in LHC collisions are MIP's. Dividing the energy deposited by a MIP E_{MIP} by the energy to create an electron hole pair E_{eh} leads to the number of generated charge carriers N [8].

$$N = \frac{E_{\text{MIP}}}{E_{\text{eh}}} \quad (3.1)$$

A MIP generates about 22,500 electron hole pairs for standard 300 μm thick sensors [8]. However, the intrinsic charge carrier density at room temperature is $n_i \approx 8.72 \cdot 10^9 \text{ cm}^{-3}$ which is several magnitudes larger. Due to the several magnitudes larger intrinsic carrier density the actual signal could be a statistical anomaly, thus unable to detect. Hence a p-n junction is necessary to deplete the silicon of the intrinsic charge carriers in order to be able to detect MIPs.

¹In general the energy loss of charged particles in matter can be described by the Bethe-Bloch equation.

3.2 Sensor Design

The p-n junction of a silicon strip sensor is separated into strips in order to gain a spatial resolution of incident charged particles in the order of $10\ \mu\text{m}$. The signal of each strip can be individually read out, thus leading to a one dimensional spatial resolution. Along with stacked and twisted layers of sensors a fully three dimensional track resolution (tracking) is possible.

One dimensional resolution achieved with a separation of the p-n junction is the basic idea behind a silicon strip sensor but many other things have to be considered too in order to obtain a fully functional sensor. The following sections provide a detailed insight into the most important parts of modern silicon strip sensors (see figure 3.3). A detailed description on how those parts are manufactured gives [9].

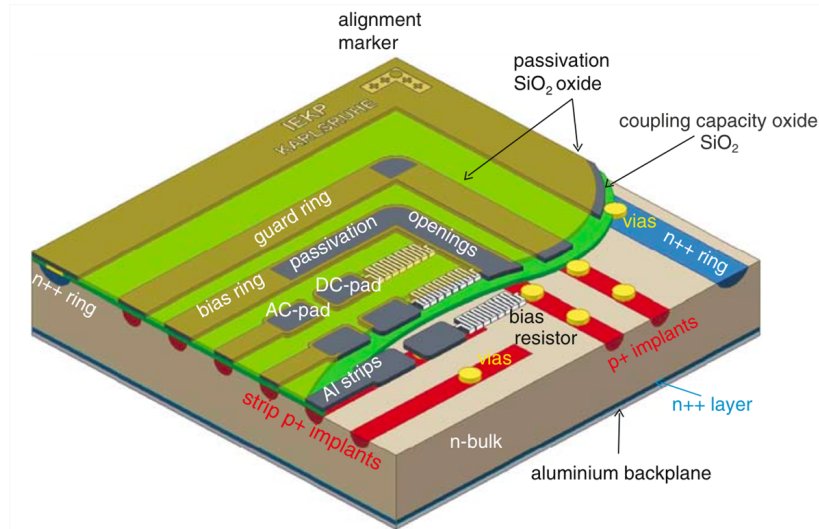


Figure 3.3: Schematic 3D-view of a silicon strip sensor [10].

3.2.1 The Silicon Base or Bulk Material

A technically feasible usage of silicon strip sensors requires a low full depletion voltage which corresponds to a high resistivity of the base material. The resistivity dependence of the full depletion voltage can be obtained from equation 2.14 and is displayed in equation 3.2.

$$V_{\text{depl}} \approx \frac{A^2 \epsilon_0 \epsilon_r}{2\mu C_{\text{min}}^2} \cdot \frac{1}{\rho} \quad (3.2)$$

Furthermore, the full depletion voltage changes for heavily irradiated sensors due to a change of the effective doping concentration (for a detailed description see chapter 9). Thus, the lifetime of a sensor depends on the exposed radiation dose and the maximum voltage the

power supplies can provide. Too heavily irradiated sensors cannot be completely depleted anymore ($V_{\text{depl}} > V_{\text{max}}$) which results in an effective smaller signal to noise ratio. This is one of the major reasons why the CMS tracker will be completely exchanged. Sensors currently used in CMS are made out of n-type base material with different resistivities. Sensors of the inner layers have a resistivity between 1.5 k Ω cm and 3 k Ω cm whereas sensors of the outer layer have a resistivity between 3.5 k Ω cm and 7.5 k Ω cm [8]. Such high resistive materials contain only a small amount of impurities and are usually manufactured using the Float-Zone process [9]. An ingot of silicon with a well-defined resistivity is cut into wafers which are serving as a raw material for semiconductor industries.

3.2.2 Strip and Backside Implantation

The segmentation of n-type silicon strip sensors is performed by implanting strips of acceptor impurities into the base material. The concentration of those impurities has to be significantly higher than those for the base material (denoted with p^+) so that the depletion region will grow deeper into the bulk of the sensor than into the strip (see equation 2.9). Moreover, a higher strip impurity concentration along with small pitches ensure a good strip isolation since the depletion region covers the area between strips already for bias voltages which are much lower than the full depletion voltage.

The pitch of strips can vary between several tens of micrometers and has an important impact on the resolution of silicon strip sensors. On the one hand the resolution of a sensor is limited technically (i.e. minimum technical achievable pitch) and on the other hand by physical reasons. The physical limitation is given by diffusion effects of the charges inside the silicon bulk material which are generated by traversing ionising particles (i.e. the size of the so called charge cloud). However, the technical limit is anyhow larger ($\approx 50 \mu\text{m}$ pitch) so the physical limitations can be neglected.

A way of improving the resolution with a moderate pitch is the center of gravity technique which can be used when the charge is read out analogue between adjacent strips.

Similar to the strips also the backside of a sensor is doped with a high concentration of donor impurities (denoted as n^+). This ensures a good ohmic contact between the aluminum layer beneath the implantation, serving as one of the biasing electrodes.

The depths of both implantations are very small as compared to the sensor thickness (i.e. 1.5 μm). However, the crucial parameter is, as already mentioned before, the concentration of implanted impurities which is several magnitudes larger than impurity concentration of the base material.

3.2.3 Signal Coupling

The signal of a sensor can be transmitted in two possible ways to readout electronics. Generally two circuits, the biasing and the signal circuit, exist. If both circuits are shorted, the signal coupling is called DC coupled. This coupling method transfers the actual signal but also the

leakage current. DC coupling can be used if the dark current is small enough which also corresponds to a low noise. This coupling method is especially used for pixel sensors due to their comparatively small area which causes only small leakage currents to flow. Moreover, the readout electronics should be able to handle a continuous current flow.

The second method transmits only the AC signal generated by traversing particles. Sensors using this method are called AC coupled. In particular, a capacitive coupling between the strips and the readout electronics ensures that only the signal itself is transmitted. This coupling method is commonly used for strip sensors due to their comparatively high dark current. The coupling capacitance itself can be applied externally or directly on the sensor. Sensors using a built-in coupling capacitance have an additional dielectric layer between the strip implantation and the covering aluminium layer. Usually silicon dioxide (SiO_2) is used but also a composition of two layers of different materials is possible.

3.2.4 Ring Structures

Biasing of a sensor is performed by using a so-called bias ring which is connected to every strip via resistors made out of polycrystalline silicon. The bias ring consists of a p^+ implantation which is covered by a layer of aluminum. It comprises the whole sensor and serves as one of the biasing electrodes. The polycrystalline silicon resistors ensure that all strips have the same potential as the bias ring. Beside this function they also serve as a current protection. For the usually used bias configuration the bias ring is connected to ground and the backside of the sensor to a positive potential.

In order to obtain a well-defined depletion region a ring of n^+ , the so-called edge ring, is implanted at the outermost edges of a sensor. As a consequence an ohmic connection between the edge ring and the backplane is achieved due to the fact that the bulk and the backside of a sensor are also n respectively n^+ doped. Thus, the edge ring has the same potential as the backplane which impedes the depletion region to grow any further. It also protects the depletion region from impurities or lattice defects located at the edges of the sensor which would lead to a significantly higher leakage current.

The guard ring is used to increase the breakdown voltage of a sensor. It is again a p^+ doped ring structure which surrounds all strips and the bias ring. It adjusts the potential difference between the bias and the edge ring preventing the occurrence of high electrical fields near the surface. In general various designs of guard ring structures are possible. Sensors built for the CMS tracker for example use only one guard ring with a floating potential. However, also more than one guard ring with varying applied potentials can be used to shape the electrical field.

3.2.5 Passivation

The passivation layer protects a sensor from environmental influences like mechanical damage, moisture or impurities and moreover serves as a chemical barrier. It also serves as an electrical

isolation which makes the passivation usually high resistive. It is the uppermost layer of a sensor covering its whole surface. Several materials like silicon nitride (Si_3N_4), silicon dioxide (SiO_2) or phosphor silicate glass (PSG) can be used. Silicon nitride for example is a commonly used material in semiconductor industries due to its diffusion barrier qualities. Sometimes more than one passivation layer is used which can impact sensors parameters in a positive but also negative way.

3.2.6 Pad Structures

Pad structures are used to connect a sensor to readout electronics and to perform quality tests. To obtain such structures windows inside the passivation layer have to be etched. Every strip of a sensor then has at least two pads, the so-called AC- and DC-pad which are enlarged areas of aluminum providing an easier way of contacting by the use of probe needles. The AC-pad is intended to transmit the AC coupled signal of a sensor and the DC-pad to perform quality tests like measurements of the single strip leakage current (also the AC-pads are necessary for individual quality tests). The DC-pad is directly connected to the p^+ implantation of the strip through contact holes which avoids a capacitive coupling. The aluminum layers of the ring structures are also connected via contact holes to the implanted area. This is necessary due to the fact that a thin layer of SiO_2 covers the bulk due to natural oxidation processes.

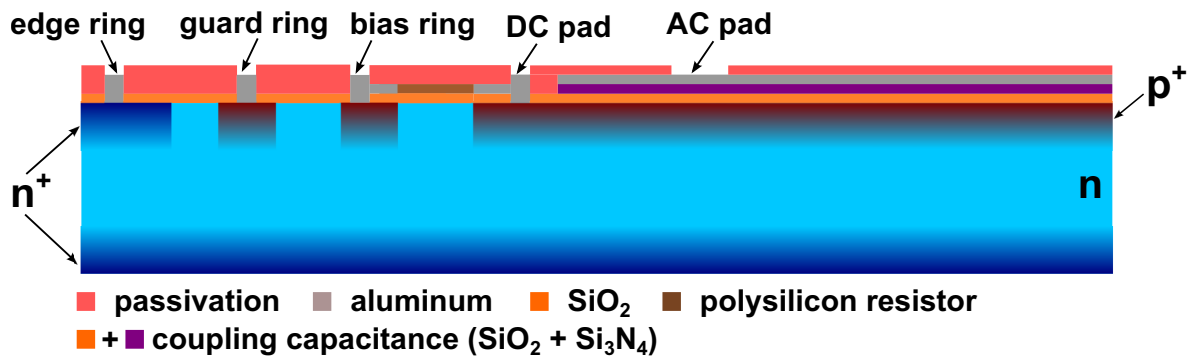


Figure 3.4: Cross section through a strip of a silicon strip sensor.

4 Silicon Strip Sensors Manufactured by Infineon Technologies Austria AG

The quantity of required sensors for the CMS tracker upgrade exceeds the production capacity of scientific institutes. Thus, an industrial fabrication is obligatory. In 2009 the Institute of High Energy Physics of the Austrian Academy of Sciences (HEPHY) and Infineon Technologies Austria AG (Infineon) started a collaboration on the development of silicon strip sensors intended for the CMS tracker upgrade. The intention behind this collaboration is to establish Infineon as a second vendor for silicon strip sensors due to the monopoly position of the up to then only vendor. The advantages manifest in a price stability and assured availability of sensors. In total 50 prototype wafers were ordered for evaluation purposes. Most of the ordered sensor were already delivered and are showing in general very encouraging results.

4.1 Wafer Layout

A description of the single sensors on a fully processed wafer will be valuable. The sensor design is similar to ones used currently in CMS meaning p-type strips implanted in n-type bulk material and was entirely developed by HEPHY.

The wafers itself have a diameter of 6 inch, a thickness of 300 μm and comprise in total 6 sensors and several test structures whereas each of them was designed for a specific purpose (see figure 4.1). The following sensors are located on each wafer:

- **STL**: The largest sensor called STL comes closest to currently in CMS used sensors by means of the active volume and the number of strips. Nevertheless, this sensor is not frequently used for tests due to the relatively high strip number which results in an extensive electrical characterisation.
- **STS**: The sensor called STS is used for several tests including beam tests at accelerator facilities but also readout tests using a radioactive source at HEPHY. This sensor is frequently used for quality tests due to its comparatively small number of strips which results in a faster electrical characterisation.
- **SX2**: The SX2 sensor is very similar to the STS with the exception that every strip is segmented into two strips while both of them are connected via polysilicon resistors to the bias line. This design concept is especially interesting since a similar one will probably be used for sensors built for the CMS tracker upgrade (see chapter 10). Electrical

measurements are again not frequently conducted for this type sensor due to the fact that it has the same number of strips as the STL which hinders a fast characterisation.

- **STI:** Sensors used for neutron irradiation studies are called STI. They perfectly fit into tubes used for irradiations (see chapter 9) due to their comparatively small size. On every wafer two STI sensors exist and are denoted with STI1 and STI2 respectively.
- **STN:** The number of strips and the active volume of a STN sensor are equal to those of a STI sensor. However, the layer of Si_3N_4 acting together with the layer of SiO_2 as a dielectric is for this sensor type not restricted to the area of the implanted strips. Instead, the layer of Si_3N_4 covers the whole sensor surface.

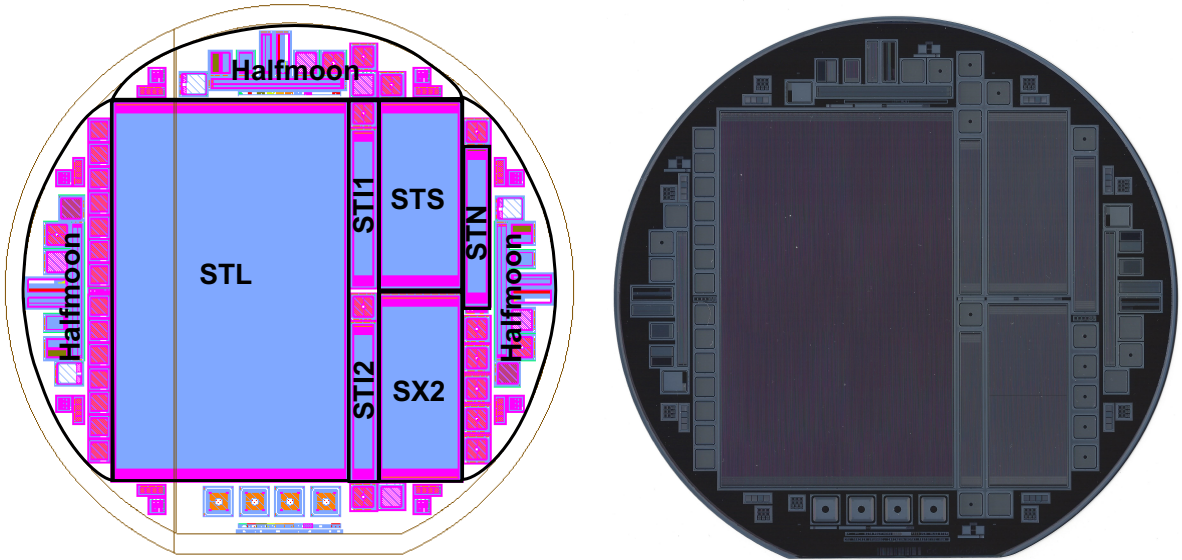


Figure 4.1: Wafer layout. Left: Schematic view, right: Fully processed wafer.

The most important sensor parameters are summarised in table 4.1.

Sensor type	Length (cm)	Width (cm)	Active volume (cm^3)	No. of strips	Pitch (μm)
STL	10.185	6.377	1.853	512	120
STS	5.051	2.285	0.305	256	80
SX2	5.051	2.285	0.305	2×256	80
STI 1&2	4.3	0.749	0.068	64	60
STN	4.3	0.749	0.068	64	60

Table 4.1: Parameters of sensors produced by Infineon Technologies Austria AG.

Test structures for quality and process control are located around the wafer edges (which are called halfmoons) to achieve an optimal utilization of the wafer area. The design of these structures is similar to those produced for the current CMS tracker. However, each test

object is built for a specific type of measurement like measurements of sheet resistances or interstrip parameters. A total of 32 diodes with three different designs are used for irradiation studies and measurements of global parameters like current-voltage and capacitance-voltage characteristics. Overall seven metal-oxid-semiconductor (MOS) structures are used to measure the charge density inside the SiO_2 and the $\text{SiO}_2 + \text{Si}_3\text{N}_4$ dielectric sandwich layer, respectively.

5 Sensor Characterisation at HEPHY

5.1 Quality Test Setup

The quality test setup (QTC) is used to perform measurements of single strip parameters on silicon strip sensors. It is a semiautomatic test equipment meaning that it measures the parameters of every strip automatically after an initial sensor alignment procedure. This becomes possible by the use of a x-y-z table which is controlled by a LabVIEW software. This table can move micron-precise in all three dimensions so every strip can be connected with stationary positioners. The electrical measurements are performed by connecting probe needles via micro positioners and the use of the x-y-z table to the bias ring, DC- and AC-pad. A switching matrix is used to interconnect the contacted sensor structures with the measurement instruments. The interconnection and measurements are again LabVIEW controlled. An aluminum vacuum support located on top of the x-y-z table is used to retain the sensor and to ensure a conductive connection to the sensors backplane. The x-y-z table along with the vacuum support, a microscope for precise contacting during the alignment process and positioners with incorporated probe needles are located inside a metallic light tight box which is acting as a Faraday Cage. Furthermore, the box prevents the intrusion of light which is of high importance since photons are able to produce electron hole pairs inside the depleted sensor volume resulting in a significantly higher leakage current. The measurement instruments are located outside of the box and are connected via a feed through to the positioners and vacuum support. Figure 5.1 shows the whole QTC setup including its measurement instruments.

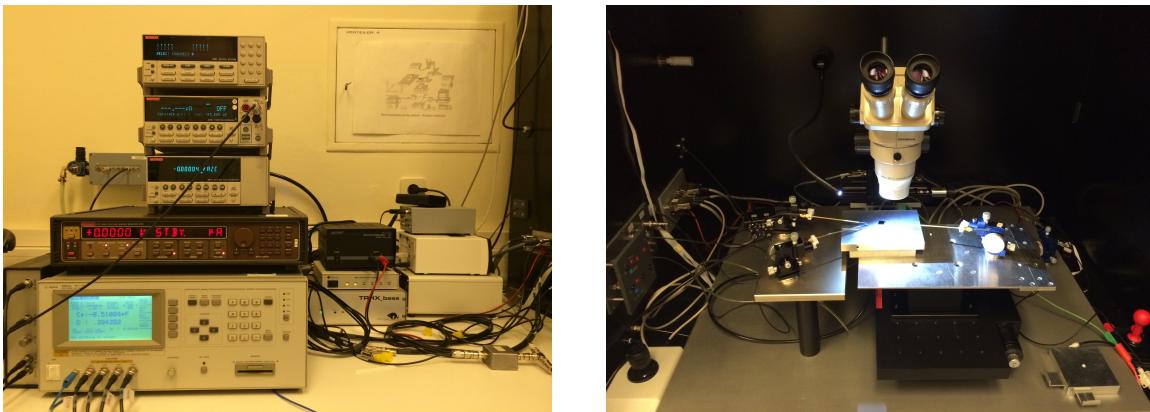


Figure 5.1: Quality Test Setup. Left: Measurement Instruments, Right: Interior of the light tight box.

A sensor is considered to be completely characterised by knowing its global and main strip parameters. The electrical characterisation is realised with the following measurement instruments: Keithley 237 (SMU), Keithley 2410 (SMU), Keithley 6514 (electrometer) and Agilent 4284A (LCR meter). For the interconnection between sensor structures and measurement instruments a Keithley 7001 switching matrix frame is used. In addition a decoupling box prevents high voltages at the inputs of the LCR meter.

The main single strip parameters for a sensor qualification are:

- Single strip leakage current – I_{strip}
- Polysilicon resistance – R_{poly}
- Coupling capacitance – C_{ac}
- Current through the dielectric layer – I_{diel}

Usually these four parameters are adequate. A good sensor shows uniform parameters over its whole area. I_{strip} should be sufficiently small and C_{ac} and R_{poly} sufficiently large. I_{diel} instead is used to detect so-called pinholes, shorts between the implant and the aluminum layer. In addition optional measurements like interstrip resistances and capacitances can be carried out providing a more substantiated characterisation.

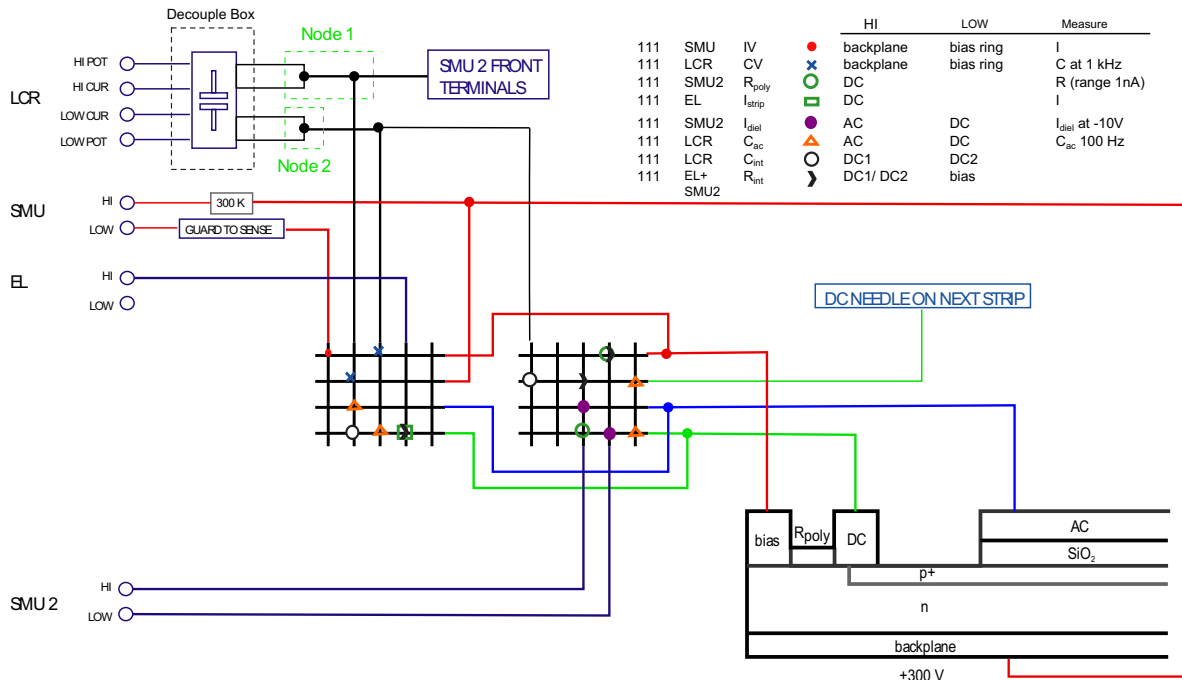


Figure 5.2: Switching system used for sensor characterisation.

A detailed description of the circuitry which is used to measure single strip parameters is given in figure 5.2. All parameters are measured slightly above the full depletion voltage. In particular, this voltage is set to 300 V for sensors of Infineon. Beside single strip parameters

global parameters (i.e. current-voltage and capacitance-voltage characteristics) which are equal to those of ordinary diodes can be measured by using this setup.

5.2 Process Quality Control Setup

The process quality control setup (PQC) is used to perform non standardized measurements on sensors and test structures. One of its main advantages is its flexibility leading to a large variety of possible measurements. It is very similar to the QTC with the exception that semiautomatic single strip measurements cannot be performed due to the lack of a motorized x-y-z table. A special feature of the PQC is that it contains vacuum support which can be heated or cooled by a Peltier-Element. This feature is of particular interest for measurements performed on irradiated structures¹. The heat loss of the Peltier-Element is compensated by an additional chiller which cools the backside. An inlet for dry air prohibits the emergence of condensed water which can harm the sensitive electronics if the vacuum support is cooled to temperatures below the dew point. To trap the dry air inside the PQC a glove box is installed allowing the handling of structures while the the Peltier-Element is activated. The installation of the peltier element and its properties are described in more details in [11].



Figure 5.3: Process quality control setup. Left: Measurement Instruments, Right: Interior of the light tight box showing the vacuum support with a incorporated Peltier-Element inside a glove box.

As well as for the QTC a metallic light tight box, several positioners along with probe needles and a microscope for precise contacting are belonging to this setup. Likewise all measurement instruments of the QTC are also available at the PQC. Figure 5.3 shows the PQC setup with its measurement instruments.

¹In general irradiated structures have to be cooled during a measurement to prevent a degradation of their characteristics (a more detailed explanation gives chapter 9).

6 Previous Measurement Results

This chapter discusses already previously performed measurements on silicon strip sensors produced by Infineon. As a first attempt two prototype batches containing 35 wafers and additional single sensors were delivered to HEPHY. Selected process steps were carried out using different manufacturing techniques in order to attain optimal process parameters for a future mass production. This approach results in so-called split groups, i.e. groups of wafers where one or more process steps are manufactured in a different way compared to others.

Most of the sensors of the first two batches were already characterised and are showing in general reasonable measurement results [9]. However, the measurements also reveal that there is still space for improvements concerning sensor design and manufacturing.

6.1 First Batch

The first batch comprises 24 wafers in total. Four different techniques for the oxidation process of the dielectric layer were applied and in addition three different diffusion techniques for the backside implantation. This results in 12 split groups within batch 1 (a detailed table of the split groups for batch 1 can be found in [9]). Nearly all sensors behave well and are showing encouraging strip values [9]. However, an area of defective strips is clearly visible. This area can be observed on every type of sensor and for every split group. The measurement results of R_{poly} are displayed in figure 6.1 exhibits particularly clear this distinct area of deviating values.

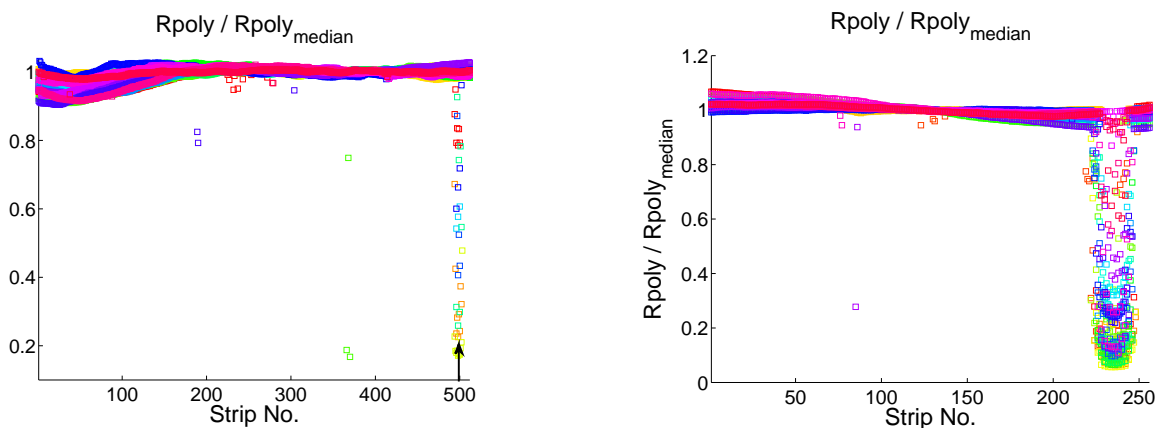


Figure 6.1: Measured R_{poly} for sensors of batch 1. Left: STL sensors, right: STS sensors [9].

It is important to mention that not only R_{poly} is affected but every other strip parameter too (i.e. I_{strip} , C_{ac} and I_{diel}). However, the current trough the dielectric layer I_{diel} is not that heavily affected like the other parameters.

The measured CV and IV characteristics showed promising results meaning that the full depletion voltage V_{depl} is uniform and in general comparatively low [9]. This does not apply for a specific split group processed using a special backside implantation technique. Sensors of this split group show a very low global leakage current but an early breakthrough. This backside implantation technique will no longer be used for later batches.

6.2 Second Batch

11 wafers are belonging to the second prototype batch. Three different variations of the R_{poly} implant dose (split 1), two different methods for the reduction of the leakage current (split2) and two techniques for the backside implantation (split3) were applied. Thus, 12 split groups exist within batch 2 (see table 6.1).

Wafer no.	Split 1 – Split 2 – Split 3	Wafer no.	Split 1 – Split 2 – Split 3
01	A-A-A	07	A-B-A
02	A-A-B	08	A-B-B
03	B-A-A	09	B-B-A
04	B-A-B	10	B-B-B
05	C-A-A	11	C-B-A
06	C-A-B		

Table 6.1: Split groups of batch 2.

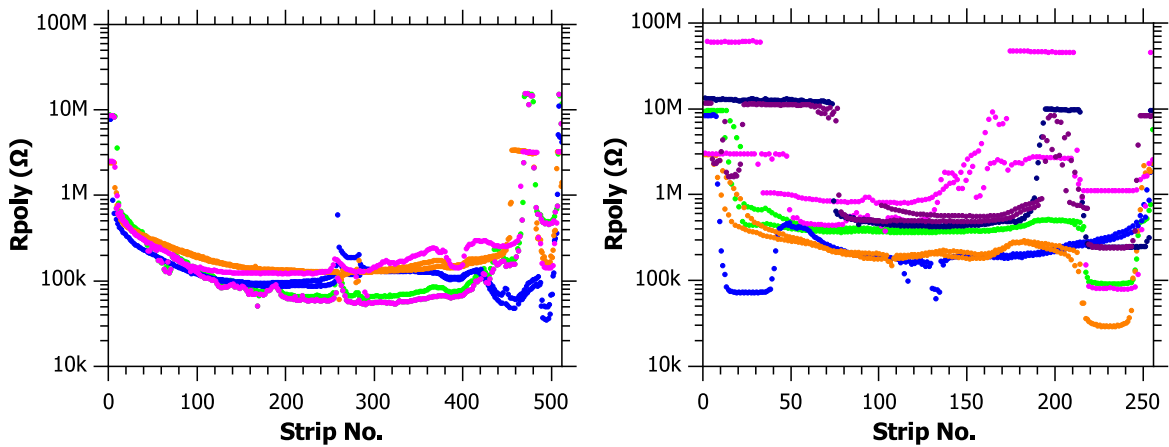


Figure 6.2: Measured R_{poly} for selected sensors of batch 2. Left: STL sensors, right: STS sensors.

As well as for the first prototype batch an area of defective strips is clearly visible for all sensors of batch 2. For batch 1 this area is confined to the far right of every sensor but measurements performed on sensors of batch 2 show an additional broad zone of defective strips located near the center. Again R_{poly} displays this issue best (see figure 6.2). The global sensor parameters are as good as for the first batch.

6.3 Analysis of the Area of defective Strips

Measurements of the first two prototype batches revealed that the observed area of defective strips concerning one sensor parameter correlates to the area observed for the other parameters. Hence, one global issue could affect all parameters resulting in deviating strip values.

By taking a closer look at the measured values of I_{strip} and R_{poly} (figure 6.3 left) it can be observed that lower values of R_{poly} correspond to higher values of I_{strip} at the defective area. This behaviour can be explained by a conductive interconnection between affected strips [9]. Thereby the measured I_{strip} is no longer the current of each strip, but in fact it is the sum of the single strip currents of the defective region. Shorted strips would lead to a measurement of a parallel circuit of several polysilicon resistors resulting in lower resistance values at the area of defective strips. An interconnection of strips is even more evident considering measurements of the inter strip resistance R_{int} (see figure 6.3 right). Usually this resistance is in the range of several $G\Omega$ but at the area of defective strips it reaches de facto zero.

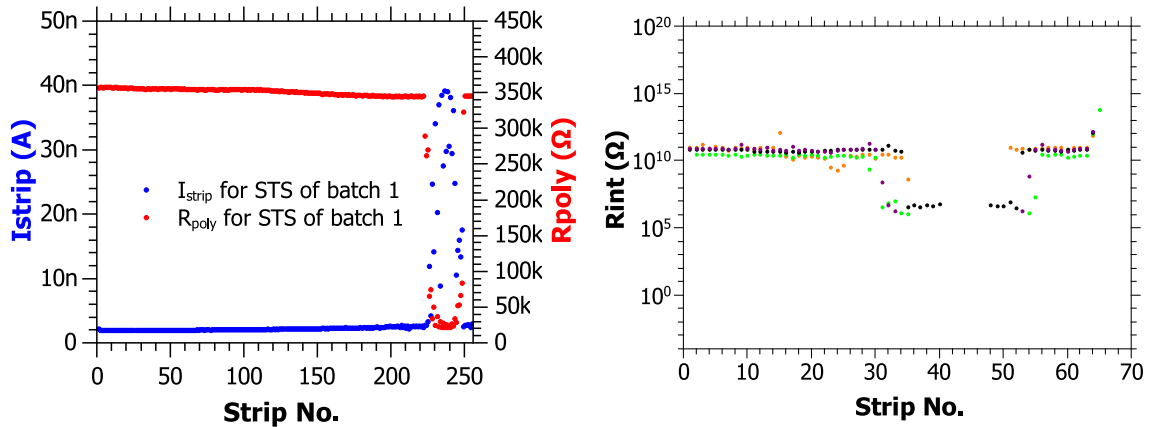


Figure 6.3: Left: I_{strip} and R_{poly} of a STS sensor of batch 1, right: Inter strip resistance of selected sensors of batch 1.

The following investigations presented in this thesis are based on the above described hypothesis of interconnected strips due to its strong plausibility. However, it is of utmost importance to know how the defective area can be removed in order to attain high-quality sensors for a future mass production. Furthermore, a physical understanding is necessary to prohibit a reoccurrence of this phenomenon.

7 Investigations of the Area of Defective Strips

The following sections will comprehensively discuss one particular issue which is most likely responsible for the area of defective strips. At first a possible process which is strongly related to the issue will be presented which provides a scientific explanation for the observed discrepancies. Furthermore, investigations on how to restore affected sensors and methods avoiding the occurrence of faulty strips will be presented. Improvements concerning specific manufacturing steps will also be investigated which provide valuable information for both Infineon and HEPHY. It is important to mention that these investigations will not be presented in the order they were carried out. This approach, however, will provide a better comprehensibility.

7.1 Field-Effect Transistor Measurements

At a first glance it is not clear which defect at which sensor layer is responsible for the conductive interconnection of strips described in chapter 6. However, due to the sensor design the interconnection of strips occurs most likely at the strip implant layer. The p^+ implanted strips are interconnected via the n-type bulk material which in general serves as a good insulator if the sensor is fully depleted. Thus, the bulk material has to change regional its properties to achieve a conductive interconnection. Taking a closer look at the structure of a silicon strip sensor reveals that it is very similar to the structure of a field-effect transistor (FET). In particular a so-called p-channel enhancement-mode isolated gate field-effect transistor (p-channel IGFET) comes closest to the sensor structure if two strips are considered (see figure 7.1). The working principle of such transistors is based on a conductive interconnection of two terminals achieved by a regional change of the properties of the intermediate bulk material. Thus, FET-like measurements on silicon strips sensors could provide a deeper insight into the area of defective strips caused by a conductive interconnection.

7.1.1 Theoretical Introduction

A p-channel IGFET has in total 4 terminals called drain, source, gate and backplane [12] (see figure 7.1). The drain and source terminals are regions of p^+ -type silicon implanted inside a n-type base material. The gate terminal is located in between the two p^+ terminals and separated from the bulk by an insulating material (usually SiO_2). Similar to silicon strip sensors the backplane connection is located at the bottom of the device usually made out of n^+ -type silicon ensuring a good ohmic contact to its covering aluminum layer.

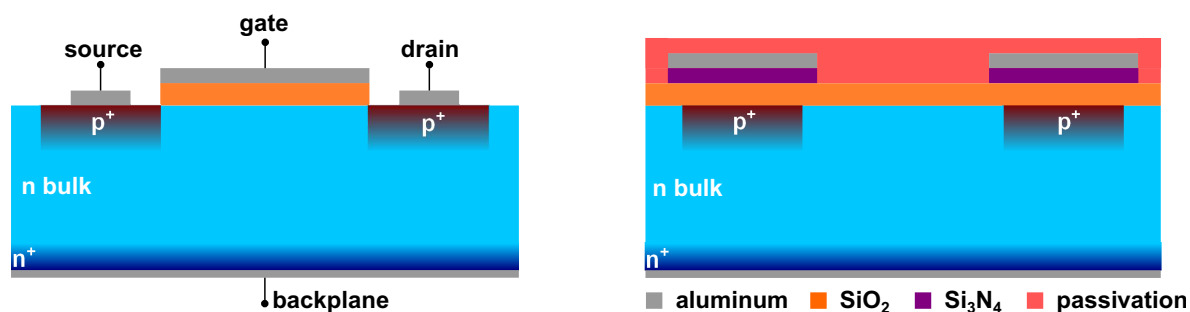


Figure 7.1: Cross section of a p-channel enhancement-mode IGFET (left) and a silicon strip sensor (right) showing that both devices are nearly identical.

As well as other transistor types the p-channel IGFET is commonly used as a switch. Unlike for bipolar transistors the opened or closed state of a FET is controlled via an externally applied potential difference between gate and source called V_{GS} . Connecting the negative pole of the gate-source voltage to the gate electrode causes an accumulation of electrons inside the gate electrode (see figure 7.2). Electrons inside the bulk material and beneath the gate electrode are consequently repelled and holes from the p⁺ regions attracted. This results in the generation of a conductive channel also called inversion layer beneath the gate connecting the two p⁺ regions. The maintenance of the inversion layer is assured by the high resistive layer of SiO₂ preventing the absorption of holes by the gate electrode. An applied potential difference between drain and source called V_{DS} then causes a current flow through the inversion layer. In particular positively charged holes flow and that is why the IGFET has the prescript “p-channel”. A further connection of the positive pole of the gate-source voltage to the backplane ensures the emergence of a depleted volume coating the inversion layer.

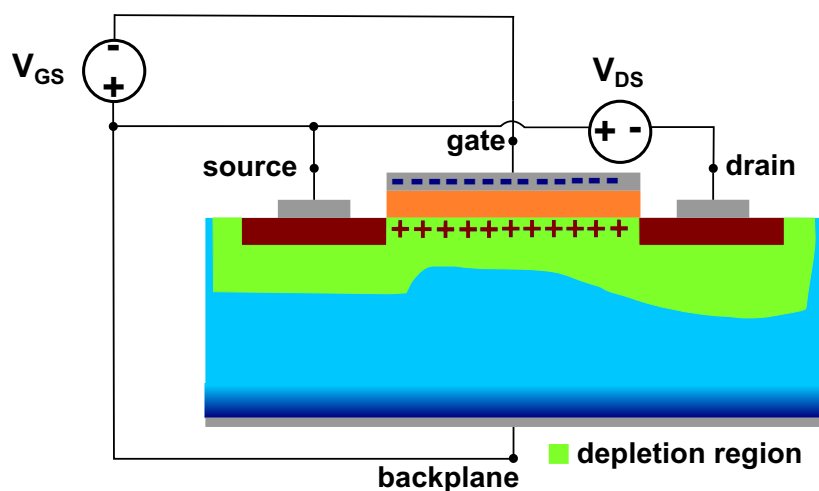


Figure 7.2: Working principle of a p-channel enhancement-mode IGFET. The depletion region beneath the source is wider due to its higher potential compared to the applied potential at the drain terminal.

Current-Voltage Characteristics of a P-Channel IGFET

The current flowing from source to drain I_D is on the one hand determined by the drain-source voltage V_{DS} and on the other hand by the gate-source voltage V_{GS} . To enable a current flow the gate-source voltage has to exceed a device specific value called threshold voltage V_T . This is necessary since the formed inversion layer does not reach the drain terminal for voltages lower than V_T . The result is that a conductive interconnection of drain and source is impossible and that no current will flow independently of the drain-source voltage. For gate-source voltages higher than V_T a current flow depending on the value of V_{DS} is the consequence. At first the current scales nearly linear with V_{DS} as long as it reaches a certain value. An increase of the drain-source voltages beyond this value results in a saturation of I_D . Saturation occurs when all holes inside the inversion layer contribute to the current conduction. Thus, higher drain-source voltages cannot effect higher currents anymore. An increase of the gate-source voltage enables a shift of the saturation region to higher drain-source voltages since more holes can contribute to the current conduction. The described current-voltage characteristics can be summarised by three equations according to the three mentioned regions [12]:

1. **Subthreshold region:** The gate-source voltage V_{GS} is below the threshold voltage V_T so no conductive interconnection of drain and source can be achieved. The current I_D is always zero independently of the drain-source voltage [12]:

$$I_D = 0 \text{ A.} \quad (7.1)$$

This represents of course the idealised case. Small leakage currents will flow in case of a real IGFET if the drain-source voltage is increased.

2. **Linear region:** V_{GS} exceeds the threshold voltage and V_{DS} is sufficiently small, i.e. $V_{GS} > V_T$ and $V_{DS} < V_{GS} - V_T$. Hence, an increase of V_{DS} results in an increase of I_D . The source-drain current can be calculated according to equation 7.2 for these boundary conditions [12].

$$I_D = \frac{\mu_p C_{\text{oxide}} W}{L} \left((V_{GS} - V_T) \cdot V_{DS} - \frac{V_{DS}^2}{2} \right) \quad (7.2)$$

Here μ_p corresponds to the hole mobility, C_{oxide} to the oxide capacitance, W to the width of the gate electrode and L to the length of the gate electrode.

3. **Saturation region:** V_{GS} exceeds the threshold voltage and V_{DS} is sufficiently high, i.e. $V_{GS} > V_T$ and $V_{DS} \geq V_{GS} - V_T$. Hence I_D remains constant if V_{DS} increases. The source-drain current can be calculated according to equation 7.3 for these boundary conditions [12].

$$I_D = \frac{\mu_p C_{\text{oxide}} W}{L} \frac{(V_{GS} - V_T)^2}{2} \quad (7.3)$$

Figure 7.3 displays the described characteristics for various gate-source voltages V_{GS} .

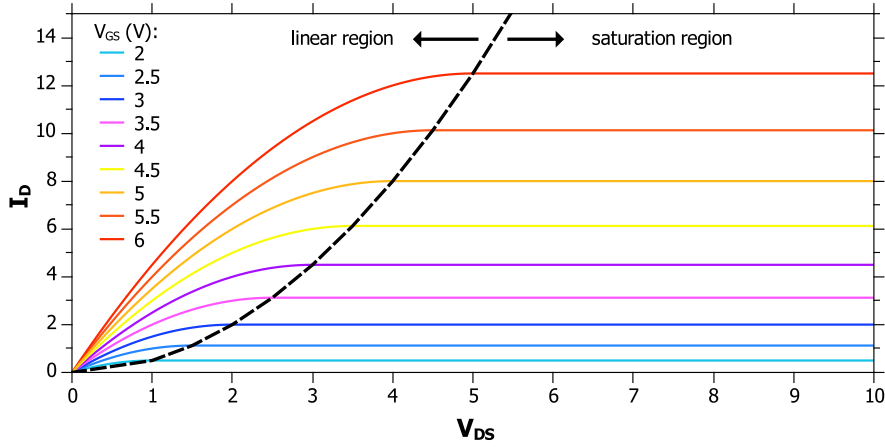


Figure 7.3: Current-voltage characteristics of a p-channel IGFET shown in figure 7.2 for several gate-source voltages. For convenience $\frac{\mu_p C_{oxide} W}{L}$ is set to 1 here.

7.1.2 Test Samples and Measurement Setup

Preliminary Remarks

Although the structure of a silicon strip sensor is very similar compared to that of a p-channel IGFET (see figure 7.1) some parts are different or even missing. At first it is obvious that the strips of a sensor are connected via the polysilicon resistors and the bias line to each other. Hence, drain and source have an ohmic connection in case of strip sensors. Furthermore the counterpart of the IGFET's gate dielectric differs. The insulating material in between of two strips and on top of the bulk material consists of one layer of SiO_2 and an additional layer of passivation. The chemical composition of the passivation layer can vary due to the deposition process (in detail described in [9]) but in general it is very similar to silicon nitride. Therefore, the passivation layer will be denoted with Si_xN_y . This additional layer should not influence measurements since it is also high resistive like SiO_2 . The third difference to a p-channel IGFET is the obvious absence of a gate electrode. The electrode has to be applied directly on the passivation layer to perform FET-like measurements on silicon strip sensors. Furthermore, the sensors DC-pads are used to obtain a direct connection to the p^+ implanted strips which are serving as drain and source terminals (see section 3.2.6).

Test Samples

Overall 3 test samples were primed for the following investigations. Two STI sensors of Infineons second batch and for reasons of comparability an additional silicon strip sensor manufactured by another vendor which produces sensors for the CMS tracker. The structure of this additional sensor is very similar to that of a STI with the exception that it has a trapezoidal shape. The vendor is known for its high-quality sensors so no defective strips are expected. In contrast both of the STI sensors show a distinct area of defective strips.

Nevertheless, this should be negligible since the target of the investigations is to test if silicon strip sensors behave like a p-channel IGFET. The results presented below indeed legitimate this approach. All used sensors have a thickness of $300\ \mu\text{m}$. The two STI sensors are called S1 respectively S2 and the additional sensor of the second vendor S3 for reasons of simplicity.

	S1	S2	S3
Length (cm)	4.3	4.3	4.7
Width (cm)	0.749	0.749	1.01 - 1.11
No. of strips	64	64	64
Strip width (μm)	20	20	26 - 34
Pitch (μm)	80	80	126 - 142
Gate material	Titanium / Gold	Conductive adhesive	Conductive adhesive
Area covered by gate (mm^2)	12.57	12.57	12.57
Strips covered by gate	53	53	31

Table 7.1: Characteristics of test samples used for FET-like measurements.

Two different methods are used for the creation of the gate electrode. The first method uses a conductive adhesive which is directly applied on the passivation of sensors S2 and S3. The second method uses a sputter process for the creation of a titanium pad onto the passivation of sensor S1¹. This pad is covered with a layer of gold preventing the occurrence of titanium dioxide. Table 7.1 summarizes the most important characteristics of the test samples which are shown in figure 7.4.



Figure 7.4: Samples with applied gate pads used for FET-like measurements. Left: All samples, right: Enlarged view of the different gate pads.

¹The Institute of Solide-State Electronics of the Vienna University of Technology carried out this process.

Measurement Setup

All measurements have been performed at the PQC setup (see figure 5.3). The required measurement instruments comprise two Keithley 2410 SMU's (K2410), one Keithley 237 SMU (K237) and one Keithley 6514 electrometer (K6514). Therewith, three different circuits are constructed to test the behaviour of silicon strip sensors under an applied gate potential. It is important to mention that all tests are performed at the standard full depletion voltage for sensors of Infineon (i.e. 300 V). Thus, the initial situation is comparable to single strip measurements performed at the QTC where the defective strips were observed for the first time.

- **First circuit (C1):** The K237 SMU is connected to the DC-pads of two neighbouring strips serving as a voltage source between drain and source. One of the two K2410 SMU's is used for the application of the gate voltage (called gate SMU). The high terminal is connected to the gate and the low terminal to the corresponding terminal of the first SMU. The second K2410 serves as biasing SMU. The low terminal is connected to the bias line and the high terminal to the backplane (BP). This circuit is used to test if the current flow between two strips can be influenced by an applied gate voltage.
- **Second circuit (C2):** The second circuit is very similar to the first one. The only difference is the placement of the ground connection. For the first circuit the ground potential is applied at one of the strips and connected to the low terminal of the gate SMU. Thus, potential at the bias line is floating for C1. This is contrary to the usually used bias configuration where the bias line is set to ground. For the second circuit the "normal" bias configuration is restored and the potentials applied at the strips and the gate are now the floating ones. Likewise as circuit C1, this circuit is used to test the behaviour of the current flow between two strips when a gate voltage is applied.
- **Third circuit (C3):** The third circuit uses the K6514 electrometer for investigations of the gate voltage dependence of the single strip leakage current. The high terminal of the electrometer is connected to one of the strips and the low terminal to ground. The bias configuration and the connections to the gate SMU are the same as for the second circuit. Furthermore, the low terminals for every measurement instrument are shorted with ground for C3. Hence, no floating potentials exists for this circuit.

All described circuits are shown in figure 7.5. Circuits C1 and C2 are very similar to the one shown in figure 7.2 with the exception that the polarities are changed. The threshold voltage V_T is now negative and negative gate potentials will cause the emergence of an inversion layer. Nevertheless, the described theory in section 7.1.1 is still valid if one considers the change of the polarities.

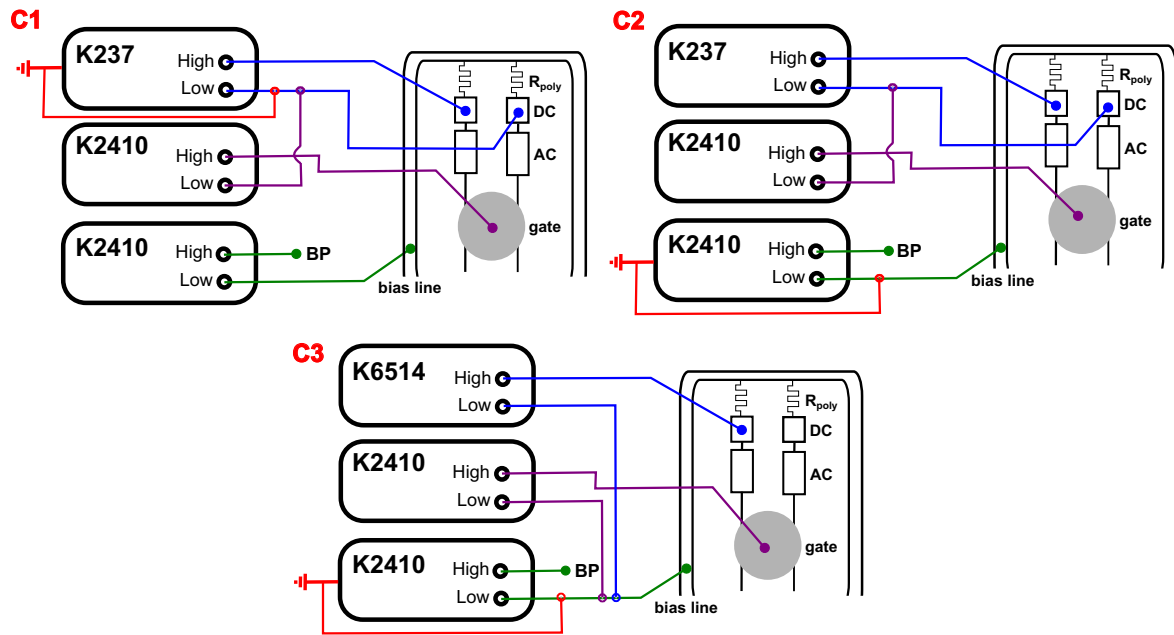


Figure 7.5: Circuits C1 (upper left), C2 (upper right) and C3 (bottom middle). The measurement instruments, a simplified strip sensor and the wiring are shown for each circuit.

7.1.3 Measurement Results

Different types of investigations are performed by using the above described circuits. First of all two different types of measurements are carried out using circuits C1 and C2. The first measurements concern the current-voltage characteristics between two neighboring strips at one fixed gate potential. Afterwards measurements of the same characteristics but with a constant voltage between two neighboring strips and a varying gate potential are conducted. Circuit C3 is used to record the single strip leakage current for varying potentials applied at the gate electrode. Measurement results gained from C3 are of particular interest since they can be compared to previous measurements of the single strip current observed at the defective area. However, target of all investigations of this section is to validate if the strips of silicon strip sensors can be conductively interconnected by the use of a gate voltage.

Current-Voltage Characteristics for Constant Gate Voltages

Due to the described functionality of a p-channel IGFET (see subsection 7.1.1) and the constructed circuits it is expected that negative gate voltages cause the appearance of an inversion layer leading to a conductive interconnection of two neighboring connected strips. Positive gate voltages on the contrary should result in an unchanged or even better strip isolation. However, all strips are connected over the R_{poly} so a current will flow anyway even if a good strips isolation at the implant layer is granted. Hence, the equivalent circuit is a parallel cir-

cuit of the inter strip resistance and the resistance of in series connected polysilicon resistors. Nevertheless, a change of the inter strip resistance will change the resistance of the whole parallel circuit.

The following measurement results display the current-voltage characteristics of a particular pair of neighboring strips for all test samples (S1, S2 and S3) and for the two circuits (C1 and C2). The connected strips are the same for every test sample for reasons of comparability.

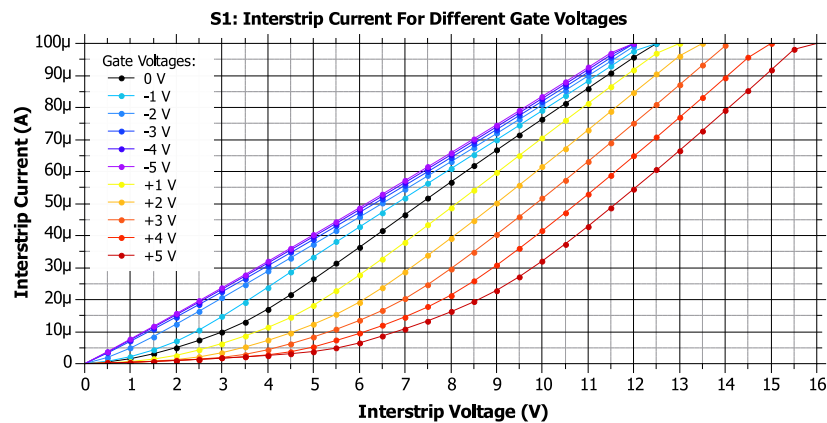


Figure 7.6: IV characteristics of two neighboring strips for sample S1 and circuit C1.

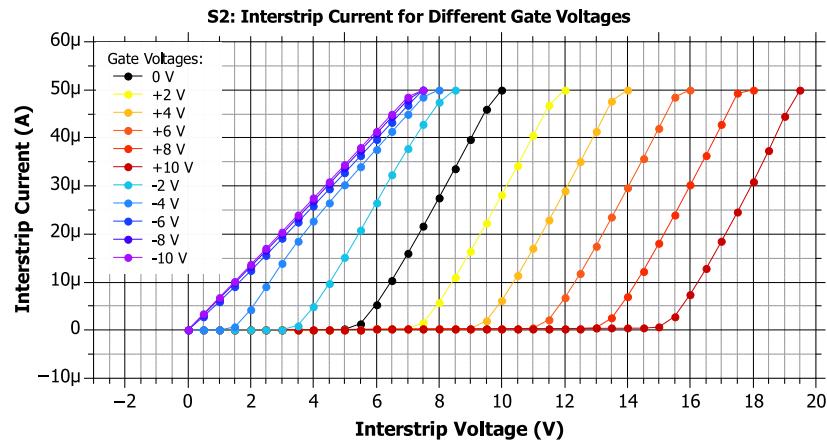


Figure 7.7: IV characteristics of two neighboring strips for sample S2 and circuit C1.

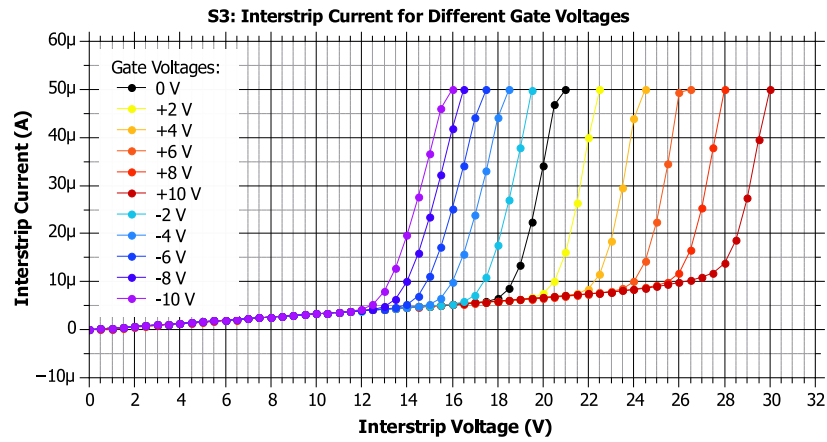


Figure 7.8: IV characteristics of two neighboring strips for sample S3 and circuit C1.

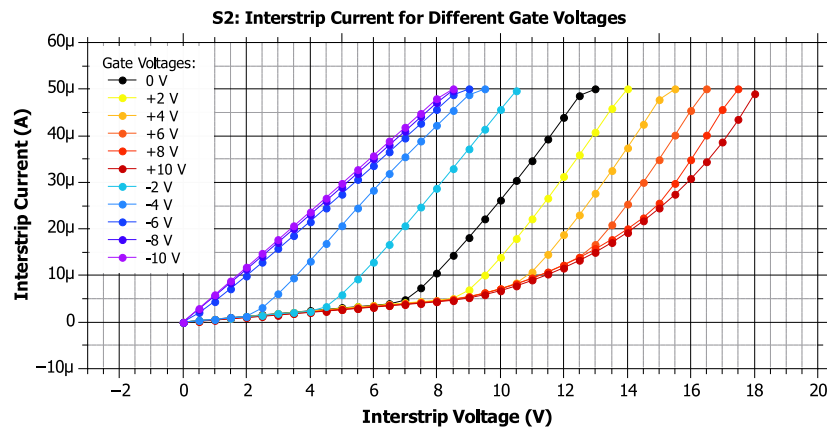


Figure 7.9: IV characteristics of two neighboring strips for sample S2 and circuit C2.

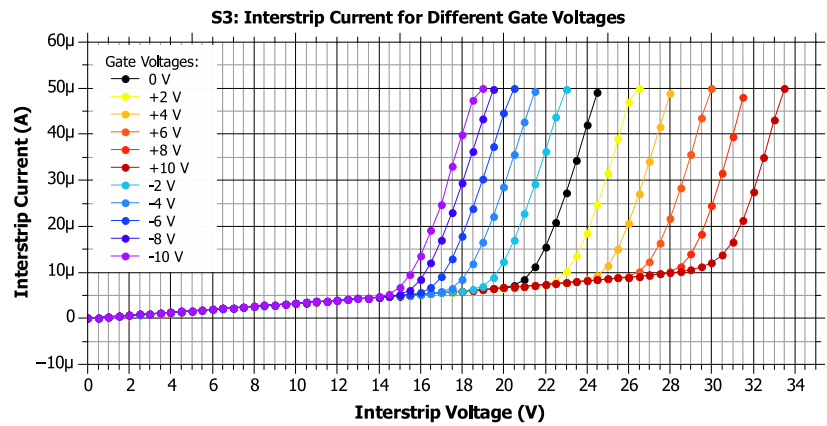


Figure 7.10: IV characteristics of two neighboring strips for sample S3 and circuit C2.

Figures 7.6 to 7.10 show that the current-voltage characteristics of silicon strip sensors can be influenced by an externally applied gate potential. It can be observed that negative gate voltages lead to higher currents and positive ones in lower currents if a defined interstrip voltage is applied. This corresponds more or less to the expected reaction. Nevertheless, the shapes of the curves are not comparable to the curves of a p-channel IGFET shown in figure 7.3. In particular no saturation of the inter strip current is visible which actually should be somehow visible although the current is flowing through the bias resistors. Alongside, positive gate voltages cause a shift of the curves to higher inter strip voltages (comparable to higher resistances) which cannot be explained by the theory of IGFET's. This theory implies that no currents will flow as long as $V_{GS} > V_T^2$. The threshold voltage V_T is negative for the used circuits so in particular all gate voltages higher or equal zero should evoke the same curves. It is imaginable that positive gate voltages could lead to an improvement of the strip isolation if defective strips are connected by a previously existent inversion layer. However, this would only hold for sensors S1 and S2 but not for sensor S3 where it is assumed that it has no defective strips. Most likely the shapes of the curves and the effect of positive gate voltages are influenced by the bias configuration and the used circuitry which differs from the one shown in figure 7.3. As already mentioned all measurements were conducted at full depletion voltage which is contrary to the "normal" operation of a IGFET. Beside this the sensor design and the existence of the parallel resistance circuit could influence the measured characteristics. However, applied gate potentials change the behaviour of the current flow which indicates that silicon strip sensors are at least comparable to p-channel IGFET's.

Coming back to the measurement results it can be observed that the measured characteristics are nearly equal for circuits C1 and C2. Hence, all further measurements are performed by using circuit C2 only since the bias configuration is the same as the one used for strip scans. It also can be observed that sample S1 shows a slightly different behaviour as the other test samples. Measurements of the global characteristics revealed that it could be damaged during the sputter process used for the application of the gate electrode. Sample S1 is excluded from further investigations for this reason.

Current-Voltage Characteristics for Varying Gate Voltages

The previous measurement results shows that the curves tend to move to lower inter strip voltages for decreasing gate voltages which states that the interstrip resistance gets accordingly smaller. This happens the other way around for positive gate voltages. However, the gap between two curves seems to stay constant for increasing positive gate voltages and continuously getting narrower for negative gate voltages. Investigations concerning this issue are presented in the following. These investigations only regard negative gate potentials since it is assumed that only they can generate the inversion layer. The inter strip voltage is set to a value where the change of the current caused by a change of the gate potential will be clearly visible. In particular, it is set to 5 V for sample S2 and to 20 V for sample S3. Subsequently

²This inequality differs from the one used in section 7.1.1 ($V_{GS} < V_T$) due to a change of the polarities.

the inter strip current for a continuously decreasing gate voltage is recorded.

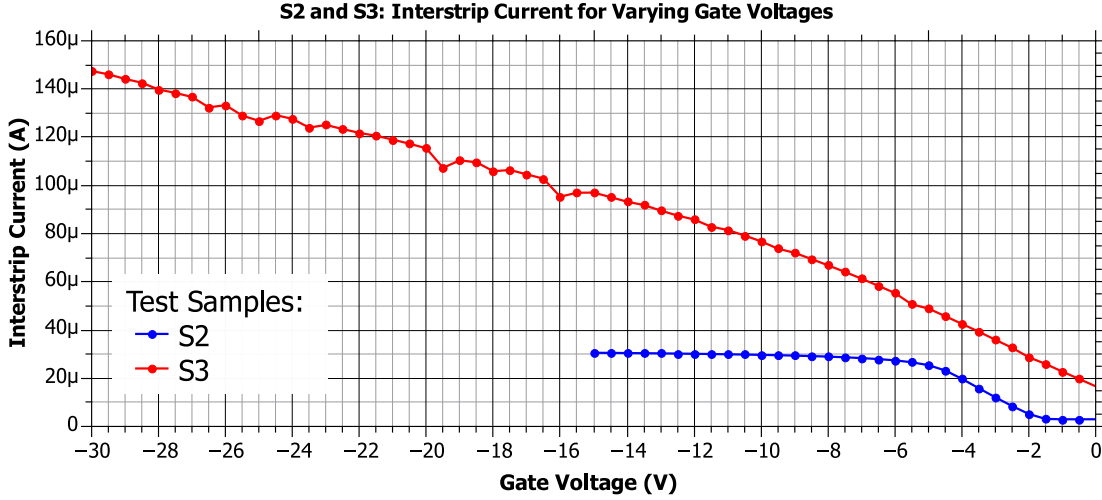


Figure 7.11: IV characteristics of two neighboring strips for samples S2 and S3 for varying gate voltages (measured using circuit C2).

Figure 7.11 shows that decreasing gate voltages effect higher inter strip currents although the inter strip voltage remains constant which can be compared to decreasing interstrip resistances. This behaviour can be observed for both test samples. In particular sample S2 shows more reasonable results. It displays an increase of the current which eventually saturates at about $V_{GS} \approx -6V$. The saturation could refer to the lowest possible inter strip resistance (at the implant layer). The theory of IGFET's described in section 7.1.1 tells that saturation occurs if $V_{DS} = |V_{GS}| - |V_T|$ according to the boundary conditions³ of equation 7.3. It also can be observed that the current starts to increase at about $-2V$. This voltage could refer to the threshold voltage V_T . Inserting these voltages into the above mentioned equation gives:

$$\underbrace{6V}_{|V_{GS}|} - \underbrace{2V}_{|V_T|} = \underbrace{4V}_{V_{DS}}. \quad (7.4)$$

The derived 4V of the drain-source voltage comes pretty close to the adjusted drain-source voltage of this sample (i.e. 5V). Hence, also this measurement indicates that silicon strip sensors behave like p-channel IGFET's. The indications are even stronger than those for the previously shown measurements since the theory of IGFET's itself can be brought into relation to silicon strip sensors.

³The absolute values of V_{GS} and V_T are added again due to the changed polarity compared to figure 7.3.

Sample S3 in contrast shows no saturation and no threshold voltage. The current is just continuously increasing. The absence of a visible threshold voltage could be due to the fact that its absolute value is very small. Actually this is not expected due to the large pitch which should lead to a high threshold voltage. The most probable explanation of the missing saturation region is the selected limit of the gate voltage. A further decrease of this voltage will most likely result in a current saturation. This was not carried out because the high inter strip current could damage the sensor (the inter strip current is already $150 \mu\text{A}$ at a gate voltage of -30 V).

Single Strip Leakage Current for Varying Gate Voltages

The following investigation concerns the dependance of the single strip leakage current for continuously decreased gate potentials. Circuit C3 is used to measure the current of a single strip on sensors S2 and S3. The number of the selected strip is the same for each sample. Negative gate voltages are of special interest since only negative ones will most probably cause the emergence of an inversion layer.

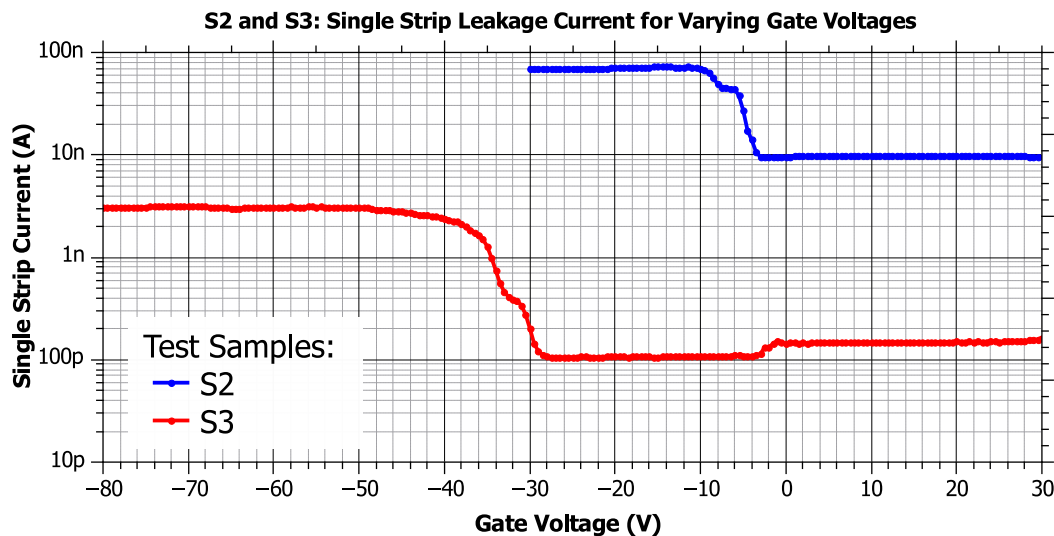


Figure 7.12: Single strip leakage current of samples S2 and S3 for continuously decreasing gate voltages (logarithmic scale, measured with circuit C3).

Figure 7.12 displays the measurement results for sensors S2 and S3. The single strip current of both sensors remains nearly constant up to a particular negative gate voltage (i.e. -3 V for sample S2 and -29 V for sample S3). A further decrease of the gate voltage results in a radical increase of the single strip current. Finally both currents saturate at a second well defined gate voltage (i.e. -10 V for sample S2 and -40 V to -50 V for sample S3). This behaviour is comparable to previous measurement results shown in figure 7.11. The assumption is that decreasing gate voltages cause a decrease of the inter strip resistance which causes the increase

of the single strip current. Therefore, the measured current of a single strip is roughly the sum of the single strip currents of strips interconnected by the inversion layer. The voltage where the current starts to increase can be compared to the threshold voltage V_T of a p-channel IGFET. It is about -3 V for sensor S2 and about -29 V for sensor S3. The high threshold voltage for sample S3 is very unexpected due to the already gained results. The voltage where the current starts to saturate probably corresponds to the point where the minimum of the inter strip resistance is reached. This is contrary to the saturation behaviour of “normal” p-channel IGFET’s where saturation starts at $V_{DS} = |V_{GS}| - |V_T|$. Hence, it depends on the inter strip voltage which is not existent for this type of measurements. Therefore, the saturation of the single strip current can only be explained by the lowest possible inter strip resistance independent of a drain-source voltage V_{DS} . The voltage where the resistance reaches its minimum (or where the current is maximum) would be about -10 V for sensor S2 and -40 V to -50 V for sensor S3.

Gate voltages referring to the increase and saturation of the single strip current are different for sensors S2 and S3. In particular sensor S3 requires lower gate voltages than sensor S2. Two major reasons could be responsible therefor. At first, the pitch differs which is for sample S3 about 65% larger than the pitch of sample S2. This should clearly influence the formation of an inversion layer since it is reasonable that larger pitches correspond to higher absolute values of threshold voltages. In addition the resistivity of the bulk material differs. Unfortunately actual values are unknown but already small deviations will definitively have an impact on the formation of the inversion layer.

The performed measurements also offer deeper insights into the manner of the conductive interconnection observed at measurements of the single strip parameters. In the first instance it can be assumed that strips are shorted (i.e. inter strip resistance is very close to zero). Accordingly the sum of the single strip currents of interconnected strips is measured instead of the “real” single strip current. The second assumption is that the shorted strips are those which are covered by the gate pad. A sufficiently small voltage at the pad consequently causes the short circuit (i.e. when saturation occurs). Based on those assumptions the saturation current can be calculated by multiplying the single strip current for positive gate voltages by the number of covered strips. The calculated value should be in the order of 70 nA for sample S2 and 3 nA for sample S3 (saturation currents shown in figure 7.12) if all covered strips are shorted. The actual calculation yields:

$$\begin{aligned} \text{Sample S2} &: 9.7\text{ nA} \times 53 = 514\text{ nA} > 70\text{ nA} \\ \text{Sample S3} &: 150\text{ pA} \times 31 = 4.65\text{ nA} > 3\text{ nA} \end{aligned} \tag{7.5}$$

Equation 7.5 shows that the calculated value of the saturation current of both samples is higher than the measured one. Hence, the simple model of a low ohmic connection between strips is questionable and not very likely. Indeed it could be possible that the inter strip resistance is not negligible even for very low gate voltages which would result in lower saturation currents. It is also questionable if all by the gate pad covered strips are interconnected. A lower number of interconnected strips would also result in a lower current.

7.1.4 Conclusion

All types of performed measurements clearly indicate that silicon strip sensors can be compared to p-channel IGFET's. Results gained from circuits C1 and C2 show that the resistance of two neighboring strips at the implant layer can be adjusted by the use of a gate potential. Measurements of the single strip current performed with circuit C3 revealed that also this current depends on an applied gate potential. Therewith, a correlation to single strip measurements performed at the QTC is achieved. Moreover, the error pattern of the area of defective strips concerning measurements of the single strip current can be reproduced (i.e. higher single strip currents for negative gate voltages). However, differences to p-channel IGFET's are also present. Design differences and the used circuits are the most probable reasons for the observed discrepancies.

Now it is of special interest how a conductive interconnection of strips can be achieved without the use of a gate pad. This question is especially relevant because silicon strip sensors definitively show an area of defective strips most likely caused by a conductive interconnection of strips although no gate pad exists. The theory of IGFET's discussed in section 7.1.1 tells that it is not necessary that an external voltage source (i.e. instrument) is connected to the gate pad for the maintenance of an inversion layer. Instead the negative charges at the gate pad and the resulting coulomb force are responsible therefore. Hence, a final test using circuit C1 and sample S1 is performed to investigate if the accumulated charges at the pad are sufficient to maintain the inversion layer. The measurement procedure is the same as for measurements shown in figure 7.6 with the exception that the current between two strips is also measured when the probe needle is lifted away from the gate pad. The potential at the pad should then be maintained by the previously deposited negative charges.

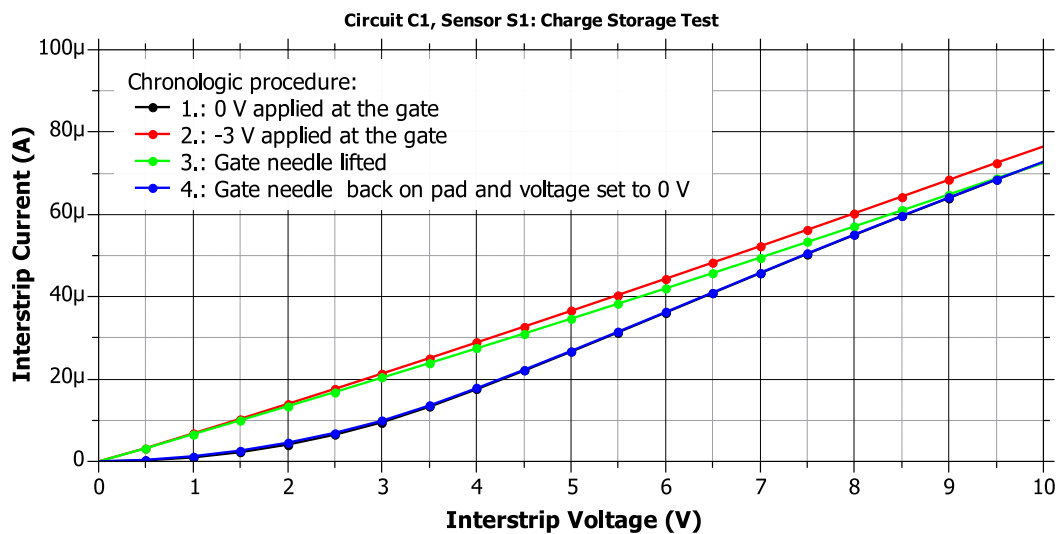


Figure 7.13: Test if stored charges at the gate pad are sufficient to maintain an inversion layer (the black curve is beneath the blue one).

The chronological measurement procedure is as follows: 0 V applied at the gate pad → -3 V applied at the gate pad → needle lifted → needle placed back on the pad and voltage is set to 0 V. For every step the IV characteristics of one pair of neighboring strips is recorded. The green and the red curve shown in figure 7.13 are nearly coinciding. This confirms the previously made assumption that negative charges are sufficient to maintain the inversion layer. In addition it can be assumed that charges on top of the passivation layer would lead to the same effects like those stored at the gate pad. Hence, a gate pad would not be necessary. So in general it very plausible that surface charges at the passivation layer can influence the behavior of silicon strip sensors in a way that strips are conductively interconnected which finally results in the observed area of defective strips. All of the following investigations are therefore based on this hypothesis.

7.2 External Charge Application Using an Ioniser Pistol

This section examines if externally applied charges at the surface of a sensor are sufficient to cause the emergence of an area of defective strips or at least have an impact on single strip parameters. Results gained from the previous section 7.1 indicate that negative surface charges provoke the formation of an inversion layer between strips which results in a defective area. Therefore, negative charges are applied in order to reproduce or expand the observed error pattern. Beside negative charges also positive charges are applied to investigate if the defective area can be cured by charges of a different polarity. In addition global sensor parameters are measured to investigate if also they can be affected by surface charges.

7.2.1 Measurement Setup and Tests Samples

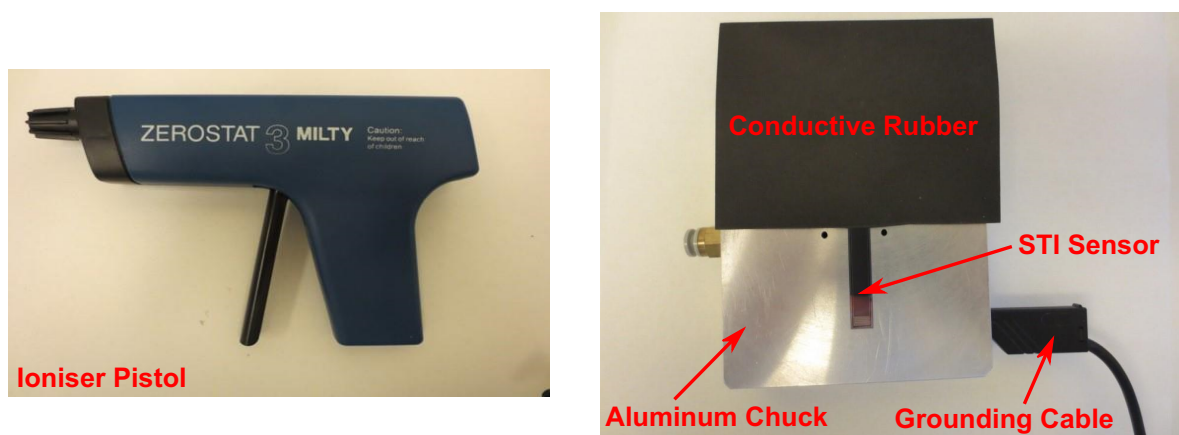


Figure 7.14: Left: Ioniser pistol, right: Preparation of a sensor.

An ioniser pistol (see figure 7.14 left) is used for the application of the electrical charges. Therewith, negative and positive charges of about 1.5 C can be applied by pulling the trigger of the device. The spread is about 40 cm if the distance to the object is about 30 cm.

The amount of charge and the application itself is not very precise but sufficient for the described purpose.

Test samples are two STI sensors of batch 2 which show a distinct area of defective strips. Hence, the evocation of a defective area by negative surface charges can not be investigated since such an area is already present. Nevertheless, it can be investigated if negative charges broaden the zone of defective strips and positive ones cure the whole sensor.

The samples are mounted onto an aluminium chuck and about the half of the sensors surface is covered with a conductive rubber that touches the sensor and the chuck (see figure 7.14 right). Hence, only a defined area of the sensor is directly exposed to the stream of charges. A grounding of the chuck ensures the drainage of excessive charges that hit the rubber and the chuck. Charges that hit the bare part of the sensors surface are preserved since the passivation is a high resistive material which should prevent the fast drainage of charges.

7.2.2 Measurement Results

In total three measurements of the single strip parameters I_{strip} , R_{poly} , C_{ac} and I_{diel} and global sensor parameters (CV and IV characteristics) are performed to investigate the impact of externally applied charges. The parameter I_{strip} is the only one presented in the following due to its high significance and due the fact that all other single strip parameters behave similar (i.e. showing the same defective area). The first measurement is realized before any charges are applied. Data from this measurement represent the initial situation. Afterwards charges are applied for one time by pulling the trigger of the ioniser pistol once. Subsequently the sensor is placed into the QTC and remeasured. The last measurement is carried out after charges are applied for ten times. The whole procedure is realised for two different STI sensors where either only negative or only positive charges are applied. The ioniser pistol is placed about 3 cm above the sensors surface for every of the two test runs. This distance is small enough so that most of the charges hit the sensor.

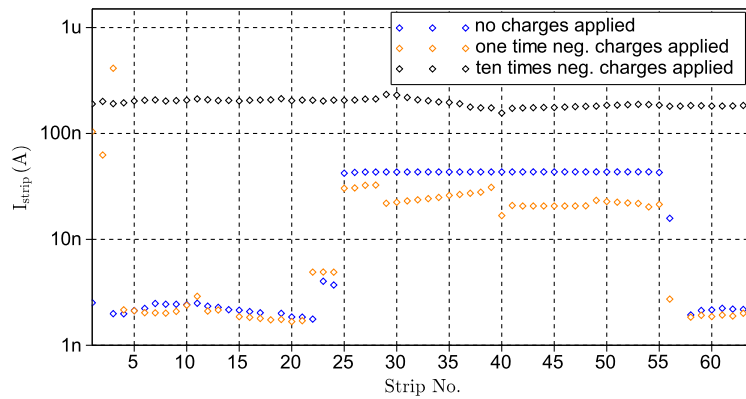


Figure 7.15: I_{strip} of sensor used for negative charge application (logarithmic scale).

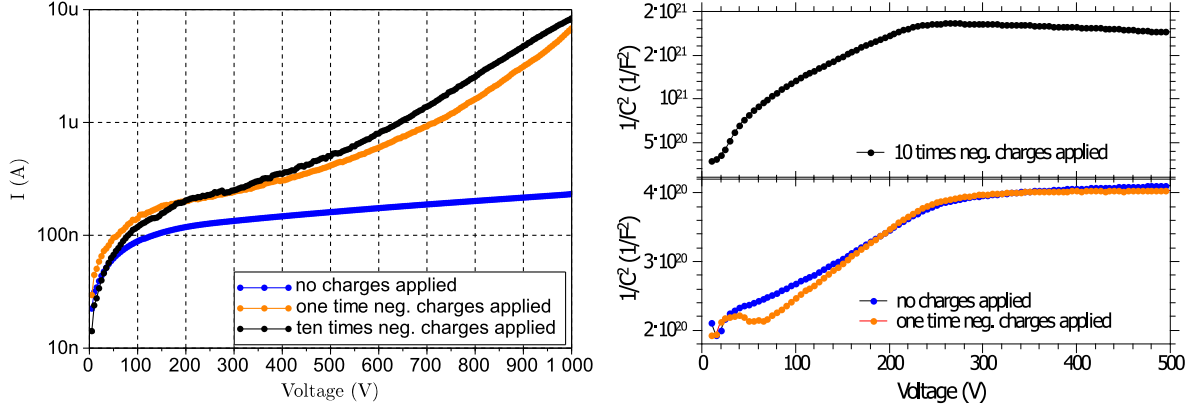


Figure 7.16: Global parameters of sensor used for negative charge application. Left: IV (logarithmic scale), right: CV (linear scale).

The measurement results of I_{strip} of the sample used for the negative charge application (figure 7.15) show that a sufficient amount of negative charge clearly affects its single sensor parameters. All other strip parameters show comparable results like I_{strip} . If negative charges are applied for one time the defective area remains nearly the same as for the initial situation. This is remarkable since roughly 1.5 C are applied which represents already a huge amount of charge. On the contrary the global IV characteristics (figure 7.16 left) have already changed. A breakthrough arises which is not present for the initial situation. The CV characteristics on the other hand (figure 7.16 right) are not affected for a single application of negative charges. The situation changes dramatically if charges are applied for ten times. Strip and global parameters are now heavily affected. All strips show a higher current which leads to the assumption that now all strips are conductively interconnected. Thus, the area of defective strips broadens over the whole sensor. The IV characteristics are unchanged compared to the previous measurement but the CV characteristics are very strange and not comparable anymore to the previous measured ones. It could be possible that the sensor is already damaged due to the extremely high amount of applied charges.

It turns out that positive charges affect the sensor in a similar way as negative ones. As before the single strip current of the sample used for positive charge application (figure 7.17) is not affected if charges are applied for one time only. It is assumed that they cure the defective area but nothing like that can be observed. Furthermore, the application of ten times the amount of positive charges reproduces the error pattern observed for negative charges. This is very contrary to the assumption. The global measurement results (see figure 7.18) are less affected compared to the previous case of negative charge application. The IV characteristics show good results (i.e. low currents and no breakthroughs) but one comparatively early breakthrough is visible after positive charges are applied for ten times. The CV characteristics on the contrary remain unchanged for every amount of added charge.

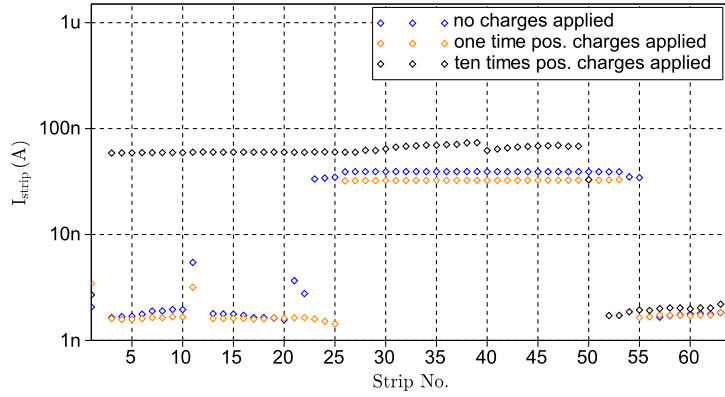


Figure 7.17: I_{strip} of sample used for positive charge application (logarithmic scale).

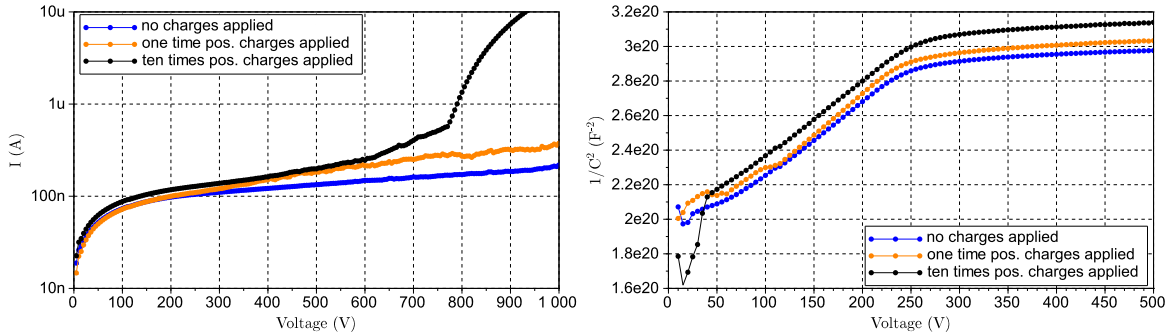


Figure 7.18: Global parameters of sensor used for positive charge application. Left: IV (logarithmic scale), right: CV (linear scale).

The performed investigations confirm that external charge application affects the single strip and global sensor parameters of silicon strip sensors. It has been found that also positive charges can lead to the same increased currents and so far it is not understood what mechanism is responsible therefore. Nearly the same error pattern can be observed as for the other case which cannot be explained by the theory of IGFET's.

Results of global characteristics of both test runs indicate that both sensors are already heavily damaged by the excessive application of charges which is not surprising since several coulombs were applied. Generally charges and electrostatic discharges can be very harmful for silicon devices and are comprised in the topic of ESD (electrostatic discharge) which is well known in semiconductor industries. However, it is still assumed that negative surface charges are the reason for the conductive interconnection and thus for the area of defective strips since it is not clear if the sensors were already damaged or not.

7.3 Formation of the Defective Area at Infineon and HEPHY

This section investigates treatments of sensors manufactured by Infineon that could cause the defective area. A priori those treatments can be associated with an external application of charges. The previous sections explained how charges can affect the sensor parameters in a way that a defective area becomes visible. The treatments described in the following might also directly affect the sensor parameters but it is most likely that the produced charges are responsible therefor.

7.3.1 Sawing Tests

To obtain a single sensor out of a fully processed wafer one has to cut it out by the use of a diamond sawing blade. The sawing process is the last step of sensor manufacturing and very likely generates electrostatic charges which can settle onto the surface of a sensor. That the sawing procedure at Infineon could be the reason for the defective area becomes apparent if one compares the results of single strip measurement obtained by Infineon and HEPHY [13]. Infineon established an automated test equipment ATE (figure 7.19) which measures the same sensor parameters which HEPHY does except for inter strip parameters. The ATE setup can only perform measurements on STL sensors which are on an uncut wafer. Hence, the sensor and the whole wafer are not sawed at the time of measurement. One wafer which was already tested by Infineon was delivered to HEPHY without an applied sawing procedure to obtain comparable measurement results of the thereon located STL sensor [13]. The right picture of figure 7.19 shows the measurement results of R_{poly} of this STL sensor obtained by Infineon and HEPHY. At first it can be observed that both measurement results are very similar. This is especially important for a later mass production since one can rely on results gained by Infineon. However, it is more astonishing that no defective area can be observed neither at HEPHY nor at Infineon. The only difference to sensors showing a defective area is that this sensor is not sawed. Thus, it is very convincing that sawing might induce the defective area.

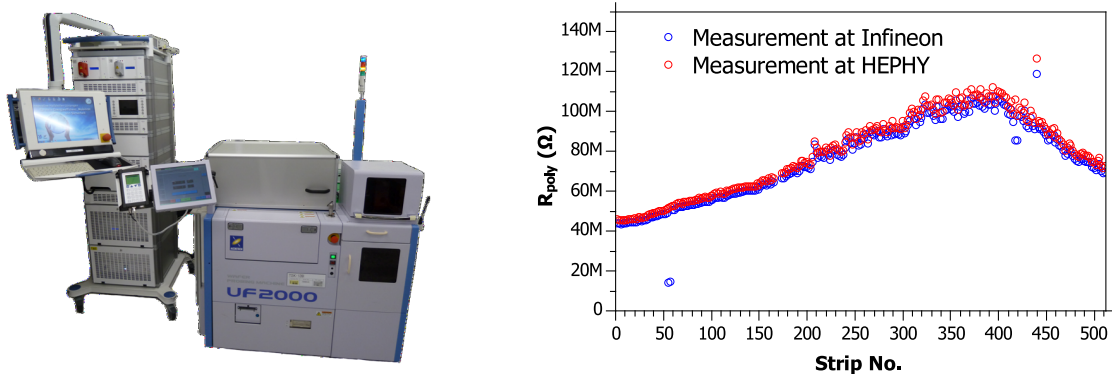
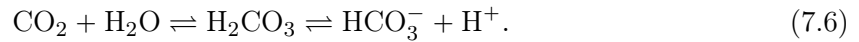


Figure 7.19: Left: ATE setup at Infineon, right: Measurement results of R_{poly} obtained by HEPHY (red) and Infineon (blue) of a STL sensor which is not sawed.

It is necessary to have a sawing method that prevents the arising of an area of defective strips since sensors have to be cut out of the wafer anyway. Two papers (i.e. [14] and [15]) discuss the generation of electrostatic charges during the sawing process and a possible improvement of this procedure. According to these references the high resistive deionised water serving as a sawing lubricant in combination with the rotating sawing blade might be responsible for the generation of static charges and electrostatic discharges. Results gained from the previous sections lead to the assumption that those static charges are retrained at the surface of sensors and most likely cause the defective area. A commonly used method in semiconductor industries called CO₂ bubbling might be able to prevent the emergence or to provide a better dissipation of harmful static charges [14], [15]. By this method CO₂ is added to the sawing lubricant (i.e. carbonising it) in order to lower its resistivity. If carbon dioxide is added to water carbonic acid is produced which dissociate in hydrogen and bicarbonate ions [16]:



Those ions subsequently lower the resistivity of the sawing lubricant which provides a better dissipation of static charges generated during the sawing procedure. However, this method is controversial since carbonic acid can also damage certain semiconductor devices. Especially the metallisation of devices is endangered.

Infineon delivered two differently sawed wafers to investigate the impact of CO₂ bubbling. One wafer is sawed with enabled CO₂ bubbler and the other one with the standard process (i.e. without CO₂ bubbler). Furthermore, Infineon provided the measurement results gained by the ATE setup of the STL sensors of both wafers. This provides an opportunity of validation that sawing is able to induce the area of defective strips. A direct comparison of measurement results gained by Infineon and HEPHY is hindered by the fact that Infineon measures all single strip parameters at 50 V but HEPHY at 300 V bias voltage. The most comparable parameter for this situation is R_{poly} since it is nearly independent of the bias voltage. Therefore, a focus on this parameter is set in the following.

Figure 7.20 shows the measurement results obtained by Infineon and HEPHY of a STL sensor sawed with the standard procedure without CO₂ bubbler. No defective area can be observed for measurements done by Infineon. This is expected because similar results were observed earlier for sensors which are not sawed (see figure 7.19 right). The already sawed sensor measured at HEPHY in contrast shows a broad defective area between strip number 20 and 420 and in addition a narrower one between strip number 480 and 510. These are the same affected strips which were observed at measurements of sensors of batch 2. This strongly indicates that the standard sawing procedure causes the area of defective strips and that not previous processing steps at Infineon are responsible therefor. The emergence of the defective area can be evoked by other issues happening between sawing at Infineon and measurements at HEPHY. Such issues are packaging, transportation or handling of sensors.

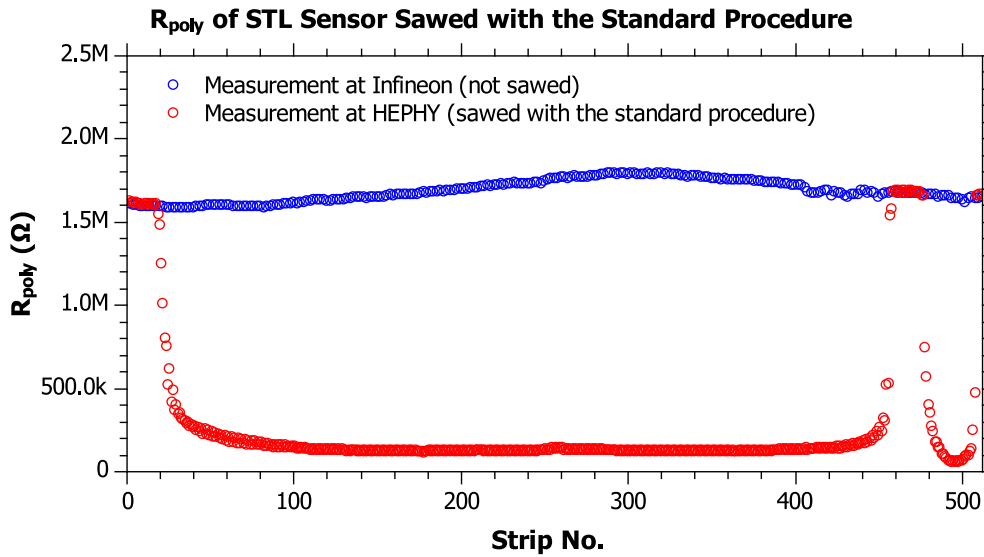


Figure 7.20: R_{poly} of a STL sensor sawed with the standard procedure (i.e. without CO_2 bubbler). Infineon (blue) measured the sensor directly on the wafer at 50 V bias voltage. The measurement at HEPHY (red) was performed on the already sawed sensor at 300 V bias voltage.

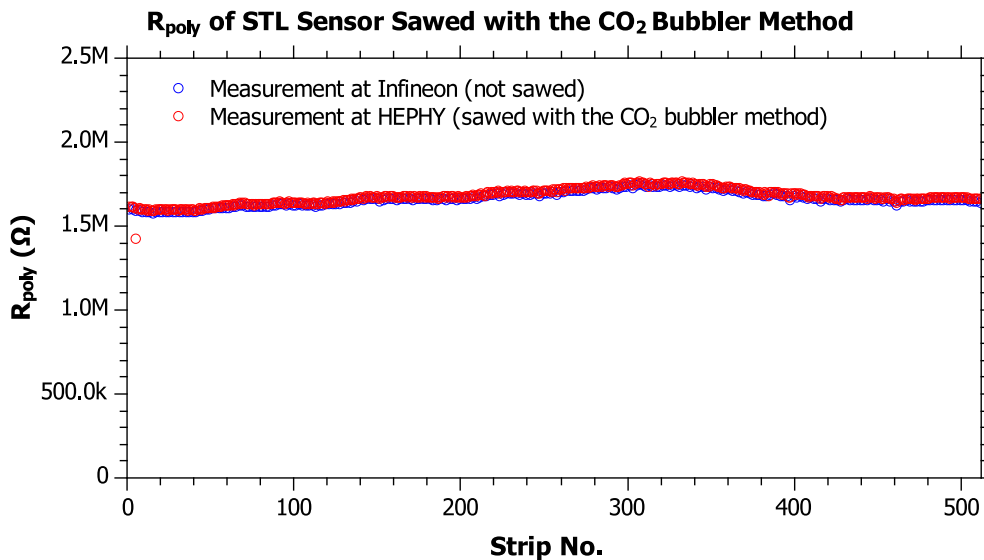


Figure 7.21: R_{poly} of a STL sensor sawed with the method of CO_2 bubbling. Infineon (blue) measured the sensor directly on the wafer at 50 V bias voltage. The measurement at HEPHY (red) was performed on the already sawed sensor at 300 V bias voltage.

Figure 7.21 displays the measurement results of Infineon and HEPHY of the STL sensor sawed with the method of CO₂ bubbling. Both results coincide and in addition a defective area is not present. This is remarkable since the measurement at HEPHY was performed on the already sawed sensor. Measurement results gained from this sensor strongly indicate that the method of CO₂ bubbling prevents the emergence of an area of defective strips.

All other sensors of the two differently sawed wafers show similar results as the STL sensor. The gained additional statistics encourage these conclusions. Unfortunately, some sensors which were sawed using the CO₂ bubbler method still show a small defective area (see figure 7.22). This area is explicitly narrower than the normally observed one but the error pattern is the same (i.e. higher single strip current, lower poly silicon resistances, etc.). The method of CO₂ bubbling can therefore only be seen as an improvement but not as a solution of the problem. Again it is possible that other processes induced the defective area. Especially sensor handling could be responsible which will be investigated in more detail later. However, defective strips at the far right (high strip numbers) of the sensor are not visible for any sensor sawed with the method of CO₂ bubbling. It is imaginable that the deviating values of these strips can only be generated by the standard sawing procedure itself.

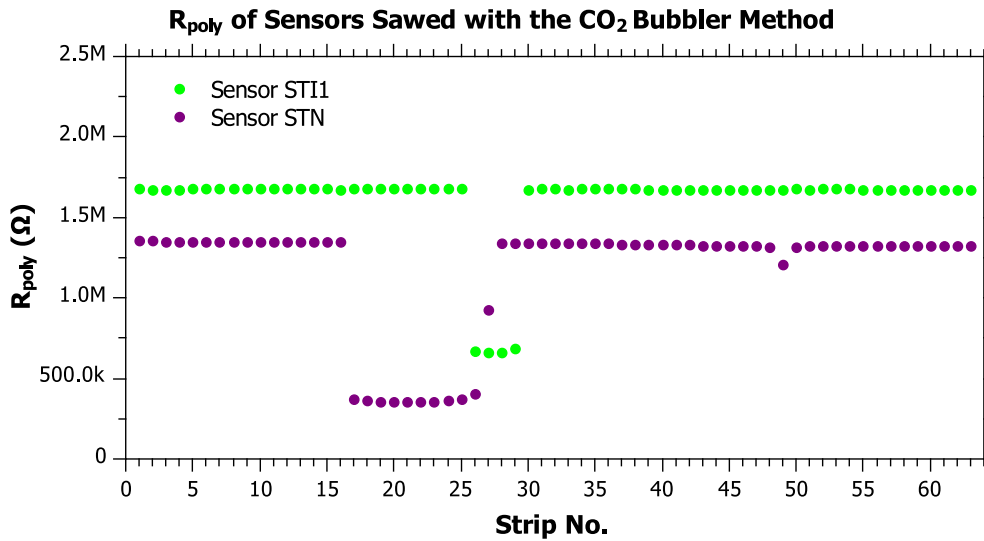


Figure 7.22: R_{poly} of sensors STI1 and STN sawed with the method of CO₂ bubbling.

The STL sensor sawed with the method of CO₂ bubbling (figure 7.21) was remeasured in order to investigate if a defective area reappears after a certain time. This provides information if only the sawing procedure is responsible for the emergence of the defective area or if other issues might also contribute.

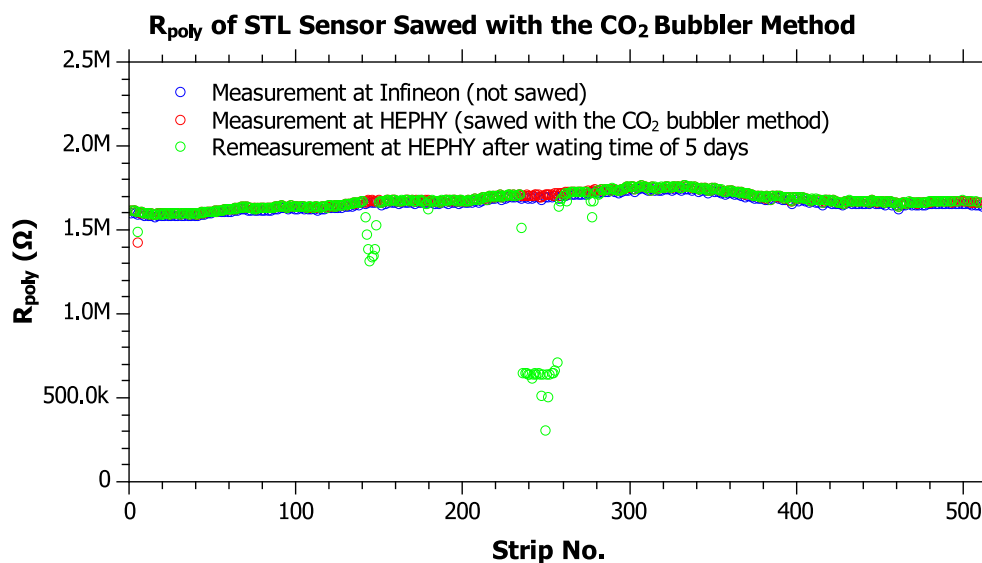


Figure 7.23: Measurement results shown in figure 7.21 (blue, red) and in addition the results of the remeasurement at HEPHY (green).

Figure 7.23 displays the measurement results of R_{poly} shown in figure 7.21 and in addition the results of the remeasurement. The remeasurement was performed after a waiting time of 5 days where the sensor was not handled and stored in a dry box. It can be observed that the sensor shows a very narrow defective area which appeared during the 5 days of waiting time. Thus, an additional issue besides the standard sawing procedure is able to generate a defective area. That the storage is responsible for the reoccurrence of defective strips is not very likely since all sensors are stored at defined and monitored atmospheric conditions (i.e. constant temperature and constantly low humidity). It is more likely, however, that the handling of sensors is the cause of the reappearance of the defective area.

7.3.2 Sensor Handling Tests

All unpackaged devices in semiconductor industries are strictly handled under electrostatic discharge (ESD) safe conditions. This is important since electrostatic charges located at the handling instruments or at the body of the operator can easily be generated by mechanical friction, electrical fields or triboelectric effects. The potential difference to ground caused by those charges can reach voltages of up to several kV. An eventual discharge will result in high currents which might flow off to ground directly through the handled semiconductor device. In most cases the device is completely destroyed after such an electrostatic discharge. Therefore, ESD-safe conditions prevent the accumulation of static charges by a permanent ohmic connection to ground of everything which gets in touch with an ESD sensitive device. Consequently, discharges at the devices are not possible anymore because all static charges are permanently dissipated.

ESD safe conditions are only partly realised at the clean room of HEPHY. Especially the ESD safety of handling instruments is sometimes questionable. This makes it likely that static charges are generated during sensor handling which do not have the possibility to flow off to ground. Besides the risk of an electrostatic discharge those charges can settle onto the sensors surface and induce the defective area.

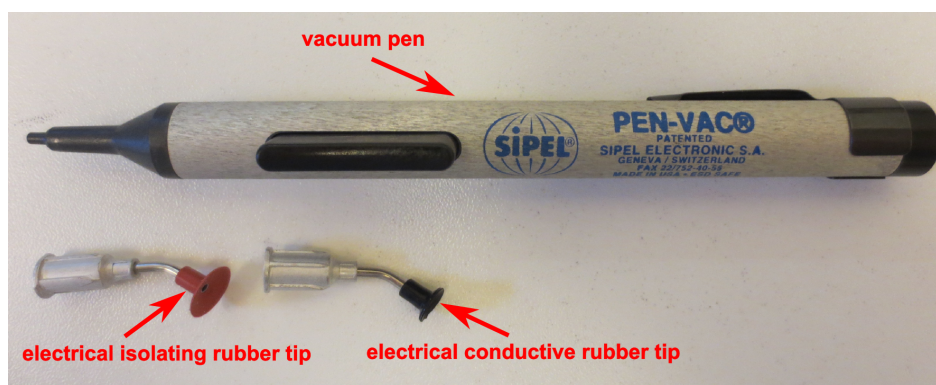


Figure 7.24: Vacuum pen with different rubber tips.

Sensor handling at HEPHY is mostly done by using vacuum pens (see figure 7.24). The rubber tip of the pen can be fixed to a sensor by the use of a vacuum which is generated by pressing a button at the pen. The pen itself is ESD safe but the rubber tips might not. In particular, the black tip is electrically conductive thus ESD safe but it turned out that the red tip is electrically isolating. Hence, static charges at the insulating red rubber tip cannot flow off even if an operator wears a wristband which is connected to ground. Generally the red tip provides better fixation of sensors which makes it the primarily one used for sensor handling. It is therefore indeed imaginable that if sensors are handled with the red tip, static charges are generated by friction or triboelectric effects which cannot flow off due to the high resistive rubber material. Furthermore, the static charges can also be transferred to the surface of the sensors since the rubber tip touches it there.

A STS sensor is used to investigate if handling with the red vacuum pen tip can lead to an accumulation static charges at the sensors surface which manifest in defective strips observed at measurements of its single strip parameters. This STS sensor is a special one since it was treated with a procedure which cures sensors showing an area of defective strips. This procedure is discussed in detail in section 7.4. The advantage of an already cured sensor is that an emerging area of defective strips can be better realised. Subsequently after the curing procedure the sensor was lifted with the vacuum pen for several times and remeasured after each handling series. Furthermore, measurements after certain time intervals without any handling of the sensor were performed. This should provide additional information if the area of defective strips appears during the storage of the sensor inside the dry box. In total 8 measurements were performed according to the 8 different test series.

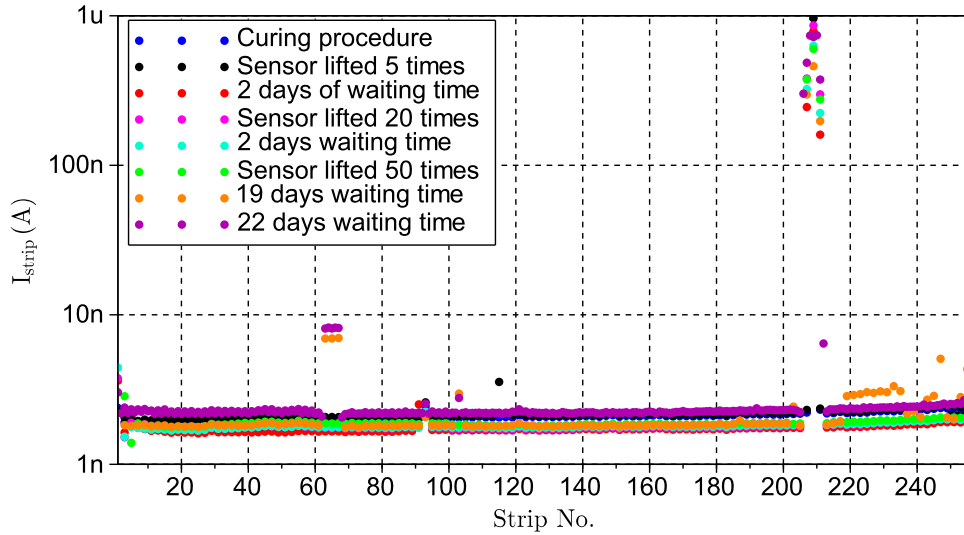


Figure 7.25: Measurement results of I_{strip} of the STS sensors used for handling tests. The legend shows the chronologic performed tests starting from top (blue) to bottom (purple).

Figure 7.25 exemplarily shows I_{strip} of the STS sensors used to investigate handling issues. All other single strip parameters show similar results. Both handling and storage of the sensor do not have significant impact on its single strip parameters. Two very narrow areas show varying measurement results. The first area is around strip number 210. All data points show there an increased single strip current. This area is already present after the curing procedure was applied. Most likely it is the residual of a previous broader defective area. The second area lies around strip number 65. The single strip current is also there increased but not that heavily as compared to the first area. Only the orange and purple data points are affected there. Both of those measurements correspond to a waiting time or storage dependence. This might indicate that the storage of the sensors could be the cause of the reappearing defective area. All measurement results which were obtained after the sensor was handled with the red vacuum pen tip are nearly coinciding. Hence, even the ESD unsafe red pen tip does not pose a threat to sensors by means of static charge generation.

7.3.3 Conclusion

The investigated treatments lead to the conclusion that the defective area of strips can be related rather to the sawing procedure than to sensor handling. All STL sensors show encouraging measurement results before a sawing procedure is applied. This indicates that previous processing steps at Infineon are not responsible for the defective area. It turned out that the method of CO_2 bubbling is an easy way to protect sensors from static charges which results in more uniform strip parameters. Nevertheless, it is unknown if the remaining defective

strips are still caused by the sawing procedure with enabled CO₂ bubbler or if other issues are responsible therefore. All investigations performed in this section lead to the assumption that the defective area occurs in between wafer sawing and measurements at HEPHY. Still uninvestigated are packaging issues which might be responsible for the reoccurrence of defective strips for sensors sawed with the CO₂ bubbler method. An intrinsic problem of sensors produced by Infineon which consequently leads to defective strips after a certain time is also not excluded. This intrinsic problem could make sensors of Infineon more sensitive to static surface charges than sensors of other vendors.

7.4 Removal of the Area of Defective Strips

Sensors produced by Infineon are not the only ones which are affected by an area of defective strips. Areas of defective strips were observed earlier at silicon strip sensors produced by another vendor. The evaluation of these sensors is in detail discussed in [10]. They reveal the same error pattern as those produced by Infineon (i.e. defective strips possibly caused by low inter strip resistances). Like for Infineon sensors it is assumed that an accumulation layer at the implant layer is responsible for the interconnection of strips. According to [10] it is possible to cure affected sensors by a bathing procedure. In particular they solely were put into deionised water for a certain time and remeasured after the bathing procedure. The result was that no defective strips could be observed anymore after bathing. In case of sensors made by Infineon the surrounding water could provide a better dissipation of static charges located at the surface. So it is assumed that sensor bathing could also be an effective and simple way to cure sensors produced by Infineon.

7.4.1 Tests Samples and Procedure

Several test runs are performed in order to investigate the effect of sensor bathing. STS sensors of batch 1 and batch 2 are primarily used but in addition also STI sensors. Sensors of batch 1 are of a special interest since they still have an unintended layer of photoresist on top of the passivation layer. This layer might influence the dissipation of static charges. Most of the sensors are bathed in tap water instead of the in [10] suggested deionised water since it has a significantly lower resistivity. It is assumed that a lower resistivity of the bathing substance provides a better dissipation of static charges. Some sensors are also bathed in deionised water. This should provide information if also a high resistive liquid is able to improve charge dissipation.

The bathing procedure itself is very simple. The sensors are put into a petri dish filled with either tap or deionised water and completely submerged. The sensors are left for 7h, 12h or even 24h inside the bath in case of tap water. Afterwards they are pulled out with a tweezer and dried by compressed air. Global and single strip parameters are measured afterwards at the QTC setup. Furthermore, two STI sensors of batch 2 are used to investigate how long it takes for defective strips to disappear [13]. Their single strip parameters are measured after

successive bathing steps. The bathing times for this study are gradually increased and ranging from 20 min to 80 min.

7.4.2 Measurement Results

Sensors exposed to high humidities usually show a degradation of their global electrical characteristics. Higher global dark currents arising from additional surface currents are most likely the consequence. Hence, one has to be aware of deviations of global characteristics caused by bathing. Deviations of the IV characteristics before and after bathing are visible for all bathed sensors. In particular the global dark current is indeed higher after bathing. However, all sensors still show reasonable global characteristics (i.e. low full depletion voltage, high breakthrough voltage) which indicates that no major damage is caused by the bathing procedure.

The results presented in the following will restrict to the single strip parameters only. This restriction is made since the aim of these studies is to investigate if the single strip parameters can be recovered by bathing. Global measurement results in contrast cannot provide any information on this topic. Furthermore, only results of I_{strip} will be presented because once again all other parameters behave similar. The description in the legend of the following graphs refers to the sensor type, the batch and their wafer number.

Sensors Bathed for 7 h in Tap Water

The measurement results of I_{strip} of sensors bathed for 7 h in tap water are shown in figure 7.26. Only STS sensors of batch 2 are used for this bathing series. It can be observed that bathing recovers most of the defective strips. Irregularities can still be found for strips lying between strip number 100 and 140. The error pattern there is different to the normally observed one. Defective strips do not show a generally increased single strip current like they show it before bathing. Instead it seems that the single strip current at this area behaves chaotic after bathing. Some of the strips even show a higher current as before. Nevertheless, all sensors have a lot less defective strips after bathing. This indicates that bathing with tap water recovers sensors produced by Infineon.

Sensors Bathed for 12 h in Tap Water

The measurement results of I_{strip} of sensors bathed for 12 h in tap water are shown in figure 7.27. One STS and two STI sensors of batch 2 are used for this bathing series. Like for the previous series the single strip currents of all sensor types recover after bathing. Hence, this procedure has a positive impact also on single strip parameters of STI sensors. This leads to the assumption that all sensor types can be cured by this procedure. Some strips still show an increased current although this bathing series lasts 5 h longer than the previous one. A further increase of the bathing time will therefore most likely not lead to a further improvement of the affected strips.

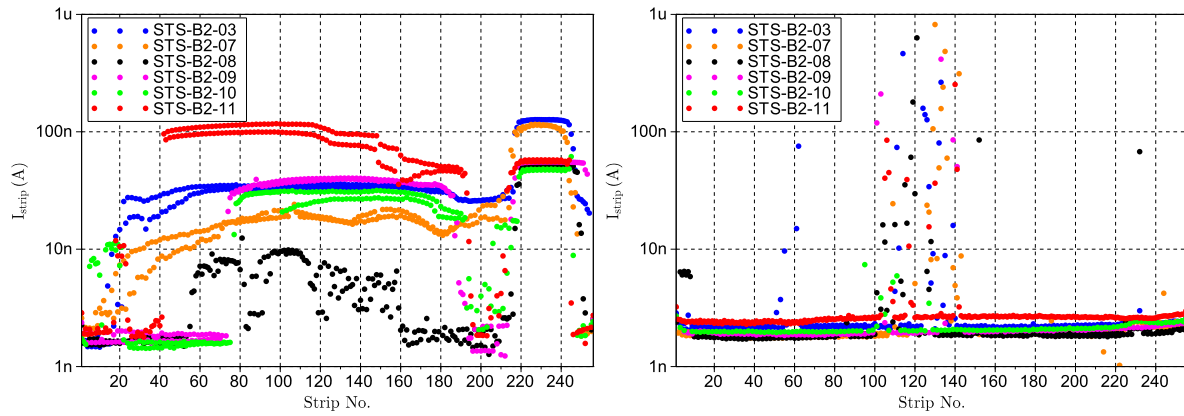


Figure 7.26: I_{strip} for STS sensors bathed for 7 h in tap water (logarithmic scale). Left: Before bathing, right: After bathing.

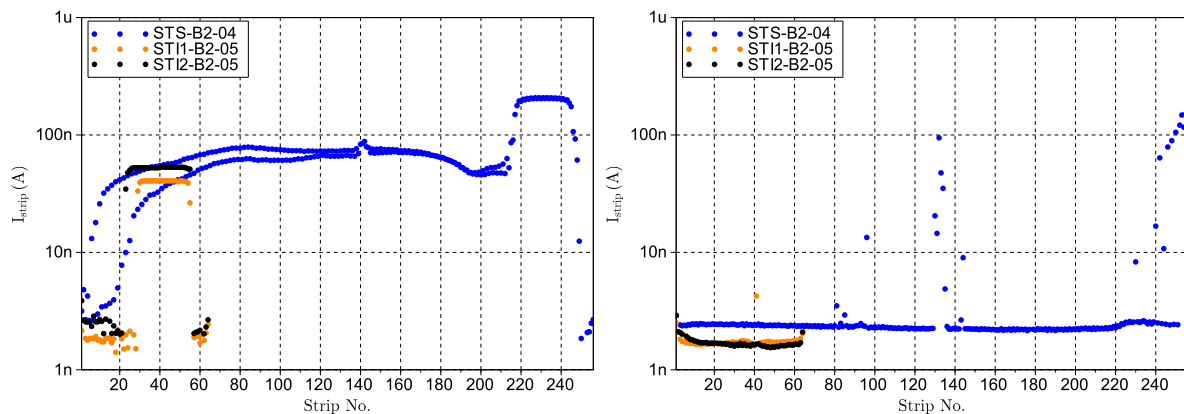


Figure 7.27: I_{strip} for STS and STI sensors bathed for 12 h in tap water (logarithmic scale). Left: Before bathing, right: After bathing.

Sensors Bathed for 24 h in Tap Water

Figure 7.28 shows the measured single strip current of STS sensors of batch 1 before and after bathing. These sensors were submerged into tap water for 24 h. Nearly all sensors still show a defective area after bathing although the bathing time is more than 3 times that long as for the first series. The unintended layer of photoresist on top of the passivation layer could be the cause for this behaviour. The measurements indicate that the photoresist on sensors of batch 1 impede the dissipation of static surface charges rather than to improve. However, the currents at the affected area at the right side of the sensors is significantly lower than before. So at least an improvement of the single strip parameters can be achieved. Some strips in the

middle of the sensor show a higher current which could already be observed for the previous bathing tests. This is remarkable since a defective area at the sensors center is not present before bathing. Hence, this could mean that bathing could also have a negative impact on sensor parameters.

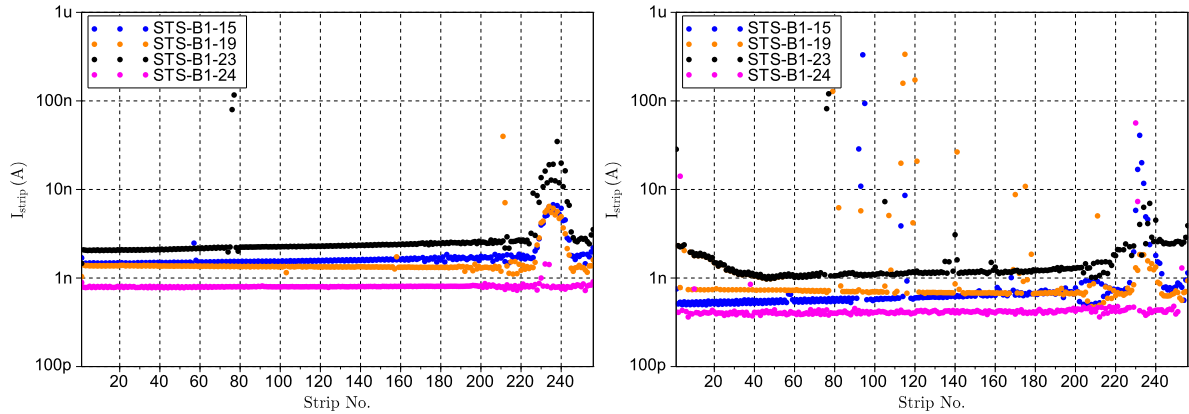


Figure 7.28: I_{strip} for STS sensors bathed for 24h in tap water (logarithmic scale). Left: Before bathing, right: After bathing.

Bathing Time Dependence

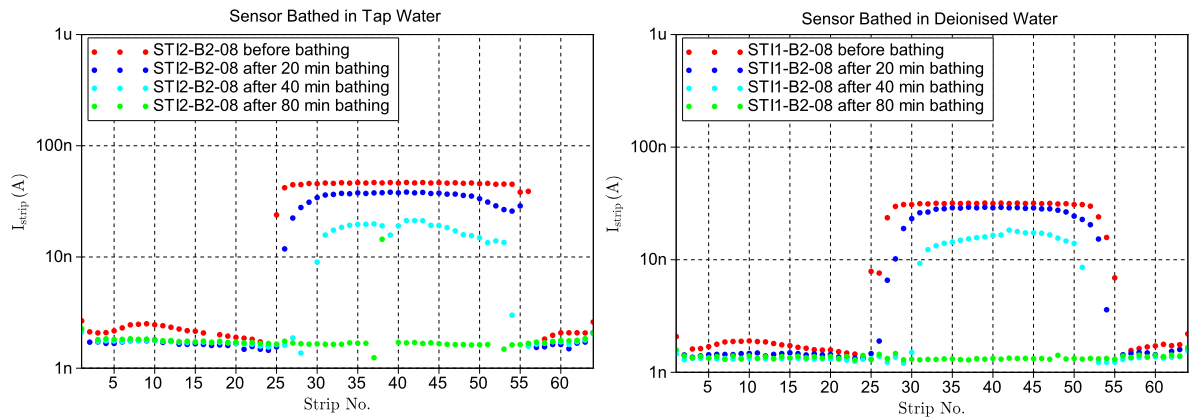


Figure 7.29: Left: Bathing time dependence of I_{strip} of a STI sensor bathed in tap water (logarithmic scale) [13]. Right: Bathing time dependence of I_{strip} of a STI sensor bathed in deionised water (logarithmic scale).

Figure 7.29 shows the results of investigations concerning the bathing time dependence of the recovery of defective strips. Two STI sensors of batch 2 are bathed in either tap (figure 7.29 left) or deionised (figure 7.29 right) water. The bathing time is successively increased from 20 min to 80 min and the single sensor parameters are remeasured after every bathing

step. The single strip currents at the defective area continuously decrease for both bathing liquids. Furthermore, the area continuously gets narrower. This observation indicates that the recovery process starts at the edges of the defective area and proceeds towards the center. The sensors are completely restored after a total bathing time of 140 min. Every other single strip parameter shows similar behaviours. The time it takes for a complete recovery of sensors is especially crucial for later performed beam and readout tests where sensors without a defective area are needed. The investigations moreover proved that also deionised water is able to restore affected sensors. It can be assumed that deionised water cures affected strips as fast as tap water since both plots of figure 7.29 are nearly identical.

7.4.3 Conclusion

Investigations performed in this section prove that bathing is able to cure the area of defective strips of sensors produced by Infineon. It turned out that sensors of batch 2 respond better on the bathing procedure than those of batch 1. Most likely the unintended layer of photoresist is responsible therefore. However, this issue is neglectable since all upcoming wafers will not have this additional layer. An estimation of the time needed to cure sensors of batch 2 could be also gained. The assumption now is that sensors bathed for more than 3 h are completely recovered. This is valid for sensors of batch 2 which are bathed in either tap or deionised water.

The optical examination of sensors bathed in tap and deionised water revealed an additional issue. Discolorations were seen at the aluminum layer resulting from bathing in tap water (see figure 7.30 left). Only directly exposed aluminum which is not covered by the passivation layer is affected. In contrast a sensor bathed in deionised water for more than twice as long shows no discolorations (see figure 7.30 right). Deposits from chalk or impurities of the tap water are the most probable cause for the observed discolorations. Future bathing will therefore restrict to deionised water which seems to be as effective as tap water.

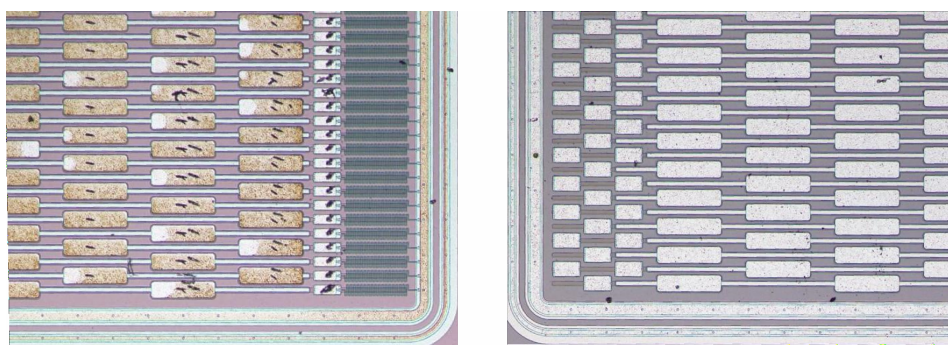


Figure 7.30: Sensor bathed for 7 h in tap water showing discolorations at the exposed aluminum (left). Sensor bathed for 16 h in deionised water showing no discolorations (right).

7.5 Examination of the Resistivity of the Passivation Layer

So far it is well comprehensible that static charges located at the surface of sensors are the most probable cause for the observed defective areas. Results gained by FET-like measurements, sawing methods and bathing studies consolidate this hypothesis. It is still questionable why sensors produced by other vendors do not show similar error patterns as those observed for sensors produced by Infineon. Investigations presented in section 7.1 at least indicate that also their single strip parameters are sensitive to static surface charges. Section 7.3 revealed that the charge accumulation and hence the defective area occurs between sawing and characterisation measurements at HEPHY (at least in case of sensors sawed with the CO₂ bubbler method). Thus, sensors of other vendors which are stored and measured at HEPHY should also be exposed to externally applied charges like it is assumed for sensors produced by Infineon. This section investigates therefore a possible issue which might improve the resilience against surface charges. An improved resilience could explain why sensors produced by other vendors do not show a defective area of strips.

Samples of different vendors are available allowing comparison. In particular comparisons of different sensor structures of sensors produced by five different vendors are in detail carried out in [17]. Results gained in [17] along with an additional literature research revealed that especially the passivation layer differs among the major vendors. Beside variations of the thicknesses, different kinds of materials are used to passivate silicon strip sensors. The electrical properties of this uppermost layer might influence the dissipation of static charges located thereon. It is assumed that established vendors adjust the composition of this layer in order to support the dissipation of eventually applied surface charges. This could explain why only sensors produced by Infineon show a defective area of strips.

Infineon provided the information on the composition of the passivation layer in order to support investigations performed in this thesis. In particular silicon nitride (Si_xN_y) is used where the exact composition is not defined due to the deposition process itself. In addition to silicon nitride, phosphorus silicate glass (PSG) and silicon dioxide (SiO₂) are commonly used passivation materials in semiconductor industries. It turned out that two major vendors indeed use these materials as passivation. PSG and SiO₂ could be assigned to either one of the two major vendors with the assistance of results gained by energy-dispersive x-ray spectroscopy (EDX) performed in [17]. In the following PSG is associated to vendor 1 and SiO₂ to vendor 2 for legal reasons.

The resistivity of the passivation layer is the most crucial parameter when it comes to the ability of static charge dissipation. High resistivities of all passivations are assumed since their task is to act as an electrical isolation and furthermore as a mechanical and chemical barrier against environmental influences. Nevertheless, a resistivity value of one magnitude less than compared to those of other passivation materials could already lead to a better long term charge dissipation behaviour. This in turn would manifest in an improved resilience against static charges. Precise measurements of the resistivity of the different passivation materials are therefore carried out in this section. The primary assumption is that the resistivity of the passivation of sensors produced by Infineon is significantly higher than those of other vendors.

If this assumption can be validated it would provide a further hint why sensors manufactured by other vendors do not show defective areas of strips like sensors produced by Infineon.

7.5.1 Test Samples

The resistivity of the different passivation materials is determined by precise measurements of a traversing current (a detailed description gives 7.5.2). In general such measurements can be compared to measurements of the leakage current flowing through a dielectric layer of a capacitor. Dedicated test structures for such measurements are unfortunately not implemented on wafers produced by any of the three considered vendors. This is not surprising since the passivation layer is the uppermost one which consequently leads to complications concerning the design of such structures. Actually an additional layer on top would have to be added in order to enable resistivity measurements of the passivation layer. This however will consequently boost prices. Therefore, samples have to be constructed that allow to perform the intended resistivity measurements. It turned out that some already existing structures are also appropriate although they were not designed for that kind of purpose.

The used test samples can be divided into two groups. The first group are self made MIM samples (see figure 7.31 right). This nomenclature is given due to their three layer sandwich design made of metal-insulator-metal (MIM) where the insulator refers to the passivation. Locations at the wafer where broad areas of aluminum are covered by passivation are used as the first metal layer. The second metal layer has to be applied externally on top of the insulating material⁴.

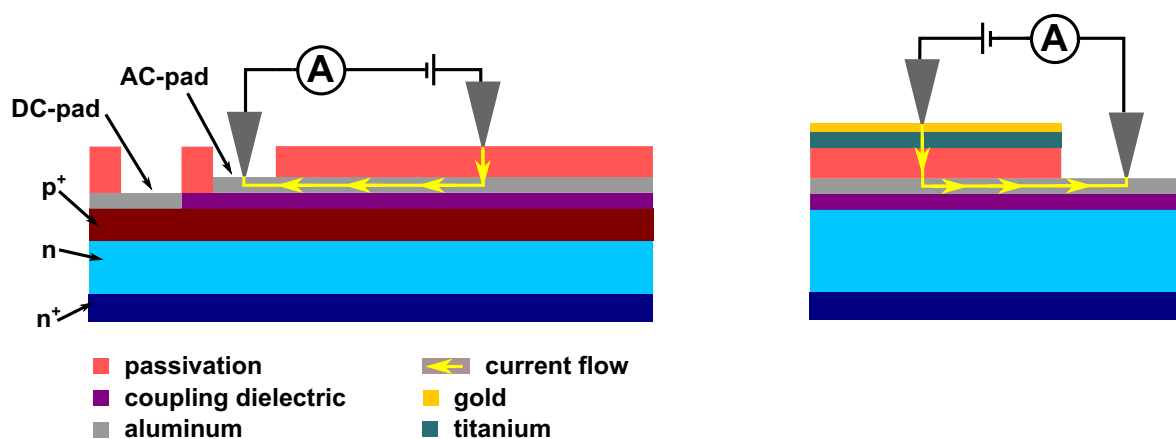


Figure 7.31: Schematic cross section of the two different kinds of samples used to measure the resistivity of the passivation layer. Left: Strip sample, right: MIM sample. In addition the connection of probe needles and a simplified circuit used for the actual measurement is shown.

⁴ Once again the Institute of Solid State Electronics offered their expertise in order to sputter a titanium-gold pad directly onto the passivation for this purpose.

The other group of test samples are already existing structures. Those structures are de facto small silicon strip sensors and therefore denoted as strip samples (see figure 7.31 left). Resistivity measurements of the passivation are also here realised using metal-insulator-metal structures. The narrow aluminum strips constitute the metal layer beneath the passivation instead of a broad area of aluminium like for MIM samples. The AC-pads enable the necessary connection to every strip. The second layer of aluminium is realised by a part of the measurement circuitry i.e. a tungsten carbide probe needle which contacts the passivation directly above the aluminum strip. The resulting structure used for measurements is very similar to that of MIM samples with the exception that no sputter process is necessary.

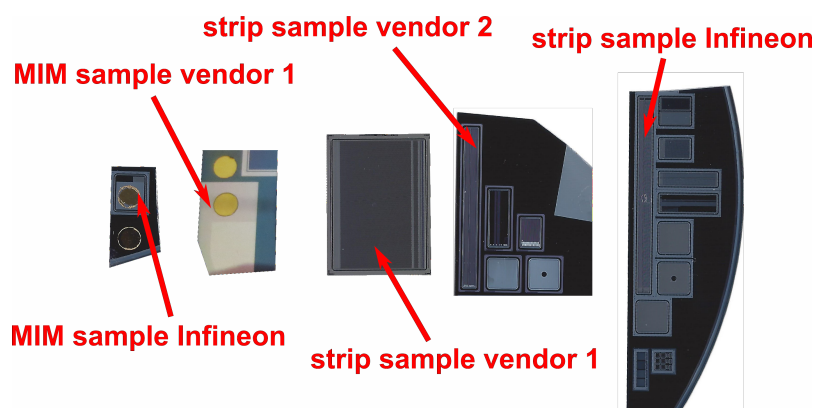


Figure 7.32: MIM and strip samples of different vendors used for measurement of the resistivity of the passivation layer.

Figure 7.32 shows pictures of strip and MIM samples of every of the three considered vendors. MIM samples of vendor 2 are unfortunately not available since comparable structures could not be ascertained on wafers of this vendor. Furthermore, an important detail for samples of vendor 1 has to be mentioned. Scanning electron microscope (SEM) pictures which were made in context of [17] revealed that the passivation layer of this vendor actually consists out of two layers made out of different materials. Most likely, the upper layer is made out of the already mentioned PSG. The lower one on the contrary, is most likely made out of SiO_2 . Again EDX measurements made in context of [17] lead to this assumption. Two layers of passivation impede the envisaged resistivity measurements of the uppermost layer since the current used to calculate the actual resistivity is flowing vertically through the passivation layer (see figure 7.31). The obtained resistivity value is therefore a composition of the resistivity of the lower and upper layer. This fact has to be considered for comparisons of resistivity values of the different passivations which are presented later.

The materials used by the different vendors to passivate sensors, their thickness and the corresponding uncertainties are summarized in table 7.2. The thickness of the passivation is determined by SEM pictures made in context of [17] except for Infineon which provided this information. The uncertainty of the thickness is assumed to be equal for every of the investigated passivations and is also provided by Infineon. Variations at the deposition processes

however lead to a relatively coarse estimation of this uncertainty.

Vendor	Material	Thickness (nm)	Uncertainty (nm)
Infineon	Si _x N _y	750	50
Vendor 1	SiO ₂ + PSG	200 + 413	50
Vendor 2	SiO ₂	400	50

Table 7.2: Characteristics of test samples used for resistivity measurements.

7.5.2 Measurement Procedure

Principle of Resistivity Measurements

As already mentioned resistivity measurements of high resistive samples can be traced back to precise measurements of a current flowing through. In order to enable a current flow a potential difference has to be applied at the sample which consequently evokes an electrical field inside. The resistivity can be calculated if the absolute value of the electrical field E is divided by the absolute value of the current density J (see equation 7.7) .

$$\rho = \frac{E}{J} \quad (7.7)$$

The magnitude of the electrical field is obtained by the ratio of the applied voltage V and the thickness of the sample d i.e. $E = \frac{V}{d}$. This simplified approach is valid since an uniform electrical field inside the sample is assumed. The current density can be obtained if the measured current I is divided by the cross section area A where the current is flowing through i.e. $J = \frac{I}{A}$.

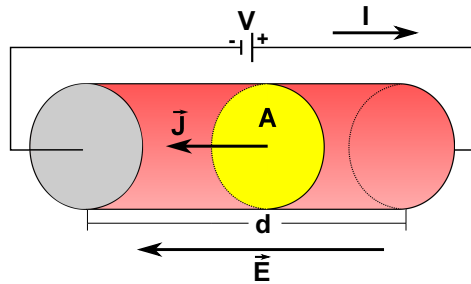


Figure 7.33: Correlation of different parameters used for calculations of the resistivity.

The magnitude of the applied voltage has to be divided by the thickness of the passivation layer in order to obtain the magnitude of the electrical field inside samples used for resistivity measurements of the passivation layers. Those thicknesses are displayed in table 7.2. The area traversed by the measured current corresponds to either the area of the contacting probe needle tip (strip samples) or the area of the sputtered pad (MIM samples). They are examined

with the use of microscopic images and summarised in table 7.3. The utilization of these areas is appropriate since the areas of the metal layers beneath the passivation are larger than the mentioned ones for both kinds of samples. Hence, the current flow is regional limited by the areas displayed in table 7.3. The relatively large uncertainties are intended since only coarse estimations could be gained.

	Area	Uncertainty
Sputtered pad	22.2 mm ²	3.3 mm ²
Needle tip	452 μm ²	113 μm ²

Table 7.3: Area and corresponding uncertainties for strip and MIM samples.

Simplified circuits corresponding to the two kinds of test samples which are used to measure the current flowing vertically through the passivation layer are shown in figure 7.31. Together with the previously made assumptions concerning current density and electrical field calculations of the actual resistivities can be performed.

Error Sources

Several error sources impede precise measurements of resistivities of different passivation layers. Especially the externally applied pad and the tungsten carbide probe needle limit the measurement accuracy. The sputtered pad is generally very sensitive to mechanical stress and can easily be peeled away. This leads to significantly higher uncertainties of the actual area than shown in table 7.3. The tungsten carbide probe needle used for measurements of strip samples induces several error sources too. The brittle alloy tends to break which makes precise estimations of the contacting area impossible. Actually the area increases after every break off due to the cone shape of the needle. The fact that the needle contacts the passivation directly induces an additional error source. It is not exactly known how far the needle is penetrating into the passivation. Large relative uncertainties of the actual passivation thickness are the consequence even if the needle penetrates only a few nm into it. However, uncertainties of the current density and the electrical field are calculated from those displayed in table 7.2 and 7.3. The described additional error sources state that larger errors are in any case possible.

Measurement Methods

Generally the behaviour of the current-voltage characteristics of the investigated high resistive passivation layers can be compared to those of a lowpass filter (see figure 7.34 left). The current is time dependent and determined by the capacitance of the capacitor C and the resistance of the resistor R inside the circuit. The product of these is known as time constant tau, $\tau = RC$. In particular the time dependent current is given by equation 7.8.

$$I(t) = I_0 \cdot \exp\left(\frac{-t}{RC}\right) \quad (7.8)$$

The maximum current $I_0 = U/R$ is flowing at the beginning of charging and discharging of the capacitor (i.e. when the voltage is applied or removed) and is exponentially decreasing with time (see figure 7.34 right). The capacitor shown in the lowpass filter circuit corresponds to the actual test sample (strip or MIM) and the resistance to the input impedance of the amperemeter and additional line resistances.

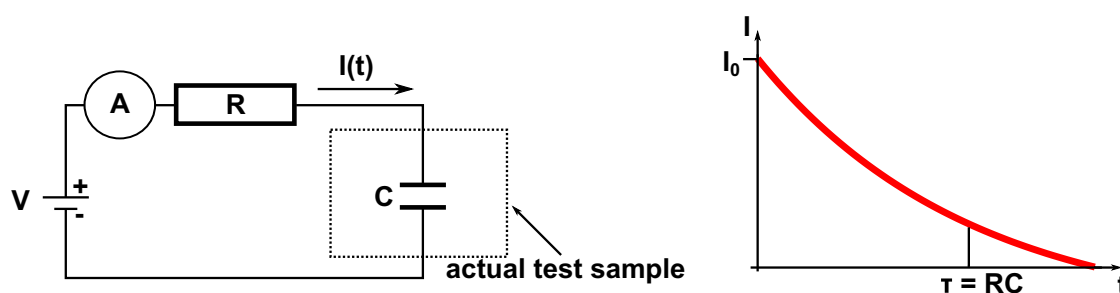


Figure 7.34: Equivalent circuit diagram for current measurements used to determine the resistivity (left). Time dependence of the current (right).

Measurements of the conductivity (reciprocal of the resistivity) of high resistive dielectric films were already performed in [18]. Different kinds of methods are presented there in order to determine the traversing current. Two of the in [18] discussed methods are also suitable for the intended measurements of this section.

The first measurement method is called staircase mode. Within this method the voltage at the sample is successively increased and the time dependent current which is flowing through is recorded (see figure 7.35). The average of the measured current after a waiting time of $t > \tau$ is used, in order to gain a single current value for every voltage step.

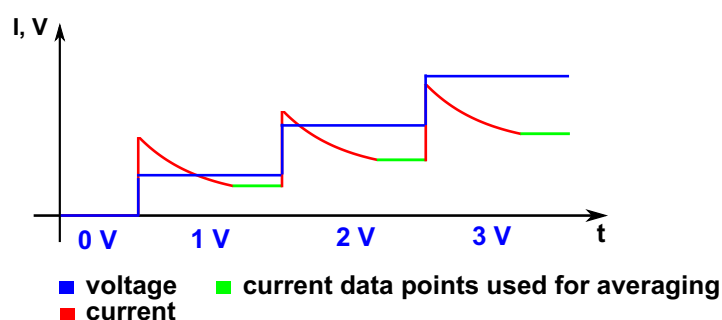


Figure 7.35: Scheme of the staircase mode.

The waiting time t is arbitrary but has to be chosen sufficiently long since the value of τ is not known. In practice t corresponds to the time where the current does not decrease anymore. This time has to be adjusted newly for every test sample. The average current corresponds to the current flowing through the passivation layer. This current is equal to zero for an ideal capacitor. Along with the voltage, the thicknesses of the passivation layers and the area of the pad or needle, the resistivity can be calculated.

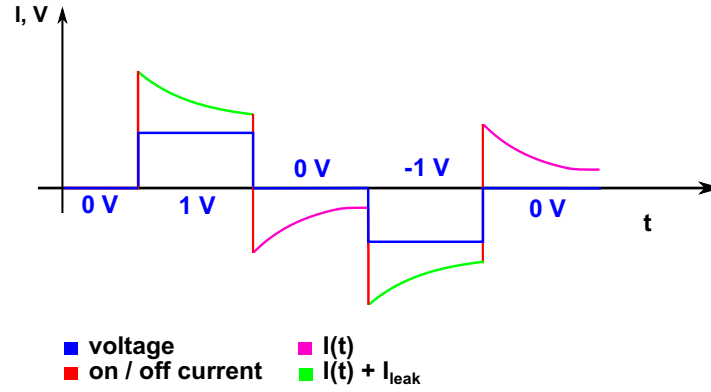


Figure 7.36: Scheme of the pulse mode.

The second measurement method is called pulse mode (see figure 7.36). By this method the voltage at the sample is periodically applied and removed. If the voltage is applied, the total measured current I_C^{tot} consists of the time dependent charging current $I_C(t)$ and the leakage current I_{leak} which is flowing through the sample. In contrast only the time dependent discharge current $I_D(t)$ is flowing if the voltage is removed. In case of lowpass filters the absolute values of the time dependent charging and discharging currents are equal to the current displayed in equation 7.8:

$$|I_C(t)| = |I_D(t)| = I(t). \quad (7.9)$$

Thus, if the absolute value of the total measured charging current is subtracted by the absolute value of the discharging current one obtains the actual leakage current:

$$|I_C^{\text{tot}}| - |I_D(t)| = I(t) + |I_{\text{leak}}| - I(t) = |I_{\text{leak}}|. \quad (7.10)$$

In practice every data point of the charging curve is subtracted by the corresponding one of the discharging curve. Afterwards the average of every difference is taken as the actual current which corresponds to the used charging voltage. This method can likewise be used for negative and positive voltages which offers crosschecking abilities of the gained results. The relationship of the leakage current and voltage can be obtained if the calculation displayed in equation 7.10 is repeated for several increasing voltage steps. The pulse mode is more sophisticated than the staircase mode and less prone to errors. The biggest error source of the staircase mode results from the waiting time t which is more or less estimated. The pulse mode in contrast is free of this parameter.

7.5.3 Measurement Setup

Circuitry Used for Precise Current Measurements

Both currents gained either by the staircase or pulse mode are assumed to be very small. Because of that a Keithley 6514 electrometer is used for measurements of the current flowing through the passivation layer. This instrument offers a resolution of up to 1 fA. On the other hand a Keithley 237 SMU serves as a voltage source. These two measurement instruments are already sufficient for the envisaged circuit shown in figure 7.37. The two outputs (respectively inputs) are connected to positioners with incorporated tungsten carbide probe needles. In case of strip samples one needle is connected to the AC pad and the other one directly onto the passivation above the strip. Whereas for MIM samples one needle is connected to the broad area of aluminum below the passivation and the other one to the sputtered pad.

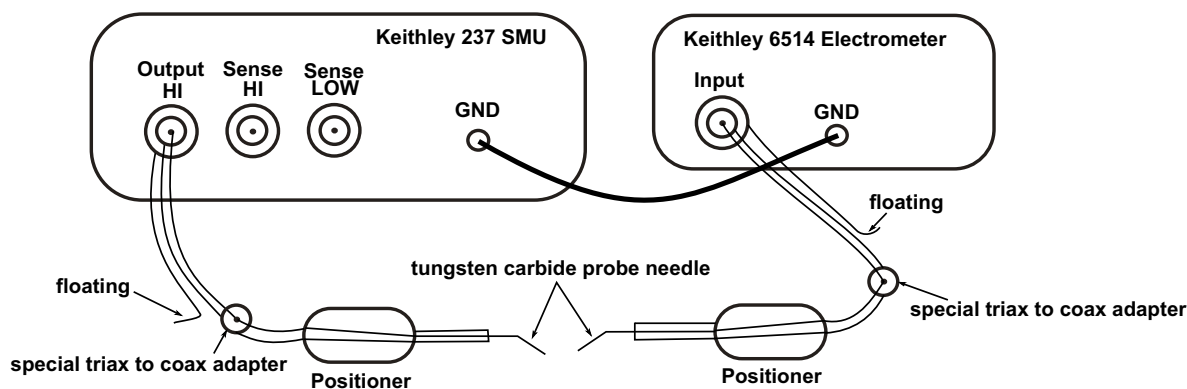


Figure 7.37: Circuit used for current measurements. Every conductor of the triaxial respectively coaxial cable is shown.

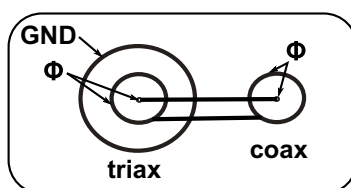


Figure 7.38: Inner circuitry of the special triax to coax adapter.

Especially cabling is an important issue when it comes to precise current measurements. In particular triaxial cables are used for the whole cabling. More precise current measurements can be performed therewith due to an additional coaxial conductor which is on the same potential as the sense wire in the center. A leakage current flowing between core and this additional conductor is therefore prohibited which results in lower noise and thus an improved measurement of small currents. However, the positioners itself can only be connected to coaxial cables. Along with a special triax to coax adapter it is possible to connect the additional

coaxial conductor of the triaxial cable to the shield of the coaxial cable (see figure 7.38). Therewith, a leakage current flowing from core to shield is also prohibited for coaxial cables since both conductors have the same potential.

Measurement Setup Used for Resistivity Measurements of Strip and MIM Samples

Beside QTC and PQC a third probe station called P3 is available at HEPHY. Mostly it is used for sensor readout tests but several other tests and circuits can be realised too due to its high flexibility. In particular the P3 setup is suitable for resistivity measurements of either strip or MIM samples. An additional feature of the P3 is a scale which improves the error estimation of the thickness of the passivation layer. The scale is used to measure the contacting weight of the probe needle touching the passivation. The assumption is that if the pressure of the needle is too high it penetrates the passivation which reduces the effective thickness. This consequently leads to unestimated large errors of the calculated electrical field. The contacting weight can be adjusted via an x-y-z table or manually. Furthermore, a LabVIEW software monitors the weight during the whole measurement. The needle contacting the AC pad of the strip sample is located at the same table as the scale which enables the adjustment of the second needle via the x-y-z table after taring. The measurement of the contacting weight is especially important for strip samples since the needle is directly touching the passivation layer.

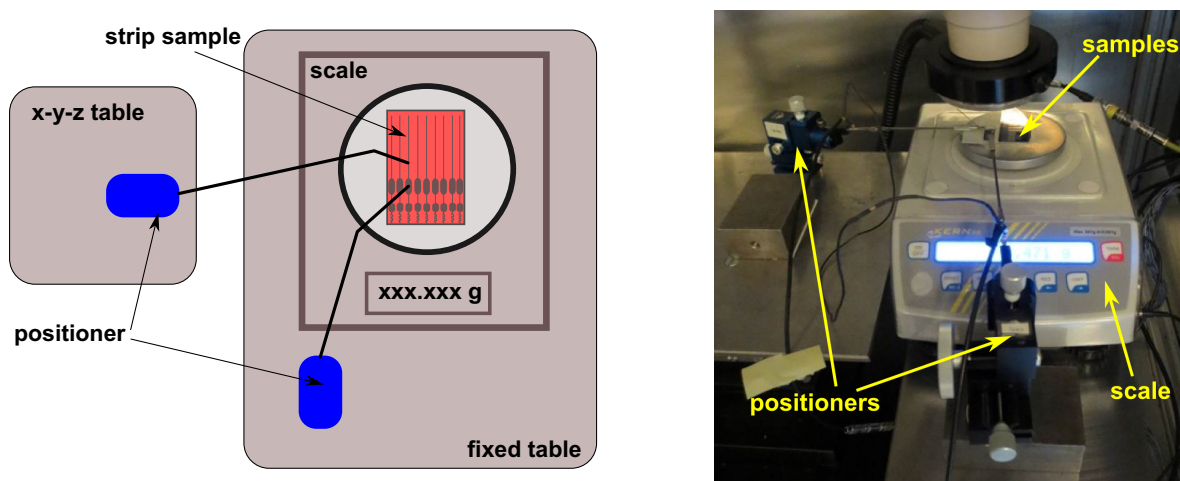


Figure 7.39: Left: Schematic view of the measurement setup (measurement of a strip sample is displayed), right: Picture of the used setup.

The setup displayed in figure 7.39 is likewise used for MIM samples although the scale is not essential here. It is assumed that the thickness of the sputtered pad is sufficient to prohibit the intrusion of the needle into the passivation. Nevertheless, the contacting pressure is carefully adjusted and kept low even for that kind of samples.

7.5.4 Measurement Results

Preliminary Remarks

All measurement results are pictured as plots where the current density is plotted against the electrical field. The resulting curves should be straight lines and the slopes should correspond to the inverse of the resistivity (see equation 7.7). It turned out that this naive assumption is not valid. Several secondary effects like the Poole-Frenkel effect, Schottky-Richardson emission and Fowler-Nordheim tunneling disturb the desired ohmic behaviour (a detailed description is given [18]). In particular the current density has an exponential dependency of the electrical field for all mentioned effects. The secondary effects have major impact especially at high field strengths. Indeed all measurement results show an exponential curve shape which is exemplarily illustrated in figure 7.40.

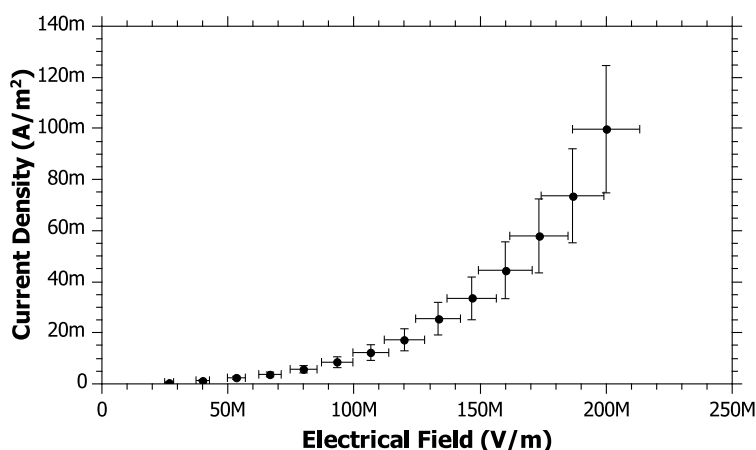


Figure 7.40: Exemplary measurement result showing the exponential behaviour of the current density.

The secondary effects hinder the calculation of the resistivity of different materials used for sensor passivation since no defined slope can be ascertained. Nevertheless, comparisons between different vendors can be made. The current density is plotted logarithmically for the measurement results presented in the following in order to have a better ability to discriminate the single measurement curves.

The electrical sensitivity of samples is an additional issue hindering a detailed analysis of different resistivities. In fact most of the measurements of either strip or MIM samples delivered non reasonable results. The most common cause therefore is that the current was too small for the capability of the electrometer. In addition breakthroughs which emerged if the two metal layers are shorted were observed for several samples. Furthermore, several measurements were discarded due to heavy noise. All these issues lead to the fact that a broad statistical analysis cannot be performed which consequently reduces the significance of the non-discarded measurement results.

Measurement Results Obtained by Staircase Mode

Figures 7.41, 7.42 and 7.43 show the non-discarded measurement results of strip samples of every vendor gained by the staircase mode. The legend displays the measurement number and the contacting pressure of the needle. Every measurement is performed on a separate strip but on one strip sample of each vendor.

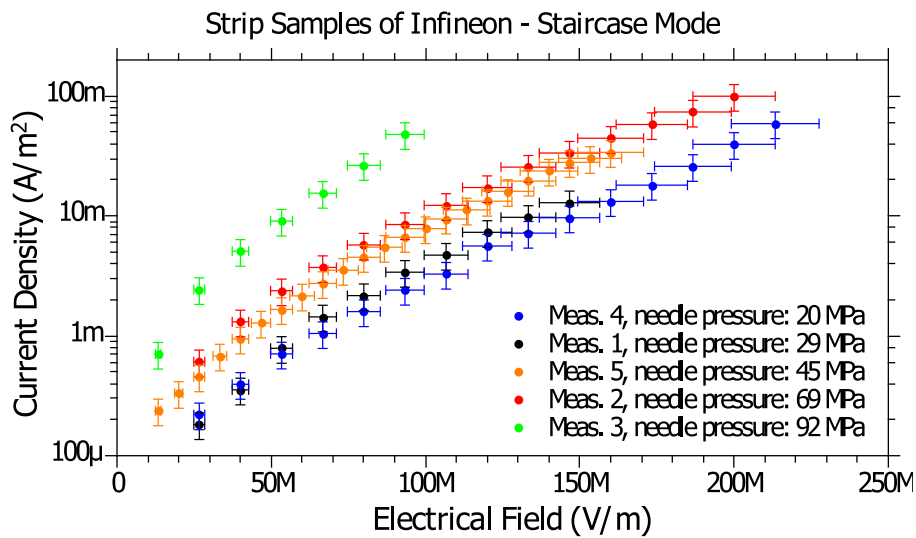


Figure 7.41: Measurement results of an Infineon strip sample obtained by the staircase mode (logarithmic y-axis, arranged in order of pressure).

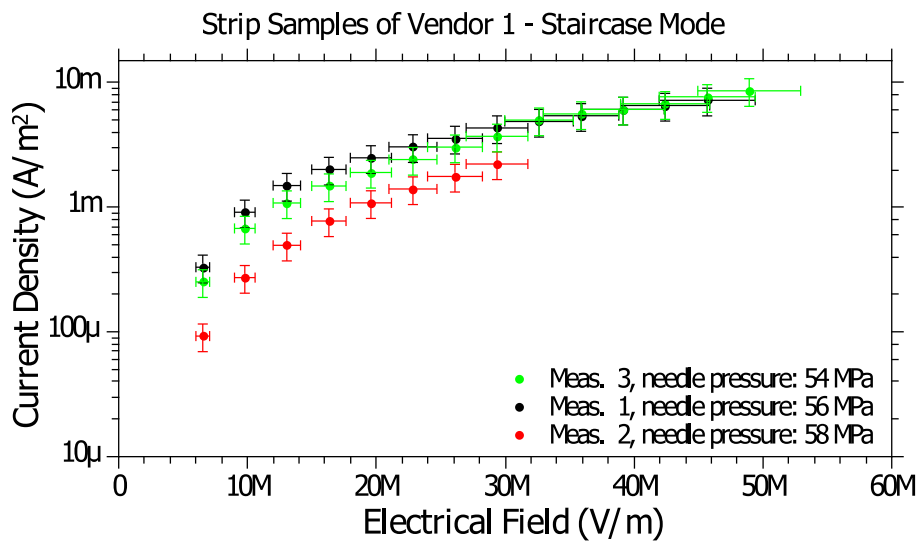


Figure 7.42: Measurement results of a strip sample of vendor 1 obtained by the staircase mode (logarithmic y-axis, arranged in order of pressure).

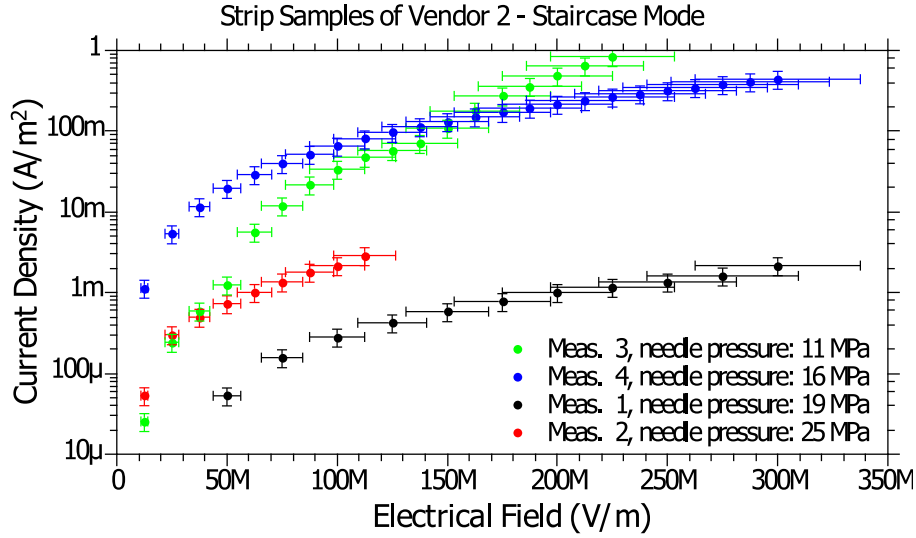


Figure 7.43: Measurement results of a strip sample of vendor 2 obtained by the staircase mode (logarithmic y-axis, arranged in order of pressure).

The error bars are calculated with the method of linear error propagation:

$$\Delta E = \left| \frac{\partial U}{\partial d} \right| \cdot \Delta d = \frac{U}{d^2} \cdot \Delta d \quad (7.11)$$

$$\Delta J = \left| \frac{\partial I}{\partial A} \right| \cdot \Delta A = \frac{I}{A^2} \cdot \Delta A \quad (7.12)$$

where Δd corresponds to the uncertainty of the thickness of the passivation layer and ΔA to the uncertainty of the area of the contacting needle (both are given in table 7.2 respectively 7.3). The error bars for every other presented measurement are obtained in the same way.

Results displayed in figures 7.41, 7.42 and 7.43 state that the measurements are in general not reproducible. The variation of the needle pressure could be a probable cause therefor. Higher pressures should evoke higher current densities since the effective electrical field strength is higher due to the effectively lower passivation thickness. Results of vendor 2 (figure 7.43) on the contrary indicate that this is not necessarily true. The lowest needle pressure there corresponds to one of the highest current densities. A further conspicuity is that measurements of sample of vendor 1 could only be performed up to field strengths of maximum 50 MV/m due to early breakthroughs. This fact hinders comparisons between different vendors. However, at least comparisons at 50 MV/m can be performed. The sample of Infineon shows a maximum current density of about 7 mA/m², the sample of vendor 1 of about 8.6 mA/m² and the sample of vendor 2 of about 19.6 mA/m² at 50 MV/m. Hence, the lowest current density corresponds to the sample of Infineon which indicates that its passivation has the highest resistivity. More than this indication can not be gained since the current density has generally no linear behaviour as it was assumed previously and due to several error sources.

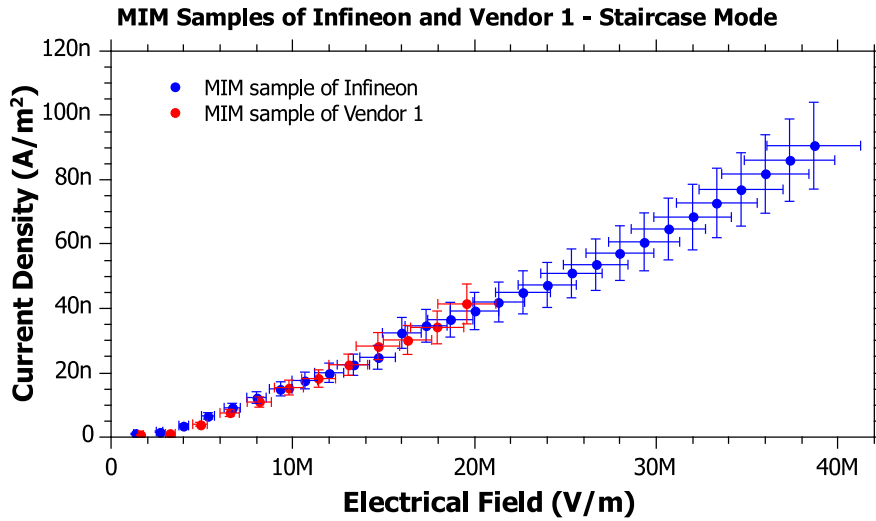


Figure 7.44: Measurement results of a MIM sample of Infineon and vendor 1 obtained by the staircase mode (linear y-axis).

Figure 7.44 shows results obtained of MIM samples of Infineon and vendor 1 by the use of the staircase mode. It is conspicuous that the current density behaves more linear than compared to strip samples. A probable reason for this behaviour might be that the mentioned secondary effects preferentially occur at higher electrical field strengths. A further increase of the field strength, however, was once again hindered by observed early breakthroughs. In general MIM samples are destroyed by high breakthrough currents which impede reproducible measurements of one and the same sample. However, the slope of both curves is nearly identical which indicates that both resistivities coincide. This statement is compatible to results gained of strip samples where both Infineon and vendor 1 have resistivity values of the same magnitude. Once again it has to be mentioned that comparisons with vendor 1 are in general impaired by the fact that this vendor uses two layers of passivation. The design of the samples enforces that the measured current from which the actual current density is calculated is flowing vertically through both layers. Therefore, the considered resistivity of vendor 1 is a combination of the resistivities of both layers.

Measurement Results Obtained by Pulse Mode

The pulse mode offers the ability to change the polarity of the applied voltage as displayed in figure 7.36. Hence, charging and discharging currents can be measured for different polarities which offers the possibility of a crosscheck of the obtained current densities. In particular charging and discharging currents are measured consecutively for positive and negative voltages. The pulse mode is, compared to the staircase mode, the more sophisticated method since the error source arising from the unknown time constant τ can be neglected. Results gained by the pulse mode are therefore more plausible. However, early breakthroughs and heavy noise impede a broad statistical analysis like for the staircase mode. Only one strip

sample of vendor 2 and Infineon and only one MIM sample of vendor 1 and Infineon delivered reasonable results.

Figure 7.45 shows the measurement results obtained for positive and negative voltages of a strip sample of vendor 2 and Infineon. The pressure of the needle contacting the passivation is about 30 MPa for both samples. In general the current density of the sample of vendor 2 is higher than for the sample of Infineon over the whole field strength range. This statement is valid if one compares the curves of the different vendors obtained for either negative or positive voltages. The results obtained for negative and positive voltages of one vendor are only comparable for low electrical field strengths. Higher field strengths are causing discrepancies between current densities gained for different polarities.

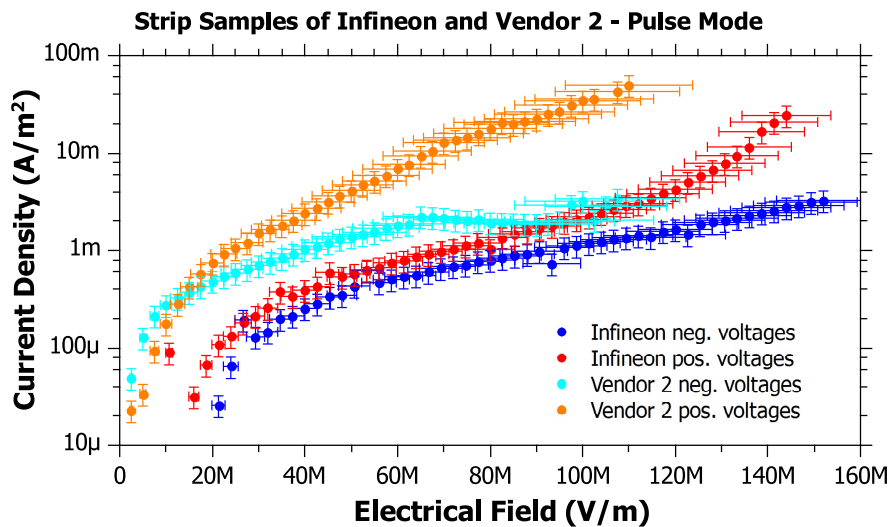


Figure 7.45: Measurement results of a strip sample of vendor 2 and Infineon obtained by the pulse mode (logarithmic y-axis).

Results displayed in figure 7.45 suggest that the passivation of Infineon has a higher resistivity than the one of vendor 2. This assumption is in accordance with results obtained by the staircase mode.

Figure 7.46 shows the measurement results obtained for positive and negative voltages of a MIM sample of vendor 1 and Infineon. In case of MIM samples of Infineon, measurements beyond 50 MV/m could not be conducted because of early breakthroughs. It can be observed that results obtained for negative and positive voltages of one vendor are now better coinciding than compared to strip samples. Furthermore, even more distinct differences between the current densities of the different vendors are visible than compared to figure 7.45. The sample of vendor 1 has a significantly higher current density than the sample of Infineon. Hence, it appears save to assume that the resistivity of the passivation layer of Infineon has a higher resistivity than the passivation of vendor 1. This perception is contrary to results obtained for MIM samples measured with the staircase mode (7.44). The statement given here is more plausible since it is believed that the pulse mode provides more accurate results. Once again it

has to be mentioned that vendor 1 uses two passivation layers. Statements about the resistivity of this vendor can therefore only be made for the combined resistivity of both layers.

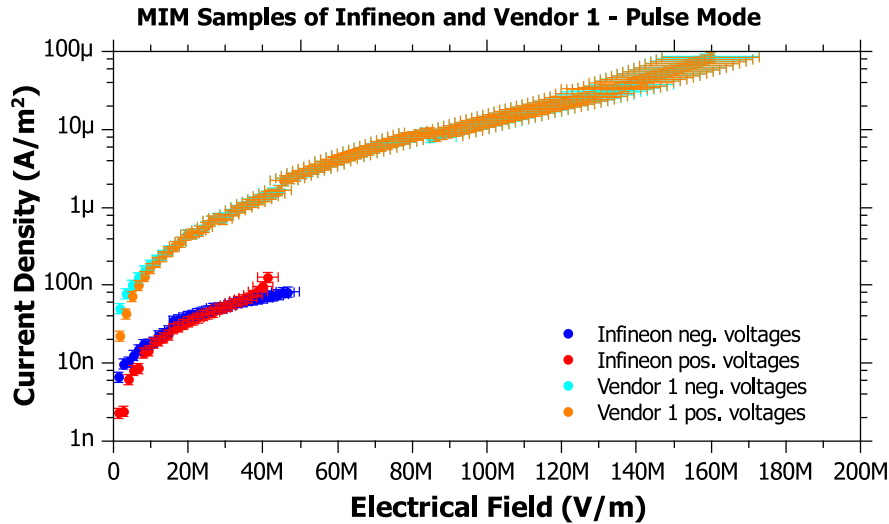


Figure 7.46: Measurement results of a MIM sample of vendor 1 and Infineon obtained by the pulse mode (logarithmic y-axis).

7.5.5 Conclusion

The majority of results gained either by the staircase or pulse mode indicate that the resistivity of the Si_xN_y passivation of Infineon is indeed larger than those of the other major vendors. However, large error sources and low statistics retain the possibility of a different conclusion.

The assumption that the dissipation of eventually applied surface charges is hindered by the higher resistive passivation of Infineon became more plausible. It is on the contrary still unknown if the lower resistivity of the passivation layers of other vendors is especially adjusted for the purpose of charge dissipation or not. It is also questionable if the upper passivation layer of vendor 1 has a lower resistivity than that of Infineon. Actually the resistivity of the surface of the passivation has to be measured in order to obtain comparable results. Discussions with Infineon for the application of suitable structures for this purpose are ongoing.

8 Environmental Stress Tests Using a Climate Chamber

Silicon strip sensors installed inside the CMS tracker are generally operated under well defined environmental conditions. The temperature for example is adjusted between -10°C and -20°C [19] by the use of a liquid cooling system. Cooling of sensors made out of silicon is an important issue since thermally generated charge carriers are reducing the signal to noise ratio. Even more important is that cooling counteracts the effect of thermal runaway. This effect occurs if the temperature dependent leakage current $I_0(t)$ of equation 2.10 increases (for example after irradiation). Higher leakage currents lead to higher power dissipated inside the silicon strip sensors which results in an increase of temperature and consequently to an even more increased current. This procedure eventually leads to a continuously increasing current.

The humidity inside the CMS tracker is another important issue concerning sensor (or more precise module) operation beside the demand of a controlled and monitored temperature. An envelope around the silicon tracker filled with nitrogen (or dry air respectively) [19] ensures that the dew point is always below the temperature of the cooling liquid. Thus, no condensation is possible at the cooling pipes which could harm the sensitive electronics. In particular the envelope atmospherically isolates the silicon tracker from the rest of the experiment which is operated at room temperature. The resulting large temperature gradients inside CMS naturally force condensation which makes atmospheric isolation of the silicon tracker indispensable. Moreover, high relative humidities are able to cause a degradation of the electrical properties of silicon strip sensors.

However, environmental conditions are generally not defined at quality tests, module assembly, packaging and transportation. It is imaginable that every sensor might have to endure partly harsh environmental conditions during the mentioned procedures. Even if sensors are exposed to such harsh conditions only for a short time, major damage could be the consequence. The following chapter investigates the temperature and humidity dependence of the global leakage current of silicon strip sensors manufactured by Infineon. Test structures of sensors currently used in CMS are used as reference samples and pass the same tests as sensors manufactured by Infineon. Anomalies of the electrical behaviour at extreme temperatures or relative humidities would indicate a poor resilience against environmental influences. This in turn could probably result in a bad longterm stability. The longterm behaviour of global sensor properties is also investigated beside the simulation of harsh environmental conditions. In particular, the considered sensors are exposed to varying humidities over a relatively long time scale. The longterm behaviour is of a special interest since sensors cannot be replaced once they are built into the actual tracker.

8.1 Climate Chamber Test Setup

The climate chamber at HEPHY is used to investigate the temperature and humidity dependence of the electrical properties of silicon strip sensors (see figure 8.1). It is one of the most recent investments and operated for the first time for investigations made in the context of this thesis. Hence, commissioning of the setup and programming (in fact reprogramming) of a suitable LabVIEW measurement software was mandatory. Longterm stability tests using a self-made climate chamber were already previously carried out at HEPHY but for different types of sensors and with a different setup [8]. However, the chamber described in the following is much more sophisticated especially when it comes to humidity adjustments.

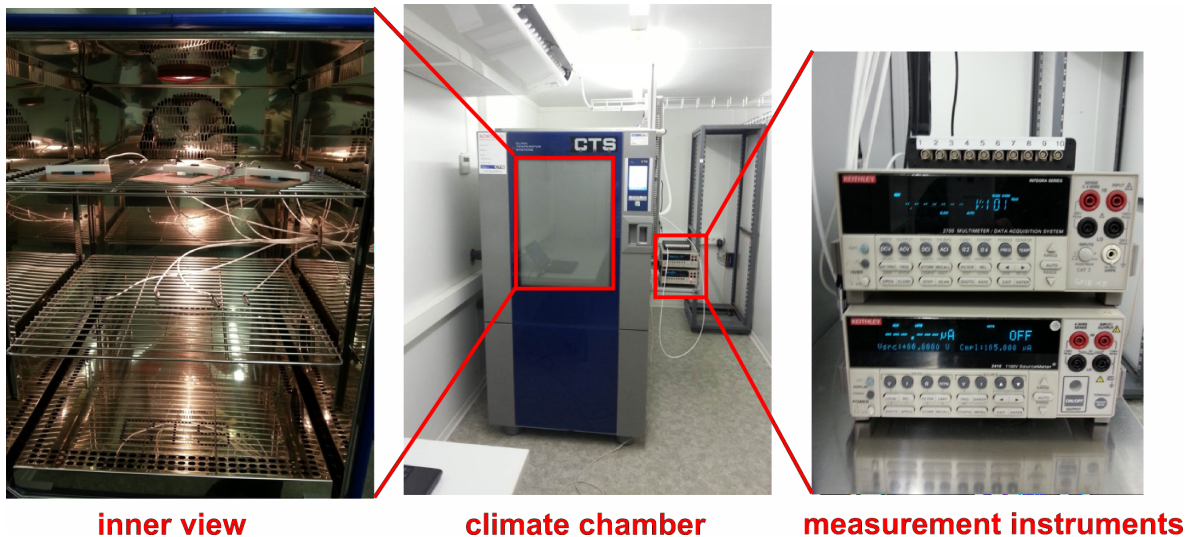


Figure 8.1: Climate chamber setup. Left: Inner view, middle: Whole test setup, right: Electrical measurement instruments.

The climate chamber is placed inside an air-conditioned container since it requires constant ambient temperatures. It is completely light tight if the door is closed which is compulsory for every electrical measurement on silicon strip sensors. The most important operational parameters of the climate chamber are listed in table 8.1. It can be controlled manually via a front panel or with the use of a program interface. Actual test cycles are mostly programmed and implemented via the program interface. Furthermore, the climate chamber can directly be controlled via LabVIEW with the use of a TCP/IP-connection.

In addition to the chamber itself electrical measurement instruments are needed in order to investigate the electrical behaviour of test samples. These measurement instruments are placed beside the chamber. Therewith, the global current-voltage characteristics can be measured for a maximum of 10 sensors at once. In particular, a Keithley 2410 SMU serves as a biasing SMU for all connected sensors. Furthermore, a Keithley 2700 multimeter / switching system is used to measure the global leakage current of every sensor. The voltage application and the

measurement of individual currents is enabled via in series connected resistors (each $470\text{ k}\Omega$) where every resistor corresponds to one test sample. The electrical connection of sensors is ensured via a cable gland at the chamber and temperature resistant cables (similar to coaxial cables).

After the measurement is started the Keithley 2410 increases the voltage up to the initially adjusted bias voltage. Meanwhile, the Keithley 2700 is switching through the different connections and measures the current flowing through the individual resistors. The time interval for every measurement can be adjusted via the LabVIEW software. If the bias voltage is reached, the Keithley 2700 continues the current measurement up to a defined measurement time. Hence, the current-voltage characteristics and the current-humidity or temperature characteristics can be recorded. An initial calibration measurement has to be performed in order to correct the measured current since the current flowing through the shunt resistors is the one which is actually measured.

	Enabled humidity control	Disabled humidity control
Temperature range ($^{\circ}\text{C}$)	min: +10, max: +95	min: -40, max: +180
Temperature deviation (K)	$\leq \pm 0.3$	$\leq \pm 0.3$
Rel. humidity range (% r.H.)	min: 10 max: 98	—
Rel. humidity deviation (% r.H.)	$\leq \pm 3$	—
Maximum temperature changing speed ($^{\circ}\text{C}/\text{min}$)	heating: 3.5, cooling: 4	heating: 3.5, cooling: 4

Table 8.1: Main operational parameters of the climate chamber.

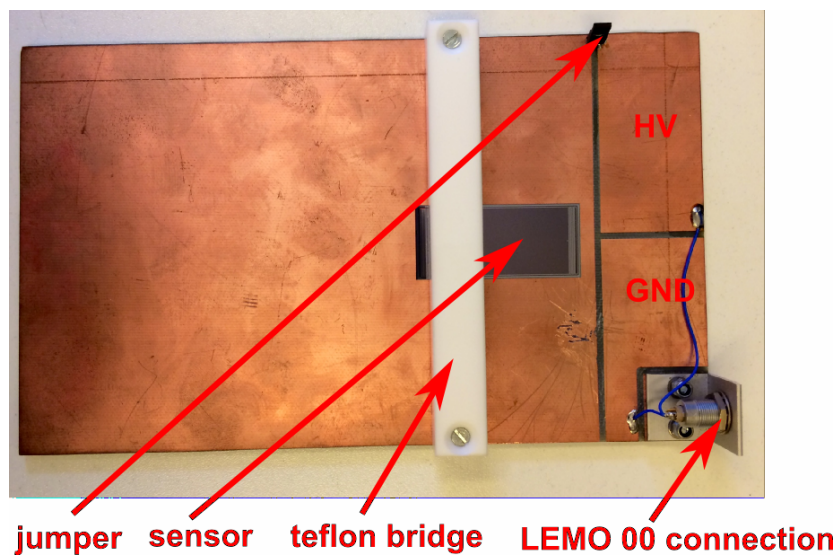


Figure 8.2: Test sample (STS sensor) mounted on a copper board.

Special boards built for environmental stress tests of silicon strip sensors facilitate electrical connections. In particular all test samples are mounted onto copper boards and are fixed by teflon bridges (see figure 8.2). The high voltage (HV) and the ground connections of the LEMO 00 cables are localised at two pads of the board. The HV is applied at the backside of the sample with the use of a jumper. The ground connection is ensured via a wire bond reaching from the bias line to the grounding pad. At present only the global leakage current can be measured with the use of the copper boards. Nevertheless, an extension to further measurement parameters (global capacitance, single strip parameters) is possible due to the adaptable design of the boards. Further sensor parameters are not investigated in this section due to the limited availability of measurement instruments.

8.2 Test Samples

Infineon STS sensors of batch 1 and 2 and small sensors of the vendor which provides the sensors for CMS are used for each investigation. The most important parameters of STS sensors have already been discussed and are summarized in table 4.1. The other types of sensors are equal to those called “S3” which were used for IGFET-like measurements (see table 7.1). They will be denoted as “CMS reference samples” in the following. Both sensors have varying number of strips (i.e. CMS reference samples: 64 and Infineon STS sensors: 256) but a similar active area. This results in similar global leakage currents which is especially important since only one SMU is serving as a voltage source for all sensors. In particular the current compliance of this SMU can be tuned better in case of similar leakage currents. Nevertheless, the active area of STS sensors of Infineon is about twice as much. Because of this it is expected that the global leakage current is larger for those kind of test samples. Absolute values of the global leakage current are anyway not that important since only its dependence of varying temperatures and humidities is investigated.

8.3 Test Cycle with Varying Relative Humidities

At first the dependency of the global leakage current to increasing relative humidities (r.H.) is investigated. The relative humidity states to which percentage the absolute humidity (= mass of water vapor in a defined volume) exploits its maximum value. Contrary to the absolute humidity, the relative humidity is temperature dependent. Hence, it always refers to an ambient temperature. The relative humidity will often be termed as humidity in the following for reasons of simplicity.

In total three CMS reference samples, two STS sensors of batch 1 and one STS sensor of batch 2 are serving as test samples. It has to be ensured that all sensors can be biased with the same voltage and that none shows early breakthroughs before the actual test cycle starts. Therefore, the global IV characteristics of all sensors are measured at first.

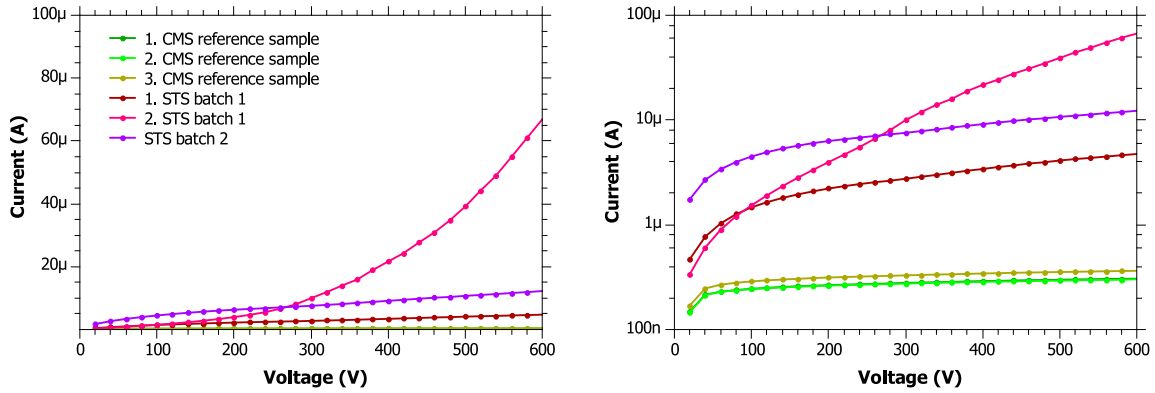


Figure 8.3: Global IV behaviours of all test samples for the intended humidity test cycle. Left: linear y-axis, right: logarithmic y-axis.

As assumed previously CMS reference samples show lower global leakage currents than STS sensors of Infineon (see figure 8.3). Breakthroughs cannot be observed until 600 V expect for the 2. STS sensor of batch 1. According to the measured IV characteristics, the longterm bias voltage is adjusted to 300 V (standard bias voltage for Infineon sensors) for the actual humidity cycle. This voltage should ensure that all test samples are fully depleted. The 2. STS of batch 1 starts already breaking through at 300 V but this should not influence its longterm behaviour concerning varying humidities since its global leakage current is still comparable small.

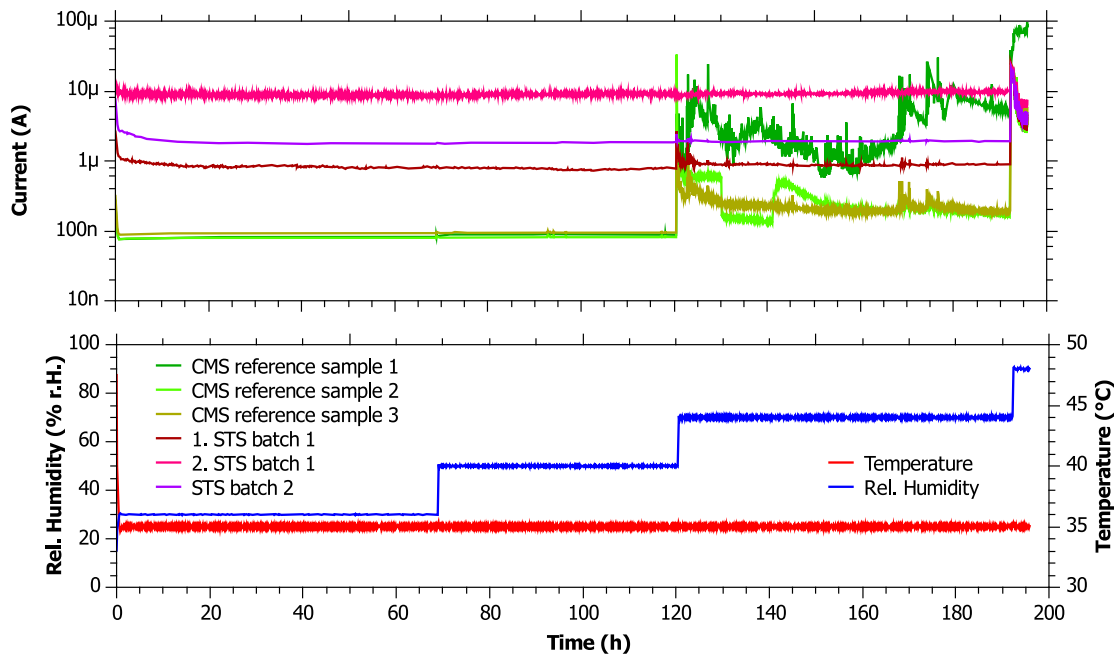


Figure 8.4: Longterm relative humidity cycle. Top: Global leakage current of test samples (logarithmic), bottom: Temperature and relative humidity.

The actual longterm humidity cycle lasts about 200 h (approximately 8 days). The temperature remains constant at 35°C and the humidity is gradually increased from 30 %r.H. to 90 %r.H. in steps of 20 %r.H.. A measurement of the global leakage current is performed every minute.

Figure 8.4 displays the longterm behaviour of the global leakage current for varying humidities of all test samples. All samples show a linear behaviour for humidities of up to 50 %r.H.. Differences of the behaviour of the global leakage current for the two different vendors arise for humidities beyond 50 %r.H.. All CMS reference samples are beginning to show irregularities at 70 %r.H.. Test samples of Infineon on the contrary are still stable at this humidity. All test samples (Infineon and CMS) are beginning to show distinct irregularities at 90 %r.H. This is expected since 90 %r.H. definitely corresponds to an extreme environmental condition which most semiconductor devices would not withstand.

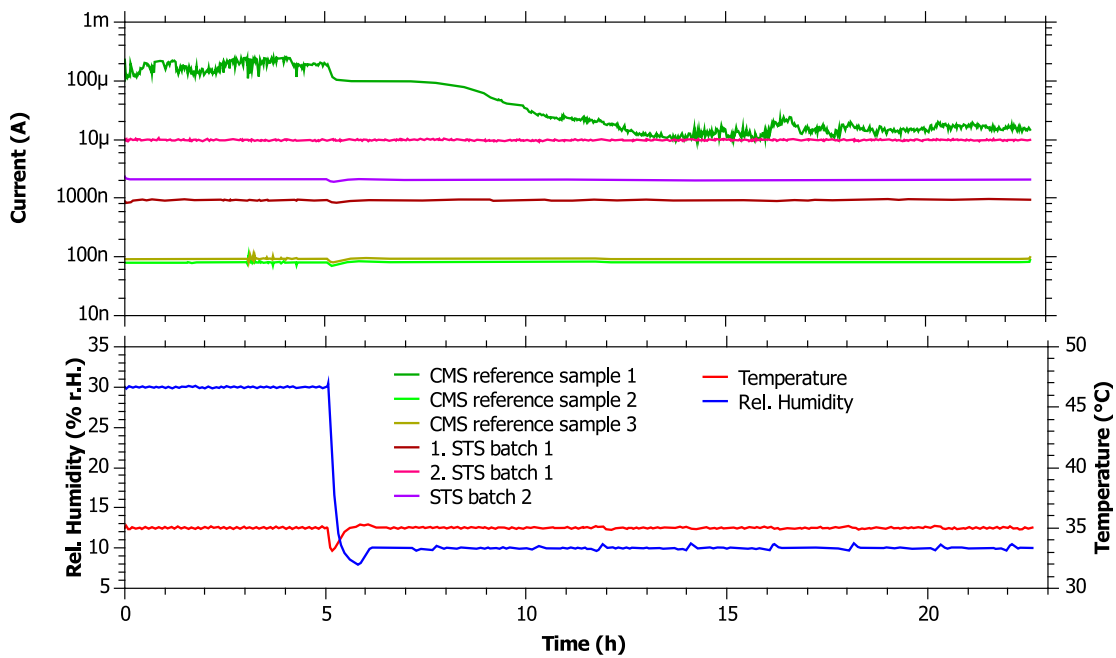


Figure 8.5: Drying procedure of test samples. Top: Global leakage current of test samples (logarithmic), bottom: Temperature and relative humidity.

Right after the longterm humidity cycle, the relative humidity was decreased from 90 %r.H. to 30 %r.H. and after a time span of 5 h to 10 %r.H. (only the decrease from 30 %r.H. to 10 %r.H. was recorded, see figure 8.5). The temperature is still adjusted to 35°C. This procedure is performed in order to remove a probable captured moisture inside or at the passivation layer and can therefore be compared to a drying procedure. It can be observed that the global leakage current of all sensors recovers to their initial value except for the 1. CMS reference sample. This test sample is consequently excluded from further investigations. All other sensors are reutilized for temperature cycles.

8.4 Test Cycle with Varying Temperatures

The temperature dependence of the global leakage current is investigated in order to validate if its behaviour is according to the theoretical predicted one. Deviations from the predicted behaviour would indicate a poor resilience against varying temperatures and moreover would reveal lattice defects inside the silicon bulk material. The latter statement can be made since the leakage current is primarily bulk generated and defects are leading to unexpected additional currents.

As already mentioned the global leakage current $I_0(T)$ of equation 2.10 is temperature dependent and is described by equation 8.1 [20]:

$$I_0(T) \propto T^2 \cdot \exp\left(\frac{-E_g}{2kT}\right) \quad (8.1)$$

where T is the temperature, E_g the band gap of silicon and k the Boltzmann constant. According to equation 8.1, the leakage current doubles for an increase in temperature of 7.5°C . Exponential temperature dependencies should also be observed for the envisaged temperature cycle for samples of both Infineon and CMS.

The test cycle consists out of two cycles where the temperature is increased from 15°C to 65°C and afterwards again decreased to 15°C . These temperature ranges are carefully chosen since the humidity control is only enabled between 10°C and 95°C (see table 8.1). The intention of applying two consecutive temperature cycles is to gain information about the reproducibility of the behaviour of the global leakage current. The temperature changing rate is fixed for every cycle and set to $0.0625^\circ\text{C}/\text{min}$. This constraint results in a total cycling time of about 54 h. This slow temperature changing rate ensures that the test samples are always in a thermodynamic equilibrium. Furthermore, the thermal capacity of the copper boards can be neglected for that slow temperature changing rate. The relative humidity is kept constant over the whole period and is adjusted to 10 % r.H..

The same samples as for the humidity tests are used except for the 1. CMS reference sample. It is assumed that the other test samples are already free from any moisture due to the results gained by the drying procedure (see figure 8.5). All test samples were stored at humidities $< 10\%$ r.H. for about one week in addition to the monitored drying procedure.

Figure 8.6 displays the measurement results of the longterm temperature cycle. The global leakage current of all test samples show an exponential dependency of the temperature (logarithmic current axis). It seems that the global leakage current of all samples has the same value for repeating equal temperatures. Hence, reproducibility seems to be granted. It is also apparent that the global leakage current of the 2. STS of batch 1 is not as heavily influenced by temperature changes as the other tests samples. The applied bias voltage (i.e. 300 V, which is the same as for humidity cycles) and its consequences might offer an explanation therefore. In particular the 2. STS sensor of batch 1 already shows a beginning breakthrough at 300 V

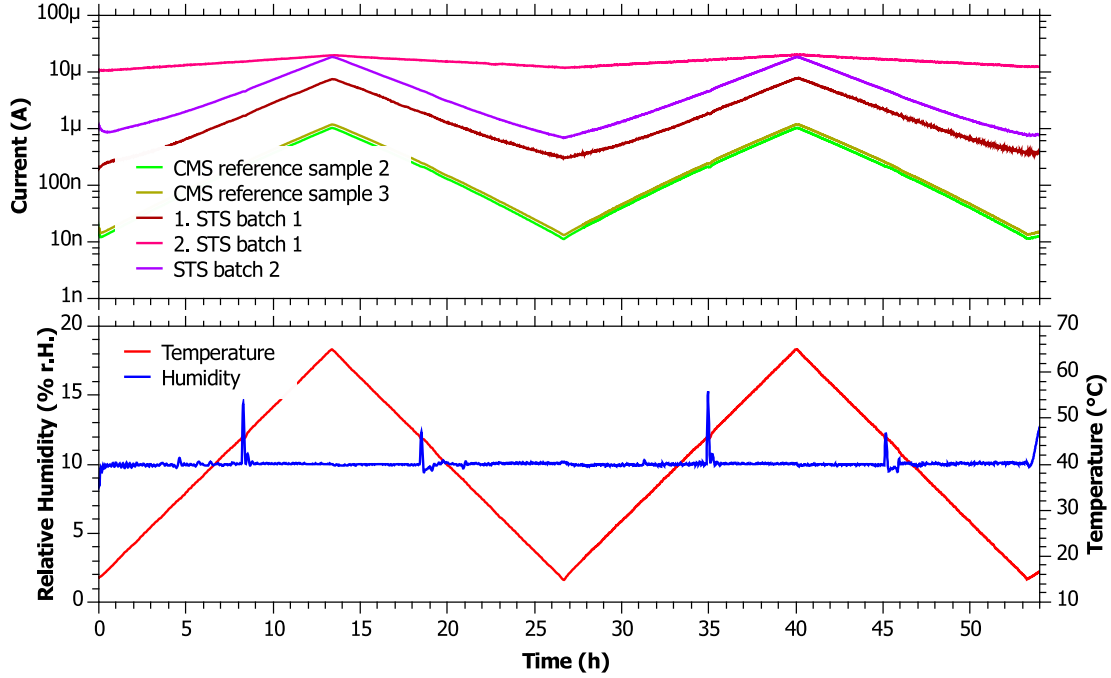


Figure 8.6: Longterm temperature cycle. Top: Global leakage current of test samples (logarithmic), bottom: Temperature and relative humidity.

(see figure 8.3). The current at the breakthrough region cannot be described by equation 8.1 anymore which leads to the observed minor temperature dependence for this sample.

However, the results displayed in figure 8.6 are only indicating that the global leakage current of the test samples behave according to the theory. In order to gain more than just indications the measured currents have to be processed in a different way. Especially Richardson plots (or Arrhenius plots) provide an opportunity therefore [20]. In case of such plots the natural logarithm of the global leakage current is plotted against the inverse of the temperature.

Taking the natural logarithm of equation 8.1 results in equation 8.2 which is equal to a linear function $y = k \cdot x + d$.

$$\ln(I_0(T)) \propto 2 \ln(T) - \frac{E_g}{2kT} \Rightarrow 2k \cdot \ln(I_0(T)) \propto 2 \ln(T) - E_g \cdot \frac{1}{T} \quad (8.2)$$

The slope of the linear function displayed in 8.2 corresponds to the band gap of silicon E_g . It can be obtained by a linear fit if $2k \cdot \ln(I_0(T))$ is plotted against $\frac{1}{T}$ (which very similar to a standard Richardson plot). Such plots can be made for every test sample and are providing a more sophisticated statement if the measured currents are according to the theoretical behaviour. In particular the band gap energy obtained by a linear fit should be about 1.12 eV ($= E_g$ of silicon). Slight deviations from this value are expected since the band gap itself is temperature dependent (see equation 2.2). Furthermore, deviations from straight lines would conclude that currents additional to bulk generated ones are flowing. The fact that two

consecutive temperature cycles were performed provides additional information concerning the reproducibility of measured currents. All test samples experienced every temperature between 15°C and 65° for four times due to the increase and decrease of the temperature and the fact that two consecutive cycles were conducted. In case of the envisaged plots this should result in four straight lines for every tests sample. Reproducibility is now granted if all of these lines coincide which states that the current takes the same value for equal temperatures.

Figure 8.7 displays the Richardson plots for CMS reference samples. The more common representation of $1000/T$ instead of $1/T$ is used for the x-axis. Both samples show straight lines so only bulk generated currents are flowing. Furthermore, all of the four lines coincide for both test samples which states that the measured current is reproducible.

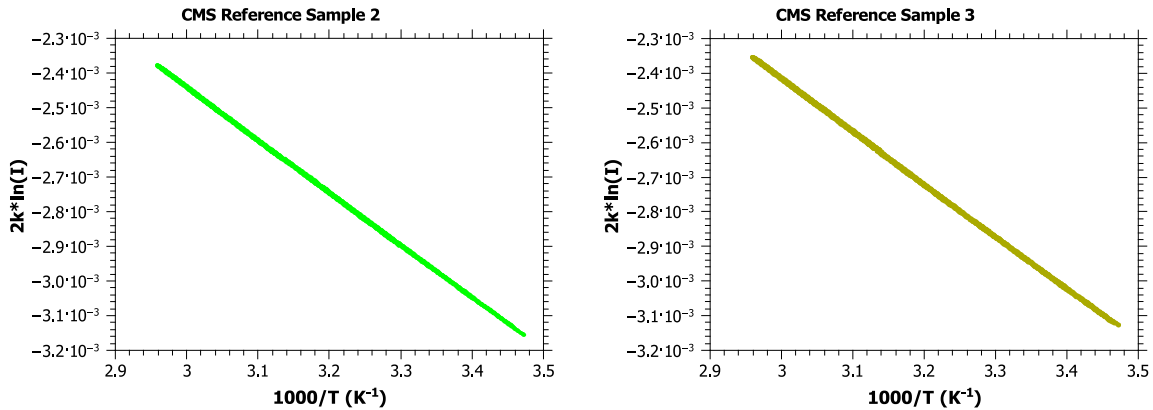


Figure 8.7: Richardson plots for CMS reference samples. Left: CMS reference sample 2, right: CMS reference sample 3.

Figure 8.8 displays the same plots for STS sensors of Infineon. The single lines are not that perfectly overlapping like for CMS reference samples. This indicates that the reproducibility of measured currents at equal temperatures is not granted. The STS sensor of batch 1 is more affected by this issue than the sensor of batch 2. A more detailed analysis of the single lines revealed that the current of the STS sensor of batch 1 is continuously increasing and that this increase is temperature independent. Most likely this sensor is already damaged. Furthermore, both sensors do not show perfect straight lines. So it is assumed that currents additional to bulk generated are flowing. Those currents might be surface currents caused by a still captured moisture coming from the previously performed humidity cycle. Lattice defects are also not excluded which would lead to the same error pattern.

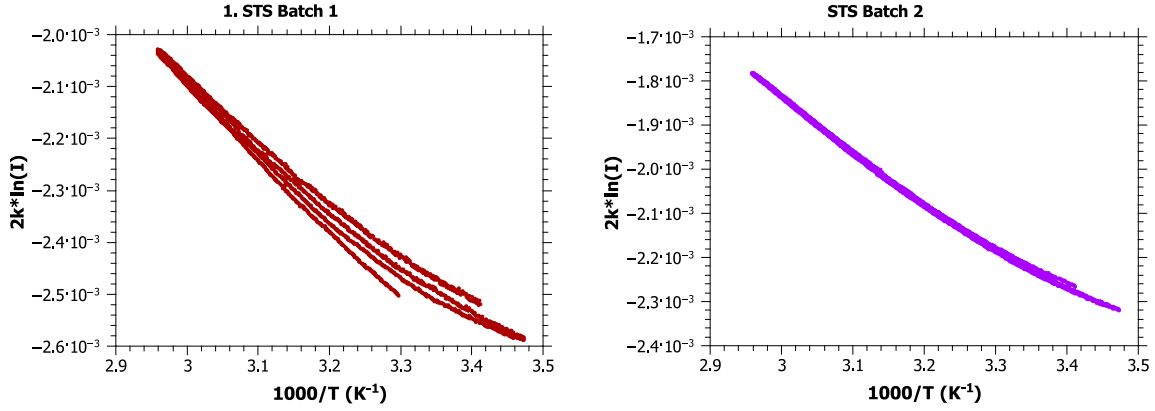


Figure 8.8: Richardson plots for STS sensors of Infineon. Left: 1. STS of batch 1, right: STS of batch 2.

Table 8.2 shows the linear fit parameters of all investigated test samples. Both types of test samples reveal a band gap energy which is close to the theoretical predicted one (i.e. 1.12 eV). However, test samples of Infineon come closer to this value than CMS reference samples but they do have a larger error.

Beside the band gap energy and its uncertainties the coefficient of determination R^2 is listed in table 8.2. It states how well the data of figures 8.7 and 8.8 can be fitted with a linear function. It can take values between 0 and 1 whereat 0 corresponds to no linear relationship and 1 to a perfect coherence of data and fitted model. The coefficient of determination takes a value very close to 1 for all test samples. Nevertheless, CMS reference samples come closer to this value than test samples of Infineon. This is not very surprising since an unperfect linear relationship for Infineon samples could already be observed by their according Richardson plots (see figure 8.8).

	E_g (eV)	ΔE_g (meV)	R^2
1. STS of batch 1	1.129	3.366	0.9754
STS of batch 2	1.089	1.947	0.9991
CMS reference sample 2	1.515	0.361	0.9998
CMS reference sample 3	1.519	0.536	0.9996

Table 8.2: Parameters gained by linear fits of Richardson plots shown in figures 8.7 and 8.8.

8.5 Conclusion

The conducted humidity cycle revealed that test samples of Infineon are even more resilient against high relative humidities (or moisture) than test samples of the vendor which provides the sensors for CMS. The most probable reason for this improved resilience might be the passivation of sensors of Infineon (i.e. silicon nitride: Si_xN_y) which differs from the passivation of sensors currently used in CMS. Silicon nitride is especially known for its qualities as moisture barrier. This makes it one of the standard materials used for the passivation of semiconductor devices. The probable disadvantages of silicon nitride according to static charge dissipation (see section 7.5) are therefore at least partly compensated by the improved resilience against moisture.

The performed temperature cycle revealed that the temperature dependent global leakage current of Infineon test samples cannot fully be described by the theoretical model. First of all it is important to mention that all test samples of Infineon used for investigations in this chapter were not bathed (see section 7.4). Hence, static charges might still be located at the passivation of these sensors. The previous chapter showed that these static charges do have an impact on the single strip parameters. It is furthermore not excluded that also the global leakage current can be influenced by static charges. The same issue causing the defective area of strips might also cause the observed discrepancies concerning the temperature dependence of the global leakage current. Exploring the results in more detail reveals that the STS sensor of batch 2 shows a much more reasonable behaviour than the sensor of batch 1. The fitted band gap energy comes closer to the predicted one and also the reproducibility of measured currents is granted for the sensor of batch 2. The only discrepancy observed for this sensor is that currents additional to the bulk generated ones are flowing which might be caused by a still captured moisture. The sensor of batch 1 on the contrary shows strong deviations from the theoretical predicted behaviour. Reasons therefore might be that this sensor is already damaged by the previously performed humidity cycle or the fact that it still has an unintended layer of photoresist on top of the passivation. This layer might influence the electrical characteristics. All upcoming batches won't have a layer of photoresist so a focus can be placed on the results of the sensor of batch 2.

Generally further statistics are needed in order to give more profound statements concerning humidity and temperature dependence of the global leakage current. Moreover, the longterm behaviour has to be investigated more in detail. Some information about the longterm behaviour although could be gained due to the fact that the humidity cycle was conducted over a relatively long time scale. At least for this time scale all samples of Infineon showed promising results concerning stability of the global leakage current.

9 Neutron Irradiation Studies

Irradiation studies take an important part in the evaluation of silicon strip sensors. They are mainly carried out at nuclear research reactors or accelerator facilities. Both of the facilities are able to provide radiation doses comparable to those which sensors would be exposed over their whole lifetime inside CMS. So every irradiation study can also be seen as an aging study. Results gained from such investigations are especially valuable when it comes to adjustments concerning bulk properties like the resistivity or even the choice of the bulk material type (n-type or p-type) itself. Improvements of single sensor structures or manufacturing techniques can also be deduced. Irradiation studies are especially important at the present time since sensors built for the future CMS tracker phase II upgrade (see section 1.2.2) will have to withstand higher radiation doses with the upcoming upgrade of the LHC, the HL-LHC. An improved irradiation hardness of sensors used for the CMS upgrade is, therefore, compulsory. The resilience of silicon strip sensors against radiation is mainly limited by the properties of silicon itself. Other materials like diamond would provide better radiation hardness but large-scale sensors made out of diamond are too expensive. So far silicon based sensors still provide the best cost-benefit ratio.

The irradiation studies presented in this chapter are the very first concerning structures made by Infineon. They will give insights into the radiation hardness and are decisive when it comes to the qualification of a new vendor. The studies were carried out at the TRIGA Mark II Research Reactor of the Institute of Atomic and Subatomic Physics (Atominstitut, ATI) in Vienna. Instead of actual strip sensors, diodes of Infineon and CMS (= diodes from wafers where the corresponding sensors are currently used in the CMS tracker) were irradiated. The choice of using diodes arises from the fact that the core of the reactor was recently exchanged which results in different fluencies and spectra. So the neutron fluence of the reactor has to be calibrated before irradiation studies can be conducted which is mostly done by the irradiation of diodes. Valuable information on the irradiation hardness of the bulk material could be gained beside reactor calibration although the studies were actually not intended therefore.

9.1 Theoretical Introduction

The change of the electrical properties of silicon strip sensors under irradiation are in detailed described in [21]. This section will only summarise the most important facts which are necessary for a sufficient understanding.

9.1.1 The Non Ionising Energy Loss (NIEL) Scaling Hypothesis

The radiation damage produced inside the silicon bulk material depends on the kind of the incidental particle (charged or neutral), its main interaction and its energy. Charged particles mainly cause ionisations whereas neutral particles mainly induce crystal lattice defects due to elastic scattering. Ionisations are in general fully reversible but interactions with the nuclei of crystal lattice atoms might not. The damages in the crystal lattice can be divided into two groups, i.e. point or cluster defects. Point defects correspond to only one displaced lattice atom. On the contrary cluster defects arise if the recoil energy is high enough so that a single displaced atom can cause further displacement inside the crystal lattice.

The NIEL scaling hypothesis provides a facile way to scale the differently induced damages. In particular, the fluence of any particle Φ can be scaled to the equivalent fluence of 1 MeV neutrons Φ_{eq} which would induce the same damage, i.e.:

$$\Phi_{\text{eq}} = \kappa \cdot \Phi \quad (9.1)$$

[21] where κ is a numerical scaling factor which is also commonly known as the hardness factor. The hardness factor can be expressed with the use of the displacement damage cross section $D(E)$ of an incident particle with energy E which can be calculated according to equation 9.2 [21].

$$D(E) = \sum_j \sigma_j(E) \cdot \int_0^{E_R^{\text{max}}} f_j(E, E_R) P(E_R) dE_R \quad (9.2)$$

In equation 9.2, σ_j is the cross section of one particular interaction process, $f_j(E, E_R)$ is the according probability that the incident particle collides with a crystal lattice atom (i.e.: primary knock-on atom, PKA) with a recoil energy E_R and $P(E_R)$ is the so-called Lindhard partition function which states which fraction of the recoil energy contributes to the displacement of the crystal lattice atom. Along with the energy spectra $\phi(E)$, the hardness factor can be calculated with the use of equation 9.3 [21].

$$\kappa = \frac{\int D(E) \phi(E) dE}{D(E_{\text{Neutron}} = 1 \text{ MeV}) \int \phi(E) dE} \quad (9.3)$$

The following sections and also the measurement results will always refer to the equivalent fluence of 1 MeV neutrons Φ_{eq} . This provides more general statements concerning radiation damages of the silicon bulk material and a better comparability with results gained by other irradiation studies.

9.1.2 Change of the Global Leakage Current Under Irradiation

Both point and cluster defects can occupy energy levels which are located in the middle of the band gap. Generation and recombination of charges are causing currents there which flow

additionally to the ordinary leakage current. The amount of the lattice defects and hence the current increase is depending on the fluence. In particular the difference of the global leakage current after and before irradiation $\Delta I = I_{\text{after, irradiation}} - I_{\text{before, irradiation}}$ can be described by equation 9.4 [21]:

$$\Delta I = \alpha \Phi_{\text{eq}} V \quad (9.4)$$

where V is the volume of the silicon strip sensor or diode and α the current related damage rate. According to equation 9.4 the leakage current increase has a linear dependency on the fluence which is demonstrated in figure 9.1.

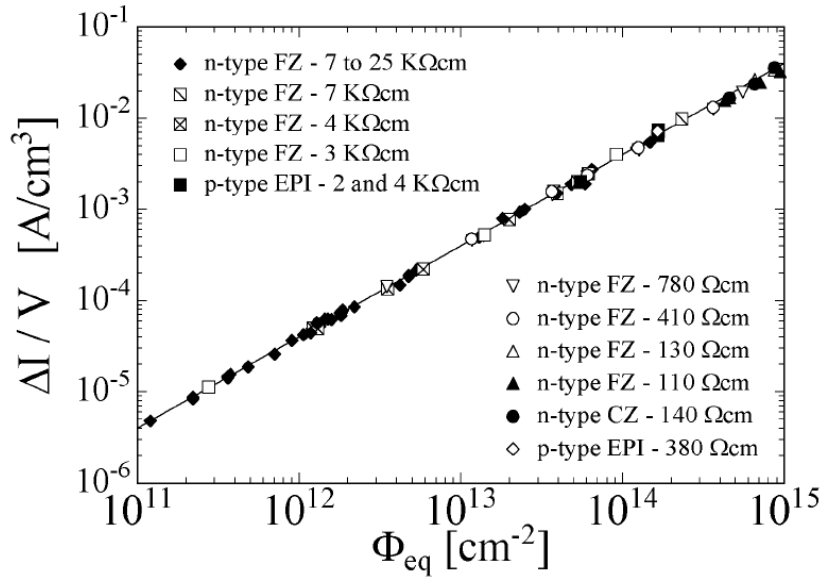


Figure 9.1: Fluence dependence of the leakage current for different types of silicon bulk materials [21].

The current related damage rate α depends on the annealing time and temperature. Annealing of irradiated structures made of silicon is generally an important process since lattice defects can migrate over the whole crystal lattice. This migration can lead to positive but also negative effects. Detailed annealing studies are not presented in the context of this thesis since it would go beyond the scope of the discussion. According to [21] the current related damage rate for different annealing temperatures and times can be calculated with the use of a fitting model (see figure 9.2). However, all irradiated diodes which are discussed in this chapter were annealed for 5 min at 80°C which leads to an current related damage rate of:

$$\alpha(5 \text{ min}, 80^\circ\text{C}) = 4.42 \cdot 10^{-17} \text{ A/cm}. \quad (9.5)$$

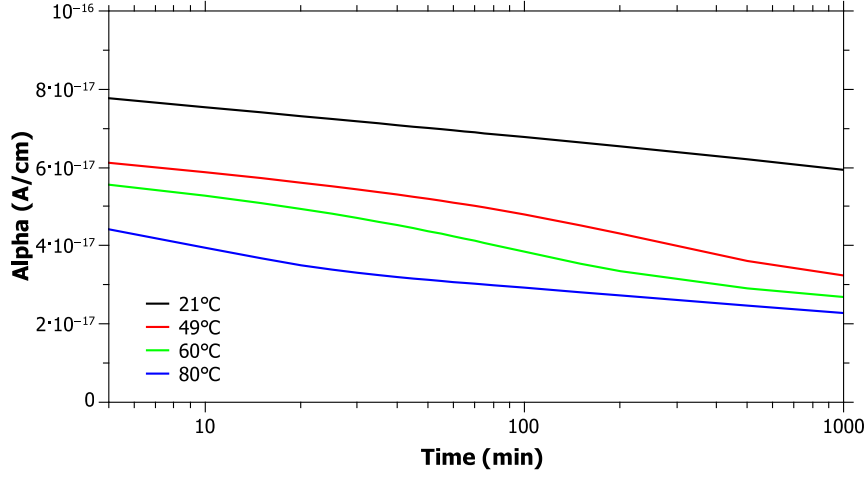


Figure 9.2: Current related damage rate α for various annealing temperatures. The time axis has a logarithmic representation.

9.1.3 Change of the Full depletion Voltage Under Irradiation

As already shown in chapter 2 the full depletion voltage of unirradiated diodes can be calculated by using equation 2.15. The same equation can also be used for irradiated diodes under the constraint that the doping concentration N is replaced by the effective doping concentration $N_{\text{eff}} = N_D - N_A$. This leads to equation 9.6.

$$V_{\text{depl}} \approx \frac{eN_{\text{eff}}d_{\text{max}}^2}{2\varepsilon_0\varepsilon_r} \quad (9.6)$$

The effective doping concentration is used due to the fact that irradiation changes the acceptor and donor concentrations. In particular, donors are removed and moreover the defects itself are acting as additional acceptors. In case of n-type bulk materials ($N_D \gg N_A$) the effective doping concentration and hence the depletion voltage initially decreases with an increasing fluence. This decrease continues until $N_D = N_A$ where the depletion voltage reaches de facto zero. The point at which that happens is also called inversion point. Continuing irradiation beyond this point results in the so called type inversion (i.e. $N_A > N_D$) where the initial n-type bulk material behaves like p-type due to the large number of induced acceptor-like defects. The depletion voltage is now continuously increasing if the absolute value of N_{eff} is considered. The described process is visualised in figure 9.3.

As well as the change of the global leakage current, the change of the depletion voltage and the effective doping concentration does also depend on the applied annealing procedure. This dependency can be neglected since every test sample was annealed for the same time and temperature.

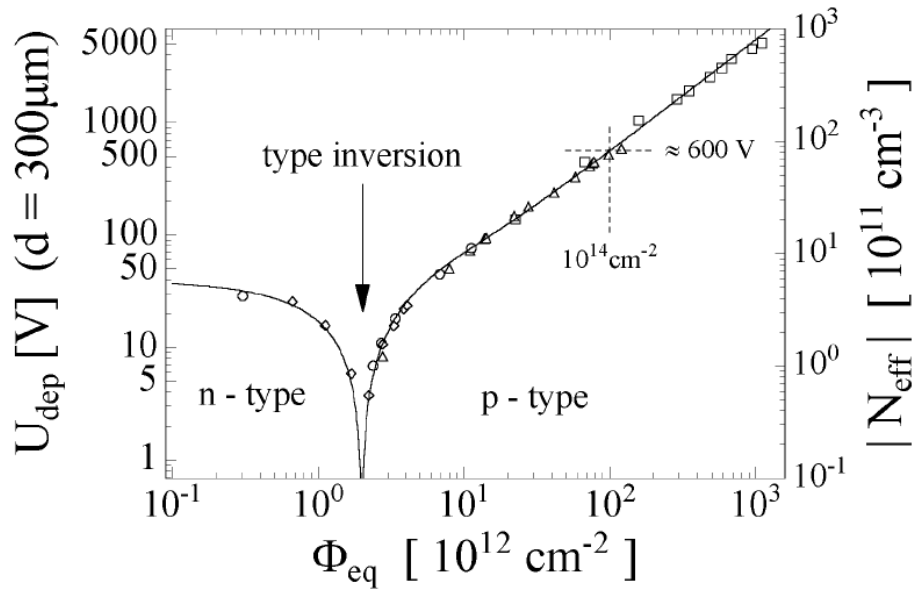


Figure 9.3: Fluence dependance of the full depletion voltage and the effective doping concentration [21].

Plots similar to those shown in figures 9.1 and 9.3 can be used to compare the measurement results gained from irradiated diodes with the according theoretical behaviour which should give insights into the radiation hardness of the bulk material of Infineon sensors. As already mentioned irradiations studies presented in this chapter are primarily intended for reactor calibration purposes. So the equivalent fluences Φ_{eq} are calculated from equation 9.4 and can, therefore, not be used for the mentioned plots. Instead the irradiation time is assigned to the x-axis. Along with the reactor power which is always the same this assignment is strongly related to the equivalent fluence and offers the possibility for the intended comparisons.

9.2 The TRIGA Mark II Reactor at the ATI

The reactor type used for neutron irradiation studies is a TRIGA (= Training-Research-Isotope Production by General Atomics) Mark II which is located at the Institute of Atomic and Subatomic Physics (Atominstitut, ATI) in Vienna. It can reach a thermal power of up to 250 kW in continuous operation mode and 250 MW in pulse mode [22]. The fuel elements contain 8 wt% uranium-235 (20% enrichment), 91 wt% zirconium and 1 wt% hydrogen (wt% = percentage per weight) [22]. The zirconium hydride fuel matrix is responsible for a prompt negative temperature coefficient of reactivity which makes this reactor type inherently safe. Three control rods made out of boron carbide are used as absorber material. These rods can be inserted into the core or retracted which enables the actual adjustment of the reactor power. The core itself is surrounded by water serving as a moderator and cooling liquid. Contrary to most other reactors an opening on top of the reactor allows to view the core right through the water (see figure 9.4).

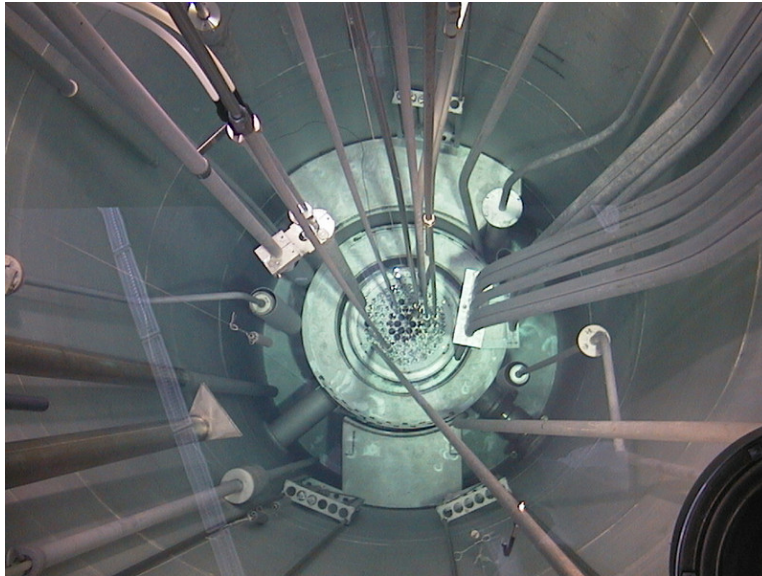


Figure 9.4: Core of the TRIGA Mark II Reactor observed through its surrounding water [22].

Test samples can be irradiated at three different positions close to or even inside the reactor core, i.e.: at the central irradiation tube, at openings between the single fuel elements and at five reflector irradiation tubes. In particular the reflector irradiations tubes are used for studies presented in this thesis due to the fact that they are the only one which are providing a dry environment. Up to five samples at once can be irradiated which results in uncomplicated and fast irradiation runs. All positions provide a 4π neutron flux due to a reflector made out of graphite which is surrounding the core.

In 2012, 91 nearly completely burnt fuel elements were returned to the vendor i.e. the Idaho National Laboratory (INL) [23]. On the other hand, 77 low burned fuel elements from INL were transferred to the ATI in order to keep the reactor operational. The core itself contains 83 fuel elements and is, therefore, nearly completely exchanged by this procedure. Hence, an initial fluence calibration of the new core is compulsory before actual neutron irradiations studies can be performed.

9.3 Tests Samples Used for Neutron Irradiation Studies

9.3.1 Types of Test Samples

Only diodes from Infineon and CMS are used for neutron irradiation studies presented here. Both types of diodes are made out of n-type base material and are similarly structured. The structure itself is very simple and can be compared to the one of silicon strip sensors (see figure 9.5). The essential element is the large scale p-n junction but also the incorporated guard ring has an importance especially when it comes to irradiations. If the guard ring is connected to the same potential as the large p⁺-type region, leakage currents from the edges of the diode

can flow off through the guard ring [21]. This provides more precise measurements of the leakage current arising from the depleted bulk beneath the large p⁺-type region. Hence, more accurate statements concerning the current increase ΔI after irradiation can be made.

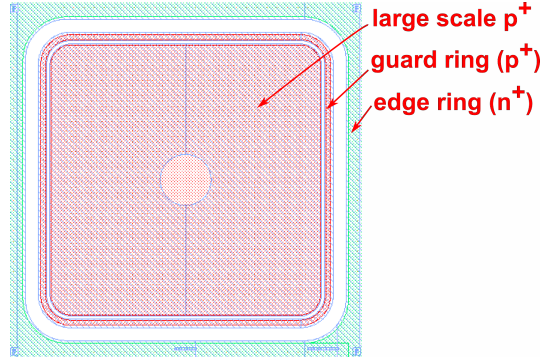


Figure 9.5: Schematic top view of a diode of Infineon.

The dimensions of Infineon and CMS diodes are listed in table 9.2. Both diodes have about the same area but different thicknesses. The resulting differences in the active volume will not have an impact on the current increase ΔI since it scales with the active volume V (see equation 9.4). On the other hand the change of the depletion voltage after irradiation can be affected by different active volumes but more important is the resistivity of the base material. The resistivity of CMS samples is about $4.3 \text{ k}\Omega \text{ cm}$ and the resistivity of Infineon samples is about $2 \text{ k}\Omega \text{ cm}$. Hence it is expected that type inversion occurs earlier for CMS samples.

	Infineon	CMS
Total length (mm)	6.99	7
Total width (mm)	6.99	7
Thickness (μm)	300	500
Active volume (mm^3)	9.41	24.5

Table 9.1: Main parameters of diodes of Infineon and CMS.

9.3.2 Preparation of Test Samples

The radiation damage produced by fast neutrons (i.e. $E_{\text{kin}} \approx 10 \text{ keV} - 20 \text{ MeV}$) is of special interest since the majority of created particles at the interaction point of CMS are high energetic. However, the spectrum of the TRIGA Mark II Reactor is mainly dominated by thermal neutrons (i.e. $E_{\text{kin}} < 100 \text{ meV}$). In order to be able to investigate the radiation damage caused by fast neutrons solely, a cadmium shielding is applied for the half of all diodes of Infineon and CMS. In particular the cadmium isotope ^{113}Cd is responsible for the shielding of diodes.

This isotope is commonly used as a shielding material against thermal neutrons since it has a large cross section at low neutron energies and only a very small one at high neutron energies (see figure 9.6). Hence, almost only fast neutrons can pass through the shielding.

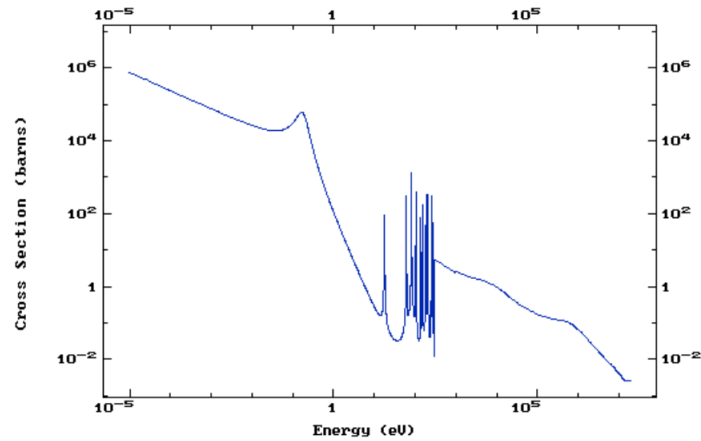


Figure 9.6: Cross section of ^{113}Cd for different energies of incident neutrons [24].

In total, 16 diodes of each type (i.e. Infineon and CMS) are used for the intended irradiation studies. Four diodes (two of each type) are packed at once into a plastic coating which is in turn inserted into a plastic tube used for irradiations. Those tubes can then be inserted into the reactor via the reflector tubes. In particular two diodes (one of Infineon and one of CMS) are packed together and shielded with cadmium plates whereas the other two remain unshielded. For the packaging itself cling film, adhesive tape and plastic sleeves are used (see figure 9.7).

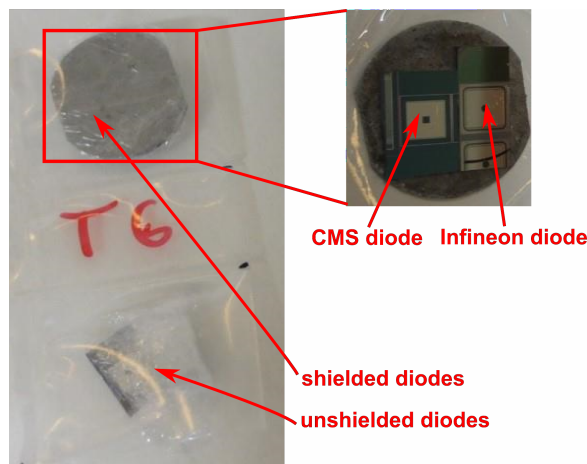


Figure 9.7: Packaging of diodes. Left: Plastic coating with embedded diodes which will be inserted into the tubes used for irradiations, right: Diodes shielded with cadmium.

9.4 Irradiation Procedure and Electrical Evaluation

9.4.1 Irradiation Procedure

Diode no.	Type	Cadmium shielding	Irradiation time (hh:mm:ss)
01	CMS	✓	00:04:06
02	Infineon	✓	00:04:06
03	CMS	×	00:04:06
04	Infineon	×	00:04:06
05	CMS	✓	00:07:23
06	Infineon	✓	00:07:23
07	CMS	×	00:07:23
08	Infineon	×	00:07:23
09	CMS	✓	00:08:14
10	Infineon	✓	00:08:14
11	CMS	×	00:08:14
12	Infineon	×	00:08:14
13	CMS	✓	00:24:44
14	Infineon	✓	00:24:44
15	CMS	×	00:24:44
16	Infineon	×	00:24:44
17	CMS	✓	00:41:12
18	Infineon	✓	00:41:12
19	CMS	×	00:41:12
20	Infineon	×	00:41:12
21	CMS	✓	01:05:56
22	Infineon	✓	01:05:56
23	CMS	×	01:05:56
24	Infineon	×	01:05:56
25	CMS	✓	01:14:10
26	Infineon	✓	01:14:10
27	CMS	×	01:14:10
28	Infineon	×	01:14:10
29	CMS	✓	01:22:24
30	Infineon	✓	01:22:24
31	CMS	×	01:22:24
32	Infineon	×	01:22:24

Table 9.2: Irradiation times and shielding information of all irradiated diodes.

Each tube with its 4 diodes is irradiated for a specific time, ranging from about 4 min to more than one hour. The reactor power is kept constant at 100 kW for every irradiation step. Table 9.2 summarises the irradiation time of every diode and provides information about cadmium shielding. In addition to the 32 diodes listed in table 9.2, one diode of Infineon and one of CMS are serving as reference samples, thus remain unirradiated. These diodes are stored and handled like it is done for the irradiated ones.

The irradiation procedure itself is straightforward. At the beginning of each irradiation step the reactor power is adjusted to 100 kW by a partial retraction of the control rods. First the tubes which are intended to be irradiated for the longest time are inserted, successively followed by the shorter period ones, according to the calculated irradiation time of table 9.2. After the longest period was elapsed the reactor is shut down by a complete insertion of all three control rods. The still packaged diodes are subsequently afterwards put into a freezer in order to prevent annealing. Generally all diodes are kept below 0°C at any time (except at the irradiation itself) for this reason. In total two runs have to be conducted since only five reflector tubes are available. The irradiated diodes, the cadmium and the packaging itself are generally highly activated after the irradiation procedure. Hence, all diodes have to be stored in the freezer at the ATI for about three weeks before their electrical characteristics can be measured at HEPHY.

9.4.2 Electrical Measurements

All of the electrical measurements are conducted at the PQC setup since it provides a vacuum support which can be cooled or heated with the use of a Peltier-Element (see section 5.2). Cooling of diodes is especially important since it prevents unintended annealing and furthermore results in lower leakage currents. This is especially important for already irradiated diodes which generally show higher leakage currents due to the induced crystal lattice defects. The only feasible measurements of diodes are IV and CV characteristics from which plots like the one shown in figure 9.1 and 9.3 can be deduced. The p⁺-type region and the bias ring are connected to the same potential (i.e. ground) for every measurement in order to have a better defined active volume.

At first the IV and CV characteristics of every diode are measured before the irradiation is conducted in order to verify that all selected diodes show reasonable behaviours and are not already damaged. For the initial measurements, the diodes are placed onto the vacuum support which is cooled to -20°C by the Peltier-Element. It is assumed that the diodes have the same temperature as the chuck in a short period of time. The annealing procedure is also carried out with the use of the Peltier-Element along with its heating capability. The temperature is therefore adjusted to 80°C and the irradiated diodes are placed via a copper plate onto the heated vacuum support. The annealing time for all diodes is 5 min. Subsequently after the annealing procedure, all diodes are put back into the freezer and the vacuum support is again cooled to -20°C. As soon this temperature is reached, all already irradiated and annealed diodes are placed back onto the vacuum support in order to remeasure the IV and CV characteristics.

9.5 Measurement Results

9.5.1 Current-Voltage Characteristics After Irradiation

The leakage current of each diode is measured up to voltages of 1 kV before and after irradiation. All of them show reasonable results before irradiation so only the characteristics of already irradiated ones will be discussed and presented in the following.

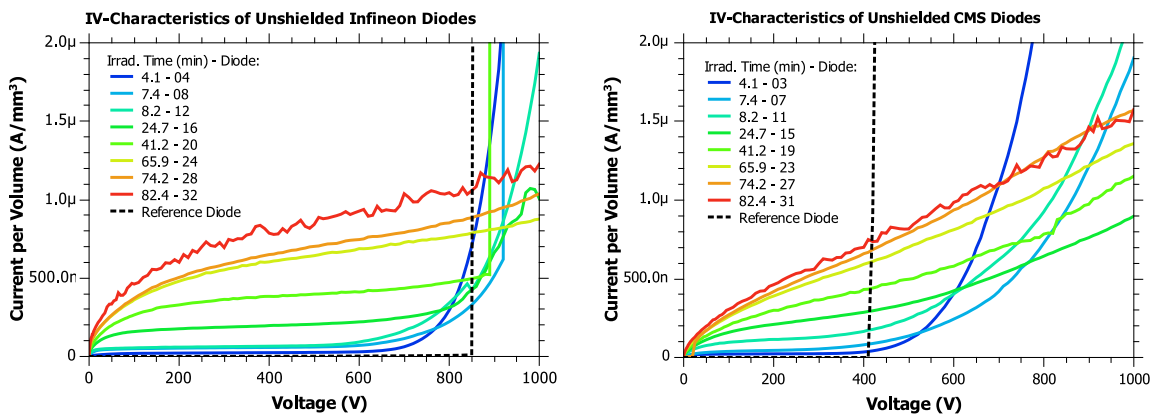


Figure 9.8: IV characteristics of neutron irradiated unshielded diodes of Infineon and CMS.

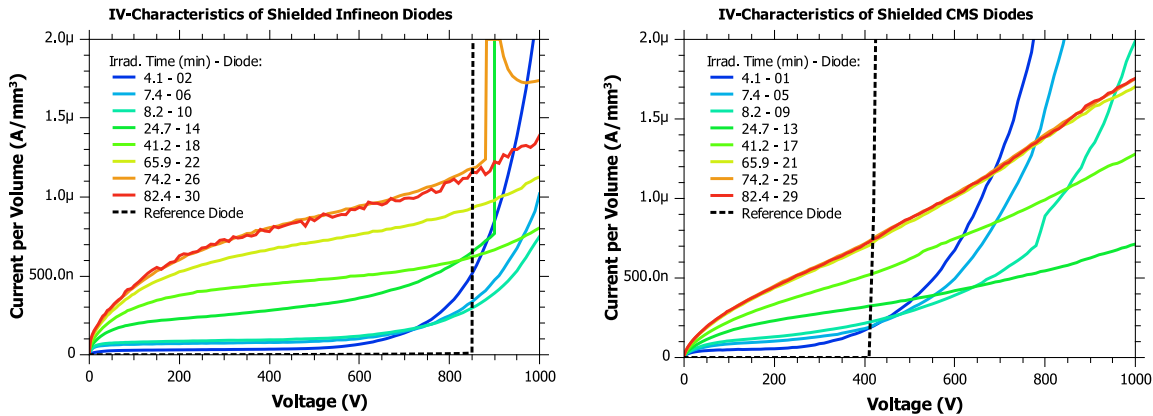


Figure 9.9: IV characteristics of neutron irradiated shielded diodes of Infineon and CMS.

Figure 9.8 displays the measurement results of unshielded diodes of Infineon and CMS. At first it is apparent that breakthroughs occur earlier for diodes of CMS (at least for irradiation times up to 24.7 min). Most likely the design of the aluminum structures is responsible therefor. The guard ring and the large aluminium pad show more distinct edges than displayed in figure 9.5 (= design of an Infineon diode) which eventually leads to electrical field peaks causing early breakthroughs. This behaviour could already be observed for unirradiated diodes thus bears no relationship to the irradiation itself.

The effect of the irradiation expresses in the same way for both types of diodes. In particular the leakage current increases for increasing irradiation times which refer to increasing fluences as it is predicted by theory. Furthermore, the breakthrough voltages tend to higher values for increasing irradiation time. This is especially observable for diodes of CMS where no breakthroughs are visible anymore for those which were irradiated for more than 8.2 min. In addition the IV characteristics of diodes of Infineon are more comparable to the one of unirradiated ones. Diodes of CMS on the contrary behave more and more linear for increasing irradiation times. This could already indicate that diodes of Infineon are more radiation hard than those of CMS. However, both types of diodes which were irradiated for the longest time (i.e. 82.4 min) do not show smooth curves anymore which leads to the assumption that these are already heavily damaged by the irradiation procedure.

Figure 9.9 displays the IV characteristics of cadmium shielded diodes of Infineon and CMS. Their characteristics are very similar to those which were already observed for the unshielded ones. These diodes however show slightly larger leakage currents than the unshielded ones which were irradiated for the same times (see figure 9.10).

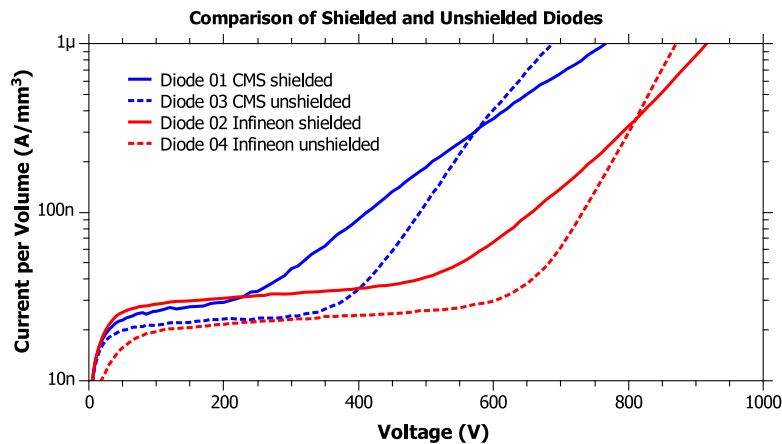


Figure 9.10: Comparison of selected shielded and unshielded diodes. All displayed diodes were irradiated for 4.1 min.

This observation is remarkable since cadmium shielding should prevent radiation damage caused by thermal neutrons. On the contrary shielded diodes seem to be even more damaged by the irradiation procedure. The observed discrepancies concerning cadmium shielding are most likely caused by the neutron capture process of the cadmium isotope ^{113}Cd . In particular, the isotope gets excited if it captures a neutron and decays into the unexcited by emitting a high energetic photon ($E_\gamma \approx 5 \text{ MeV}$) [24]. These photons could cause larger damages inside the crystal lattice than thermal neutrons which results in current increases larger than the normally expected ones.

9.5.2 Capacitance-Voltage Characteristics After Irradiation

The capacitances of all irradiated diodes are measured for voltages of up to 700 V. Only the results of the irradiated diodes are discussed and presented since all unirradiated ones show the same CV characteristics. In particular diodes of CMS are already fully depleted at about 150 V whereas diodes of Infineon are fully depleted at 195 V before irradiation. The capacitance at full depletion voltage of CMS diodes is smaller than for Infineon ones due to the fact that they are 60% thicker.

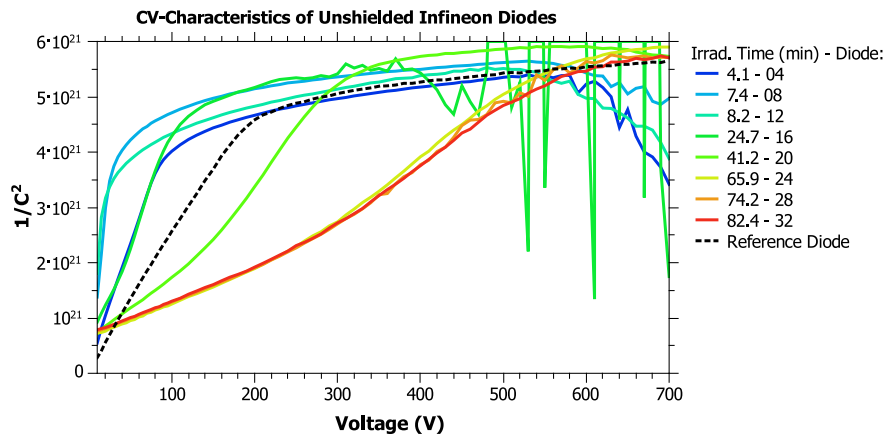


Figure 9.11: CV characteristics of neutron irradiated unshielded diodes of Infineon.

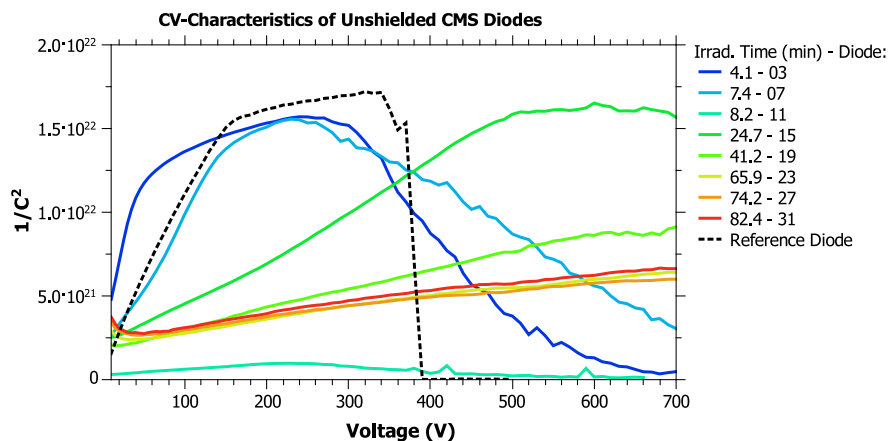


Figure 9.12: CV characteristics of neutron irradiated unshielded diodes of CMS.

Figures 9.11 and 9.12 display the measurement results after irradiation of unshielded diodes of Infineon and CMS. No completely flat plateaus are reached after the initial increase of $1/C^2$ (i.e. after the knee). This hinders the calculation of the full depletion voltage where the curve is fitted before and after the knee by two linear functions. The intersection of the fitted lines then corresponds to the full depletion voltage. This procedure however assumes that a flat plateau after the knee is present which states that the diode is fully depleted. Hence, only rough estimations can be made. This effect gets even worse for highly irradiated diodes which do not even show a distinct knee anymore.

It can be observed that diodes of Infineon show an initial decrease of the full depletion voltage up to irradiation times of 7.4 min whereas it continuously increases afterwards. This is according to the theoretical predicted behaviour which can be seen in figure 9.3. On the contrary diodes of CMS only show continuously increasing full depletion voltages. Hence, these diodes could already be type inverted after 4.1 minutes of irradiation. This assumption is indeed plausible since diodes of CMS have a higher resistivity (i.e. smaller doping concentration) than those of Infineon which consequently results in an earlier type inversion. Generally, partial strong variations of the measured capacitance can be observed (in particular for diode 16 of Infineon) and might indicate that all diodes are already fairly heavily damaged by the neutron irradiation.

Figures 9.13 and 9.14 display the CV characteristics of shielded diodes of Infineon and CMS after irradiation. This time it is not that obvious that shielded diodes are more damaged than unshielded ones like it can be observed in case of the IV characteristics. The comparison of diodes 14 (shielded) and 16 (unshielded) of Infineon which were irradiated for 24.7 min indicate that shielded diodes are more damaged than unshielded ones. The indication arises from the fact that the shielded diode 14 has a larger full depletion voltage than the unshielded diode 16 (both are already type inverted).

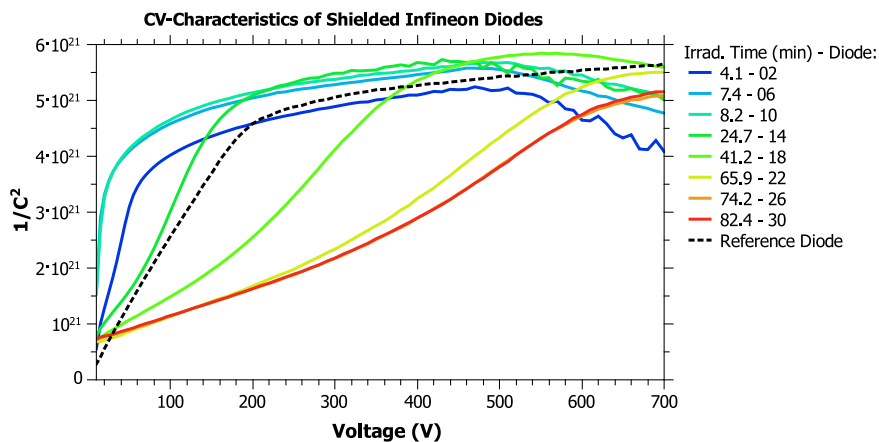


Figure 9.13: CV-characteristics of neutron irradiated unshielded diodes of Infineon.

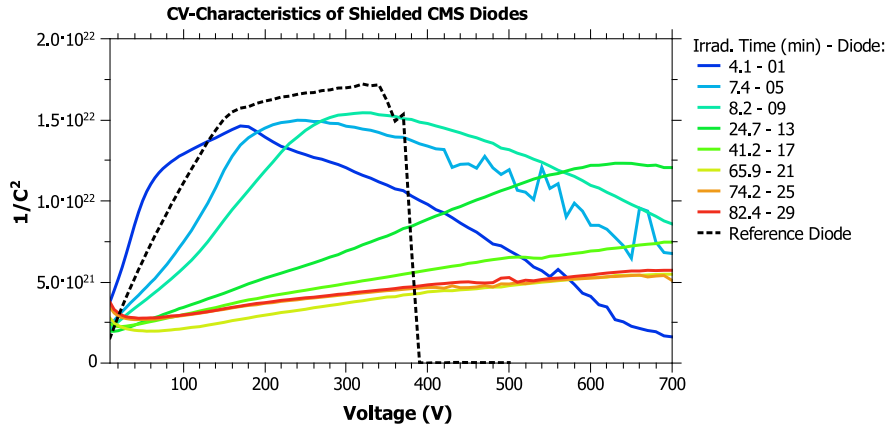


Figure 9.14: CV-characteristics of neutron irradiated unshielded diodes of CMS.

9.5.3 Results Correlated to the Irradiation Time and Fluence Calibration

The insights gained by the evaluation of the IV and CV characteristics can be processed in a similar way to plots shown in figures 9.1 and 9.3. This way of data processing should give more profound statements concerning the change of characteristics under neutron irradiation. The main purpose of the performed irradiation study is of course the fluence calibration of the TRIGA reactor wherefore it can only be referred to irradiation times instead of fluencies.

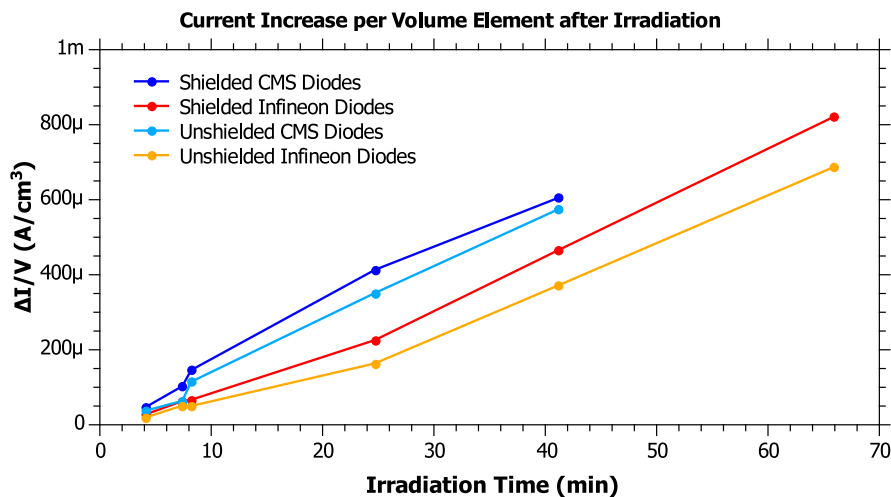


Figure 9.15: Current increase per volume element vs. irradiation time for shielded and unshielded diodes of Infineon and CMS.

Figure 9.15 displays the current increase ΔI of shielded and unshielded diodes of Infineon and CMS for various irradiations times. The currents needed to calculate ΔI refer to the currents measured at the full depletion voltage before and after irradiation. The small amount of

displayed data is accompanied by the limited availability of full depletion voltages for large irradiation times. In particular the full depletion voltages could only be calculated up to irradiation times of 65.9 min for diodes of Infineon and 41.2 min for diodes of CMS. The missing distinct knee of CV curves leads in addition to large uncertainties. Both types of diodes show linear curves with nearly equal slopes which correspond to the predictions shown in figure 9.1. However, it can be observed that the curves of diodes of CMS lie above the curves of Infineon ones. This is contrary to theoretical behaviour according to [21] (figure 9.1) where all data points should be located at a single line independently of the resistivity and the bulk material. Most likely the calculation of the the active volume is inaccurate which could lead to the observable behaviour. The previously made assumption that shielding causes even higher damages manifests also in figure 9.15 where all curves of shielded diodes lie above the curves of unshielded ones. Hence, shielded diodes experienced different (i.e. higher) fluences than unshielded ones.

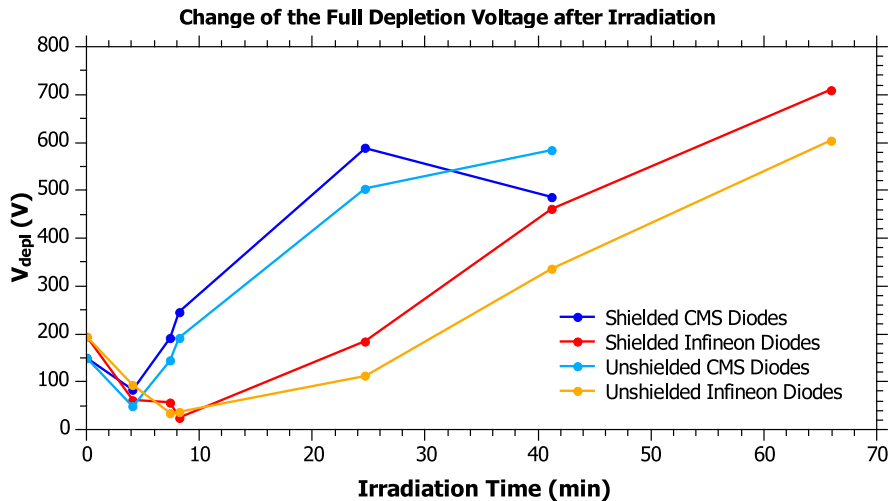


Figure 9.16: Full depletion voltage vs. irradiation time for shielded and unshielded diodes of Infineon and CMS.

Figure 9.16 displays the full depletion voltage of shielded and unshielded diodes of Infineon and CMS for various irradiation times. All displayed curves are similar to the one shown in figure 9.3 which states that the behaviour is according to the theory. The type inversion is for both types of diodes visible by means of an initial decrease of the full depletion voltage which is followed by an increase after the inversion point. More data points could be gained for diodes of Infineon which leads to a better visibility of the initial decrease of the full depletion voltage. Diodes of CMS on the contrary are already type inverted after 4.1 minutes of irradiation (= smallest time scale). The point where type inversion occurs does only depend on the initial doping concentration so no statements about radiation hardness can be made here. Nearly all data points of shielded diodes lie above the unshielded ones. This encourages the suspicion expressed at the discussion of the CV characteristics that shielded diodes are more damaged

than unshielded ones since both were irradiated for the same times.

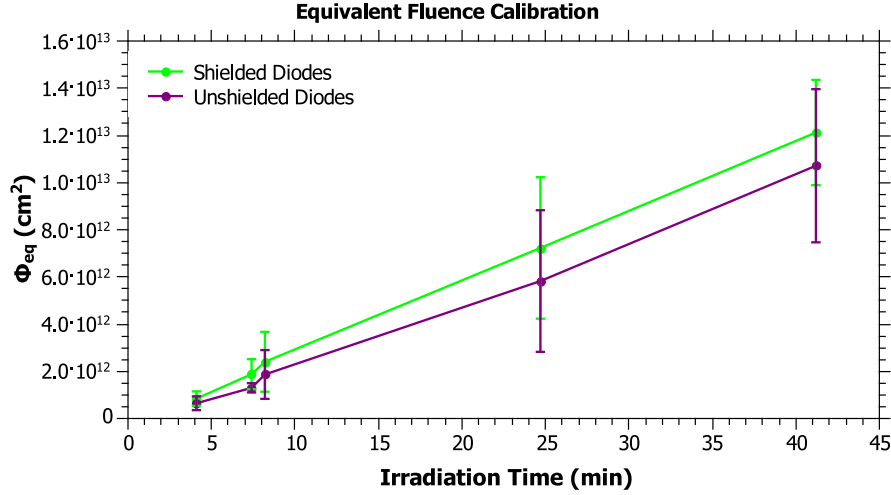


Figure 9.17: Calibration of the equivalent fluence of the TRIGA reactor at the ATI.

Figure 9.17 displays curves which are used for the calibration of the equivalent fluence of the TRIGA Mark II Reactor at the ATI. There Φ_{eq} is plotted against the irradiation time for shielded and unshielded diodes of both vendors. In particular, the average of Φ_{eq} gained by diodes of both vendors is plotted. The error bars correspond to the standard deviation. These calibration curves are only valid for a reactor power of 100 kW. New information on radiation hardness can not be gained from this plot since already processed data is taken therefor. The calculation of Φ_{eq} i.e.:

$$\Phi_{eq} = \frac{\Delta I}{\alpha V} \quad (9.7)$$

with $\alpha = 4.42 \cdot 10^{-17}$ A/cm leads to the above made statement because Φ_{eq} depends on the current increase ΔI which is already displayed in figure 9.1. Figure 9.17 is especially important for future irradiation studies since irradiation times can now be directly linked to an equivalent fluence.

9.6 Conclusion

Valuable information about the change of bulk properties caused by neutron irradiation could be gained although only diodes were irradiated. The presented results revealed that the bulk material of Infineon is at least as radiation hard as the one currently used in CMS. The intended reactor calibration could only be realised partly since all diodes are already heavily damaged for irradiation times lasting more than one hour. A second calibration run with narrower time

intervals is therefore compulsory. The information gained by this additional calibration run will also provide deeper insights into the radiation hardness of the bulk material of Infineon.

A possible way to gain more information out of highly irradiated diodes would be a remeasurement of the IV and CV characteristics without a connected guard ring. This measurement configuration will most likely prevent early breakthroughs and thus provide a better evaluation of the current increase and the depletion voltage for large irradiation times.

The unexpected effects of cadmium shielding have to be investigated in more detail for future irradiation runs. The removal of the cadmium plates directly after the irradiation procedure would provide insights if the emitted high energetic photons are causing the observed additional bulk damage or not. However, a sufficiently large half-life would be mandatory which actually might not be the case according to [24]. This intention will be anyhow very challenging since cadmium plates, packaging material and diodes are highly activated right after the irradiation. A measurement of the radiation of still packed and shielded samples would provide another way of validation (again if the half-life would be sufficiently long). All samples will therefor be put into a 4π detector right after the irradiation procedure. Cooling of samples during this measurement will be anyhow very challenging.

The next step will be the irradiation of STI sensors which should provide deeper insights into the radiation hardness of single sensor structures. A second calibration run and a detailed analysis are inescapable.

10 Summary and Outlook

Investigations which have been performed in the context of this thesis confirmed that also the second batch of silicon strip sensors manufactured by Infineon Technologies Austria AG are generally of high quality. The broad variety of investigations and comparison to other vendors revealed that Infineon is a competitive vendor for sensors used for the CMS tracker upgrade. New insights into the area of defective strips could be gained which will most likely lead to error free sensors in future delivered batches. Aging studies like environmental stress tests and irradiation studies have been conducted for the first time for sensors and test structures manufactured by Infineon. Those studies revealed promising results concerning radiation hardness and resilience against environmental influences. All of the results and perceptions which have been gained during the conducted investigations represent valuable information for possible improvements concerning both sensor layout and manufacturing processes.

The issue of the area of defective strips has been approached very extensively in order to completely resolve it. A mechanism which is most likely causing the defective area has been presented which is highly important for the physical understanding and moreover constitutes a basis for further investigations. The formation of defective strips by the use of externally applied charges assured the made assumptions. It could also be ascertained that the sawing procedure of wafers is responsible for the initial occurrence of the defective area. It turned out that the method of CO₂ bubbling during wafer sawing at Infineon provides an inexpensive and simple way to resolve this issue. Moreover, it could be demonstrated that already affected sensors can completely be restored by a bathing procedure. It is still questionable however why defective strips reoccur. The comparatively high resistivity of the passivation of sensors of Infineon might hinder the dissipation of applied surface charges during measurements at HEPHY which effectively leads to the area of defective strips.

Infineon and HEPHY have already drawn consequences from the presented results. HEPHY will extensively improve the ESD safety of their clean rooms in order to prevent the application of static surface charges. Infineon on the contrary makes a large effort to investigate resistivity concerns of the passivation layer. In particular they will deliver several additional prototype wafers with different passivation materials having partial lower resistivities. An additional consequence will be design changes of prototype sensors. A connection of the passivation layer to the bias line is planned which should lead to a better charge dissipation behaviour.

The presented aging studies concerning environmental stress tests and radiation studies revealed that test structures of Infineon are at least as durable and resilient as those of the major vendor of strip sensors for CMS. The resilience against high relative humidities is even better for sensors of Infineon. The temperature dependence of the global leakage current on

the contrary has to be investigated in more detail. It cannot be excluded that the same issue causing the defective area of strips is also responsible for the observed discrepancies concerning the temperature dependence of the global leakage current.

Results gained by irradiation studies indicate that the bulk material of diodes of Infineon is at least as radiation hard as the one which is currently used for sensors inside CMS. More statistics are however needed in order to validate this indication. The irradiation of sensors is still pending and will provide more insights into the radiation hardness of single sensor structures like the coupling oxide.

The CMS collaboration recently decided that all sensors used for the CMS upgrade will have n-type strips implanted in p-type bulk material instead of the currently used configuration. The change of the bulk material to p-type will provide a better durability of sensors which will be exposed to radiation doses higher than ever before after the LHC upgrade. In particular no type inversion can happen anymore. Moreover new sensors geometries accompanied with a larger wafer diameter are discussed. The most favoured sensors at present are n-on-p sensors which are very similar to the SX2 processed on 200 μm thin 8 inch wafers.

It seems now that investigations concerning p-on-n sensors are dispensable. This impression is deceptive when it comes to the evaluation of a new vendor like Infineon. As a first step it has anyway to be ensured that current state of the art sensors can be processed in a good quality. Infineon will, therefore, deliver a final batch of p-on-n sensors with major design differences which will most likely resolve the issue of defective strips. A lot of effort is already made for n-on-p sensors. Process techniques are currently investigated at Infineon and the wafer design is nearly completely finished by HEPHY. At the moment everything is pointing towards an early production start of world's first n-on-p silicon strip sensors produced on 200 μm thin 8 inch wafers.

Acknowledgments

First of all I would like to thank my supervisor Manfred Krammer who aroused my interest in the field of particle detectors and giving me the opportunity to work in a great scientific environment.

I want to thank Thomas Bergauer for supporting me during my whole time at HEPHY. He encouraged me at anytime and showed me new approaches for sometimes unexpectedly difficult measurements. I am very thankful for his patience during discussions and for his confidence in me. Furthermore, I want to thank him for the strong involvement in the topic and the different responsibilities which gave me unforgettable insights and improved my professional skills.

Many thanks are owed to Johannes Hacker who showed me the industrial point of view. His kind introduction into the world of semiconductor fabrication boosted my decision to work on this topic. He gave me unique insights which offered me another point of view and expanded my horizon. I appreciate very much his professional but also friendly way during every discussion. He always gave me the feeling of appreciation which created a comfortable work atmosphere. Thanks a lot for all your effort!

Special thanks to Wolfgang Treberspurg who accompanied a lot of the conducted investigations and taught me how to perform a large variety of electrical measurements. He is not only a valuable colleague but also a friend. I would have never been able to finish this thesis without his help. Thank you!

I also want to thank Marko Dragicevic who offered me the possibility to participate in a large-scale experiment like CMS and gave me insights into the scientific tasks of a CMS collaborator. I will never forget the CERN visits and the talk in front of the CMS tracker community.

Gratitude is also owed to Ulf Bartl and Thomas Wübben. Their expertise in the technical matters of semiconductor production is very valuable for the whole project especially when it comes to unexpected problems.

Furthermore, I want to thank Mario Villa who accompanied every irradiation run at the ATI. His unbureaucratic way enabled fast and uncomplicated irradiation studies.

Of course I want to thank my parents who supported me during my whole studies. They always ensured my financial safety and provided the best framework conditions for successful studies. The thesis itself is dedicated to my girlfriend Jennifer. She always encouraged me since the beginning of my studies and beyond. The loving support she gave me is largely responsible for all I have ever achieved. Danke!

Bibliography

- [1] The LHC Collaboration; <http://www.lhc-facts.ch/index.php?page=parameter>, 07.2014.
- [2] The CMS Collaboration; <http://cms.web.cern.ch/news/detector-overview>, 07.2014.
- [3] The CMS Collaboration et al.; “The CMS Experiment at the CERN LHC”, *Journal of Instrumentation* 3 S08004, 2008.
- [4] Guinness World Records; <http://www.guinnessworldrecords.com/records-7000/heaviest-particle-accelerator-detector/>, 07.2014.
- [5] CMS pictures available for publicity; <http://cds.cern.ch/>, 07.2014.
- [6] S.M. Sze; “Semiconductor Devices, Physics and Technology”, Wiley & Sons, 1985, ISBN: 0471874248.
- [7] D. E. Groom and S. R. Klein; “Passage of Particles through Matter”, *The European Physical Journal C - Particles and Fields*, Volume 15, 2000.
- [8] T. Bergauer; “Process Quality Control of Silicon Strip Detectors for the CMS Tracker”, Master’s Thesis, TU Wien, 2004.
- [9] E. Frühwirth; “Processing and Characterisation of Silicon Microstrip Detectors produced by Infineon Technologies Austria AG”, Master’s Thesis, TU Wien, 2011.
- [10] F. Hartmann; “Evolution of Silicon Sensor Technology in Particle Physics”, Springer Berlin Heidelberg, 2009, ISBN: 9783540250944.
- [11] M. Bernhard-Schwarz; “Measurements and Irradiation Analysis of Silicon Structures for the CMS Upgrade”, Master’s Thesis, TU Wien, 2011.
- [12] Y. Tsvividis; “Operation and Modelling of the MOS Transistor”, Oxford University Press, 2nd Edition, 2003, ISBN: 0195170148.
- [13] W. Treberspurg et al.; “Optimizing the quality of silicon strip sensors produced by Infineon Technologies Austria AG”, Conference Proceeding, *Journal of Instrumentation*, Volume 9, 2014.
- [14] K.P. Yan et al.; “ESD Concerns in Sawing Wafers with Discrete Semiconductor Devices”, EOS/ESD Symposium, 2007.

-
- [15] K.P. Yan et al.; “Is CO₂ Bubbling (Carbonation) a Requirement at Semiconductor Wafer Sawing Process”, EOS/ESD Symposium, 2006.
- [16] Carbonic Acid; http://en.wikipedia.org/wiki/Carbonic_acid, 07.2014
- [17] W. Treberspurg; “Manufacturing Process of Silicon Strip Sensors and Analysis of Detector Structures”, Master’s Thesis, TU Wien, 2011.
- [18] A. Dogan; “The Reliability of the Silicon Nitride Dielectric in Capacitive MEMS Switches”, Master’s Thesis, Pennsylvania State University, 2005.
- [19] M. Schwerin et al.; “The Humidity Sensors for the CMS Tracker”, CMS internal note, 2005.
- [20] D. Schroder; “Semiconductor Material and Device Characterisation”, 3rd Edition, Wiley-IEEE Press, 2006, ISBN: 9780471739067.
- [21] M. Moll; “Radiation Damage in Silicon Particle Detectors”, PhD Thesis, Universität Hamburg, 1999.
- [22] Facts about the TRIGA Mark II Reactor; <http://ati.tuwien.ac.at/reaktor>, 07.2014.
- [23] M. Villa et al.; “The Core Conversion of the TRIGA Reactor Vienna”, Conference Proceeding 22nd International Conference Nuclear Energy for New Europe 2013, http://publik.tuwien.ac.at/files/PubDat_226249.pdf, 07.2014.
- [24] A. Gicking; “Neutron Capture Cross Section of Cadmium Isotopes”, Bachelor Thesis, Oregon State University, 2011.

Abstract

The Large Hadron Collider (LHC) located at the European Organization of Nuclear Research (CERN) will be upgraded around the year 2025 which will lead to an increase in luminosity by an order of magnitude. As a consequence the silicon tracker of the Compact Muon Solenoid (CMS) will be renewed which is representing one of the four major experiments located at one of the four interaction points of the LHC. This renewal is necessary since the tracker will reach the end of its lifespan until then. The tracker itself is essential for particle identification like for the recently discovered Higgs boson. The actual micrometer-precise determination of particle tracks is realised by silicon strip sensors. These sensors constitute the centerpiece of the tracker and comprise an active area of more than 200 m^2 .

A collaboration between the Institute of High Energy Physics and Infineon Technologies Austria AG with the aim to establish Infineon as a vendor for silicon strip sensors used for the CMS upgrade is lasting since 2009. This collaboration forms the basis for this Master thesis which represents a part of the evaluation process. The thesis follows already obtained results and opens new insights due to a large variety of conducted investigations. Moreover, aging studies are conducted which are the very first made for sensors of Infineon.

The first part of this thesis constitutes extensive investigations concerning an already earlier observed issue namely an area of defective strips. At first a mechanism most likely causing this defective area is presented. The plausibility of this mechanism is consolidated with the use of a new kind of electrical measurements performed on silicon strip sensors. Furthermore, it is tried to reproduce the defective area by the use of the newly gained insights. Process and handling issues were investigated which eventually resulted in an optimized procedure. Moreover, an inexpensive and simple technique is presented which temporarily resolves the issue of defective strips. The investigations on the defective area are completed by measurements of the resistivity of the uppermost layer of sensors. These high precision measurements which were conducted with the simplest means constitute the basis for future optimizations.

Aging studies are presented in the second part of this thesis. The variability of electrical properties of silicon strip sensors under varying and partly harsh environmental conditions have been investigated with the use of a climate chamber. This setup has been used for the first time for investigations presented here. Hence, initial commissioning and programming of a suitable software was mandatory. Furthermore irradiation studies at a nuclear reactor were conducted for the first time for sensors manufactured by Infineon. Planning and analysis of these studies constitute a basis for further investigations of that kind.

Kurzfassung

Der Large Hadron Collider (LHC) am Europäischen Kernforschungszentrum CERN wird um das Jahr 2025 einem Upgrade unterzogen, welches einen Anstieg in der Luminosität um eine Größenordnung bewirkt. Infolgedessen wird auch der Silizium Spurdetektor (Tracker) des Compact Muon Solenoids (CMS) erneuert, welches eines der vier Hauptexperimente gelegen an einem der vier Interaktionspunkte des LHC's ist. Diese Erneuerung ist nötig da der Tracker bis dahin seine maximale Lebensdauer erreicht haben wird. Der Spurdetektor ist maßgeblich für die Identifikation von Teilchen, wie dem erst kürzlich entdeckten Higgs Boson, verantwortlich. Die mikrometer genaue Auflösung von Teilchenspuren wird durch Silizium-Streifensensoren ermöglicht. Diese Sensoren, deren Gesamtfläche ca. 200 m^2 umfasst, bilden das Kernstück des Spurdetektors.

Seit 2009 existiert eine Kollaboration zwischen dem Institut für Hochenergiephysik und Infineon Technologies Austria AG welche als Ziel hat, Infineon als Hersteller von Silizium Streifensensoren für das Upgrade des CMS Spurdetektors zu etablieren. Sie hält bis zum heutigen Tage an und bildet die Basis für die hier vorgestellte Masterarbeit, welche einen Teil des Evaluierungsprozesses darstellt. Die Arbeit schließt an bereits gewonnene Resultate an und eröffnet neue und wertvolle Erkenntnisse durch eine Vielzahl an durchgeführten Untersuchungen. Des Weiteren werden Alterungsstudien präsentiert, die das erste Mal für Sensoren dieses Herstellers durchgeführt wurden.

Den ersten Teil dieser Arbeit bildet die ausführliche Untersuchung einer bereits bekannten Problematik, welche eine Zone von defekten Streifen darstellt. Zunächst wird ein möglicher Mechanismus beschrieben, der für diesen Defekt verantwortlich sein könnte. Die Plausibilität dieses Mechanismus wird daraufhin durch eine neue Methode von elektrischen Messungen an Silizium Streifensensoren gefestigt. Auch wurde versucht das Fehlerbild mit Hilfe der neu gewonnenen Erkenntnisse hervorzurufen. Mögliche Fehlerursachen bei der Prozessierung, aber auch bei der Handhabung wurden erforscht, welche den Grundstein zu einem optimierten Verfahren bildeten. Des Weiteren wird eine kostengünstige und einfache Methode präsentiert, welche das Problem der defekten Streifen temporär behebt. Abgeschlossen werden die Untersuchungen der defekten Zone mit Messungen des spezifischen elektrischen Widerstandes der obersten Schicht von Streifensensoren. Diese hochpräzisen Messungen wurden mit einfachsten Mitteln durchgeführt und bilden den Grundstein für zukünftige Optimierungen.

Den zweiten Teil dieser Arbeit bilden Alterungsstudien. Die Variabilität der elektrischen Eigenschaften von Silizium Streifensensoren wurden zunächst unter variierenden und teils extremen Umwelteinflüssen mit Hilfe einer Klimakammer untersucht. Dieser Setup wurde das erste Mal für die hier vorgestellten Untersuchungen verwendet, weswegen die Inbetriebnahme und das Programmieren einer dafür geeigneten Software ebenfalls maßgeblich war. Des Weiteren wurden erstmals Bestrahlungsstudien für Sensoren dieses Herstellers an einem Kernreaktor durchgeführt. Die Planung und die Auswertung dieser Studien bilden einen Grundstein für weitere Untersuchungen dieser Art.

Curriculum Vitae

Personal Data

Date and Place of Birth: 24. August 1988, Vienna
Citizenship: Austrian
Address: Winzerstrasse 10, 1130 Vienna
Marital Status: Single

School Education

1994 to 1998: Elementary School, 1130 Vienna
1998 to 2005: Grammar School, 1140 Vienna
2006 to 2008: Maturaschule Dr. Roland, 1070 Vienna
09.10.2008: Graduation as an external student (Externistenreifeprüfung), 2500 Baden

University Education

Oct. 2012: Bachelor of Science (BSc) in Physics, University of Vienna
Since Oct. 2012 : Master's course in Physics, University of Vienna

Employment

Jan. 2006: Internship at the LEASFINANZ GmbH
Jul. 2013 to Jul. 2014 : Industry internship at Infineon Technologies Austria AG

Others

IT skills: NI LabVIEW, Wolfram Mathematica, Scilab / Matlab, Qt-Plot / Origin, Fortran 90, Latex, Microsoft Office
Languages: German (mother tongue), English